EXPLORING MILKY WAY HALO SUBSTRUCTURES WITH LARGE-AREA SKY SURVEYS

A Dissertation

by

TING LI

Submitted to the Office of Graduate and Professional Studies of
Texas A&M University
in partial fulfillment of the requirements for the degree of

DOCTOR OF PHILOSOPHY

Chair of Committee,	Darren L. DePoy
Co-Chair of Committee,	Jennifer L. Marshall
Committee Members,	Nicholas B. Suntzeff
	Casey J. Papovich
	Sherry J. Yennello
Head of Department,	George R. Welch

August 2016

Major Subject: Physics

ABSTRACT

Over the last two decades, our understanding of the Milky Way has been improved thanks to large data sets arising from large-area digital sky surveys. The stellar halo is now known to be inhabited by a variety of spatial and kinematic stellar substructures, including stellar streams and stellar clouds, all of which are predicted by hierarchical Lambda Cold Dark Matter models of galaxy formation.

In this dissertation, we first present the analysis of spectroscopic observations of individual stars from the two candidate structures discovered using an M-giant catalog from the Two Micron All-Sky Survey. The follow-up observations show that one of the candidates is a genuine structure which might be associated with the Galactic Anticenter Stellar Structure, while the other one is a false detection due to the systematic photometric errors in the survey or dust extinction in low Galactic latitudes.

We then presented the discovery of an excess of main sequence turn-off stars in the direction of the constellations of Eridanus and Phoenix from the first-year data of the Dark Energy Survey (DES) – a five-year, 5,000 deg^2 optical imaging survey in the Southern Hemisphere. The Eridanus-Phoenix (EriPhe) overdensity is centered around $l \sim 285°$ and $b \sim -60°$ and the Poisson significance of the detection is at least 9σ. The EriPhe overdensity has a cloud-like morphology and the extent is at least ~ 4 kpc by ~ 3 kpc in projection, with a heliocentric distance of about $d \sim 16$ kpc. The EriPhe overdensity is morphologically similar to the previously-discovered Virgo overdensity and Hercules-Aquila cloud. These three overdensities lie along a polar plane separated by $\sim 120°$ and may share a common origin.

In addition to the scientific discoveries, we also present the work to improve

the photometric calibration in DES using auxiliary calibration systems, since the photometric errors can cause false detection in finding the halo substructure. We present a detailed description of the two auxiliary calibration systems built at Texas A&M University. We then discuss how the auxiliary systems in DES can be used to improve the photometric calibration of the systematic chromatic errors – source color-dependent systematic errors that are caused by variations in the wavelength dependence of the atmospheric transmission and the instrumental throughput.

DEDICATION

To my Grandpa, please forgive me for not saying goodbye to you in person.

To Mom and Dad, thanks for loving me into the toughest kid you have ever had.

ACKNOWLEDGMENTS

First of all, I want to take this opportunity to express my gratitude to my graduate advisor, Darren DePoy. Darren gave me the opportunity to join the Dark Energy Survey (DES) and work on the instrumentation projects for DES. He taught me how to become a bridge between the scientists and engineers and to build instruments that make the science happen. He allowed me free rein to pursue projects that I found interesting, and gave me all the financial support a graduate student could want. He is the most knowledgeable person that I have ever met and he has become my role model since I started working with him. I really appreciate his patience with me when I turned a five-minute conversation into an hour-long discussion. There are three sentences I learned from Darren that I will never forget in my life:

1. We are scientists; we use numbers.

2. We are astronomers; we turn money into astrophysics.

3. As an instrument builder, it is important to remember "better is the enemy of good enough". That is saying, we should always start with the science goal we want to achieve.

I want to give a big thank-you to my co-advisor, Jennifer Marshall – actually, I probably spent way more time with Jen than with Darren. I remember well that Jen spent time teaching me how to do photometry and spectroscopy, how to write my first observing proposal, how to write my first paper. Also, she spent dozens of nights with me at the McDonald observatory training me to be a good observer. She also organizes lots of social activities for the lab, including the Animal Grill Party and Superbowl Night. Moreover, she invited my Mom and me to the Thanksgiving dinner with her family. To me, she is more like a close friend than a mentor or an

advisor in my graduate life. I believe that, because of her, my life as an international student (and the only international student in astronomy group for the first two years of my graduate school) is much better integrated into this country. I will not repeat your name again and again in this acknowledgment but you know that you helped on every project I worked on.

I also want to thank the other members in my committee, Nick Suntzeff, Casey Papovich and Sherry Yennello. I remember a lot of long conversations with Nick about the big pictures in astronomy when I was hesitating what to choose as my research field for my dissertation. I am grateful that I chose near-field cosmology as my research field and I definitely think that the conversations with him helped me a lot in making this decision. ASTR 314 was my first non-101-level astronomy class. I really appreciate that Casey is such a great instructor and allowed me to sit in the class for the entire semester (and I really enjoyed it!). I also want to thank Sherry for spending time being on my committee and coming to my preliminary examination even though she is such a busy person. Her perspective as a scientist outside the field definitely helped to make my dissertation better.

I appreciate all the collaborators throughout my graduate school on my various projects. First, I want to thank Kathryn Johnston for coming to our university, giving a great colloquium, and then giving me the opportunity to work with her and her postdoc Allyson Sheffield on the project with M-giants (see Section 2 in this dissertation). In particular, I need to thank Allyson for sharing her data with me and also for giving me a lot of advice and assistance on the data analysis. Also, I thank Kathryn, Allyson and Steve Majewski for many discussions over Skype on this project.

Throughout my graduate school, I spent the majority of my time on DES, and I want to thank all the 400 scientists in the collaboration. Maybe I do not know

all of you but I definitely enjoyed being part of the collaboration and I am proud to be a part of it. I want to send my special thanks to the two working groups in which I mainly participate: the calibration working group and the Milky Way science working group.

I want to thank Douglas Tucker, Rick Kessler, Dave Burke, Gary Bernstein, and William Wester from the calibration group for their help. The discussions with them in the telecons and the meetings definitely helped me understand the photometric calibrations for DES and dramatically improved my first paper in the calibration working group (see Section 5 in this dissertation).

I want to thank Brian Yanny, Eduardo Balbinot, Basilio Santiago, Kathy Vivas and Josh Simon from the Milky Way group for their help. I really appreciate the assistance they provided to make my first paper in this science working group happen (see Section 3 in this dissertation). I need to thank Nick Mondrik for helping me to create better figures and re-run calculations while I was super busy on the dwarf galaxy follow-up. I know it was less than half a year between the start of the project and the time when the paper was submitted; this could not have happened without all your support.

I also want to thank Keith Bechtol, Alex Drlica-Wagner, Risa Wechsler and Josh Simon for letting me work on the spectroscopic follow-up of the Milky Way satellites. This is not part of my dissertation but I really enjoyed the work with you all in the past year. I hope I will keep working on this topic in my postdoctoral career.

I also want to thank everyone in the Munnerlyn lab, Travis Prochaska, J-P Rheault, Luke Schmidt, Don Corona, Rick Allen, and undergraduates Nick M., Steven V., Patrick, Jason, Emily M., Emily B., etc. It was fun to spend the majority of my graduate school career in the lab and work with you on different instrumentation projects, from small projects like aTmCam (Section 4 in this dissertation) to

big ones like HETDEX/VIRUS.

Applying for postdoctoral positions was a tough but interesting period in the last part of graduate life, and I thank everyone who helped me survive this process. I am so lucky to have the support from all of my letter writers: Darren, Jen, Josh Simon, Josh Frieman, Nick Suntzeff, Brian Yanny, and Douglas Tucker. I want to give a big thank-you to Dan Nagasawa and Katelyn Stringer, who read most of my applications and helped me on my statements, especially with the grammar and language checks. I want to thank Casey, Ryan Quadri, Louie Strigari, Kim-Vy Tran, Lifan Wang, Lucas Macri, and my fellow cohort of graduate students, Steven Boada, Ryan Oelkers, Brett Salmon, Mike Smitka for their advice and companionship. It was a great pleasure to spend the past five-and-a-half years together with you.

I would also thank all the graduate students at Texas A&M– Steven B., Ryan O., Brett, Mike, Jimmy, Adam, Heath, Dan, Ben, Leo, Andrew, Yi, Wenlong, Nancy, Peter, Katelyn, and Vince– for their friendship and keeping me entertained. Thanks Steven for introducing me to *python* when I was hesitating between *IDL* and *python* in my first year of my graduate school, and for providing a huge amount of help with programming throughout graduate school. Thank you Jimmy for helping me start using the VLT/UVES pipeline quickly and for making this dissertation template for astronomy graduate students. Thank you Mei-Yu Wang for a lot of great conversations on simulations and modelings. Thank you to all my peers for enduring my endless questions – "tingquisition", and teaching me all kinds of funny words, such as "Ish Kabibble".

Last but not least, I want to thank my family – my mom and dad for all the support for the career path I chose and for forgiving me for not spending time by their side for the past few years. A last big hug to my fiance, Wei, who made graduate school much easier and more colorful than it would be if it was all on my own.

NOMENCLATURE

1m	CTIO/SMARTS (YALO) 1 meter telescope
2MASS	Two Micron All-Sky Survey
4m	CTIO Blanco 4 meter telescope
APOGEE	Apache Point Observatory Galactic Evolution Experiment
AOD	Aerosol Optical Depth
aTmCam	Atmospheric Transmission Monitoring Camera
CCD	Charge Coupled Device
CTIO	Cerro Tololo Inter-American Observatories
dec	Declination
DECal	Dark Energy Camera calibration system
DECam	Dark Energy Camera
DES	Dark Energy Survey
DESDM	DES Data Management
EriPhe	Eridanus-Phoenix Overdensity
EW	Equivalent Width
FWHM	Full Width at Half Maximum
GASS	Galactic Anticenter Stellar Structure
GPS	Global Positioning System
GSR	Galactic Standard of Rest
HerAq	Hercules-Aquila Cloud
HET	Hobby Eberly Telescope
HRS	High Resolution Spectrograph
LSR	Local Standard of Rest

M31	Andromeda Galaxy
MSTO	Main Sequence Turn-Off
NASA	National Aeronautics and Space Administration
NCSA	National Center for Supercomputing Applications
NGSL	Next Generation Spectral Library
NIST	National Institute of Standards and Technology
OMPS	Ozone Mapping and Profiler Suite Nadir Mapper
PWV	Precipitable Water Vapor
RA	Right Ascension
RV	radial velocities
S/N	Signal-to-Noise Ratio
SBIG	Santa Barbara Instrument Group
SCE	Systematic Chromatic Errors
SED	Spectral Energy Distribution
SEGUE	Sloan Extension for Galactic Understanding and Exploration
SDSS	Sloan Digitized Sky Survey
SNe	Supernovae
SNe Ia	Type Ia Supernovae
SPT	South Pole Telescope
TriAnd	Triangulum-Andromeda Cloud
VOD	Virgo Overdensity
Y1A1	Year 1 Annual 1 Data Release for DES
ΛCDM	Lambda Cold Dark Matter

TABLE OF CONTENTS

LIST OF FIGURES

xv

LIST OF TABLES

1. INTRODUCTION

1.1 Formation and Evolution of the Milky Way and Its Halo

One of the key questions of astrophysics is to understand how galaxies formed and evolved after the big bang. Milky Way, the Galaxy we reside in, provides us a unique opportunity to study a galaxy with individual stars. By measuring and analyzing the properties of large samples of stars in Milky Way, we can understand the galaxy formation and evolution in ways that cannot be extracted from observations of extragalactic objects (Ivezić et al., 2012).

In the canonical model of Milky Way formation, the Galaxy formed through a rapid collapse of a protogalactic nebula and the gas was settled into a rotating disk, a scenario suggested by Eggen et al. (1962). Their model explained the general structural, kinematic, and metallicity correlations of stars in the Milky Way. It also implied a smooth distribution of stars observable today. The Milky Way structure is fairly simple, with three discrete components: the bulge, the thin and thick disk, and the halo. However, starting from Searle & Zinn (1978), and many new discoveries of complex substructures in the distribution of the Milky Ways stars, this canonical view was challenged. Unlike the smooth models that have been used on local scales, new data from large-area sky surveys indicate the presence of more irregular substructures. We now know that the Milky Way is a much complex and dynamic structure and is shaped by the infall merging of smaller galaxy satellites. Numerical simulations suggest that this merger process plays a crucial role in establishing the structure and motions of stars in our Milky Way halo. The substructure is caused by the disruption of accreting galaxies and is predicted by the hierarchical Lambda Cold Dark Matter (ΛCDM) models of galaxy formation (Bullock & Johnston, 2005;

1

Johnston et al., 2008).

Before the discovery of tidal streams, the stellar halo was modeled as a smooth distribution of stars, with a total mass of $\sim 2 \times 10^9$ $M_\odot$ and a very old stellar population, with ages of $\sim$ 10–13 Gyr. Many studies show that the stellar halo can be better described as two overlapping components – inner halo and outer halo (Carollo et al., 2007). The two components are not only different in their density profiles (Bell et al., 2008), but also kinematically different, especially in its mean rotational velocity (Carollo et al., 2010).

Besides this spheroidal component – a smooth halo, the Milky Way is also orbited by over a hundred of globular clusters (Harris, 2010), which are generally free of gas and dark matter, and over several dozens of satellite galaxies (McConnachie, 2012), which contains large amounts of dark matters. When a globular cluster or a satellite galaxy comes too close to the Milky Way, the galaxy's gravitational potential will pull the stellar association apart via tidal force and forms tidal streams.

The Milky Way stellar halo not only has a smooth, well-mixed component but also contains dwarf galaxies, globular clusters, tidal streams. It is believed that some fraction of the Milky Way stellar halo was formed from the debris of accreted satellite galaxies that were disrupted by Milky Way gravitational potential via tidal interaction (see e.g. Bullock & Johnston, 2005; DeLucia & Helmi, 2008; Cooper et al., 2010), even though in-situ star formation may have played a role in the formation of the Milky Way halo (Helmi, 2008; Zolotov et al., 2009). A detailed overview of the halo substructures known today will be presented in Section 1.2.

1.2 The Discovery of Milky Way Halo Substructures in the Era of Large-Area Sky Surveys

1.2.1 Large-Area Sky Surveys

Over the past two decades, astronomy moved beyond the traditional observational paradigm and undertook large-area digital sky surveys, such as the Sloan Digital Sky Survey (SDSS York et al., 2000) and the Two Micron All Sky Survey (2MASS Skrutskie et al., 2006). This observational progress is an outcome of improvement in the hardware – detector development and the software – information technology. The revolutions in observations have had a dramatic impact on nearly all fields of astronomy, including studies of understanding our own Milky Way.

The SDSS is a digital photometric and spectroscopic survey in the Northern hemisphere. It covers over one-quarter of the sky in the North Galactic cap and a smaller area in the Southern Galactic hemisphere along the Celestial Equator. The Data Release 12[1] (Alam et al., 2015) has a sky coverage of about 14,600 $\deg^2$ and includes photometric measurements for 469 million unique objects. The completeness of the SDSS catalogs for point sources is $\sim$95% at an r-band magnitude of $\sim$22. The wavelength coverage of the SDSS photometric system ($ugriz$) has effective wavelengths from 3,540 Å to 9,250 Å and photometry is accurate to $\sim$0.02 mag. In addition to its imaging survey data, the SDSS also conducted a series of spectroscopic surveys as the extensions of the SDSS project to study our Milky Way. For example, Sloan Extension for Galactic Understanding and Exploration (SEGUE; Yanny et al., 2009) and its continuation the SEGUE-2 (Rockosi et al., 2009) are carried out during the SDSS-II (first extension of SDSS) and SDSS-III (second extension of SDSS). Another example is the Apache Point Observatory Galactic Evolution Ex-

---

[1]http://www.sdss.org/dr12/scope/

periment (APOGEE; Majewski et al., 2015) and its continuation APOGEE-2 during the SDSS-III and SDSS-IV (third extension of SDSS).

The 2MASS databases are derived from an all-sky near-IR photometric survey with limiting magnitudes of J = 15.8, H = 15.1, and K = 14.3 (10σ detection). The 2MASS point source catalog contains positional and photometric information for 471 million sources (mostly stars). A major advantage of 2MASS over the SDSS is the full sky coverage and its ability to penetrate deeper through the interstellar dust in the Galactic plane. In addition, it is much easier to photometrically identify certain stellar populations using near-IR data than with optical data. For example, Majewski et al. (2003) have demonstrated that M-giant candidates, color-selected from the 2MASS database, are extremely powerful probes of halo substructures over the entire sky (see details in Section 2.2).

1.2.2   An Overview of the Discoveries of Halo Substructures

Thanks to the arrival of large surveys like SDSS and 2MASS, a large amount of halo substructures have been discovered in the Galactic halo.

The most striking and beautiful example is the Sagittarius tidal stream, which was discovered by two different groups on a similar time scale using blue A-type stars (Yanny et al., 2000) and RR Lyrae stars (Ivezić et al., 2000). This stream originates in the Sagittarius dwarf spheroidal galaxy (Ibata et al., 1994) which is currently being disrupted by the tidal field of the Milky Way. This tidal stream was later traced across the sky in M-giant stars identified photometrically in 2MASS (Majewski et al., 2003).

Soon, many additional substructures were discovered. Vivas et al. (2001) found an overdensity of RR Lyrae stars in the Virgo constellation, which was related to the Virgo overdensity (VOD) discovered using F-type turn-off stars by Jurić et al.

(2008). Belokurov et al. (2007) discovered the Hercules-Aquila cloud (HerAq), which is an extended substructure in the direction near the Galactic center. A much narrower tidal stream was found extending tens of degrees from the Pal 5 globular cluster (Odenkirchen et al., 2001; Rockosi et al., 2002). Apart from those, there are also two controversial overdensities close to the Galactic plane – one is near the anticenter commonly referred to as the Monoceros Ring (Ibata et al., 2003; Yanny et al., 2003) or Galactic Anticenter Stellar Structure (GASS; Crane et al., 2003), and the other is more distant and in the south of the Galactic plane called the Triangulum-Andromeda cloud (TriAnd Rocha-Pinto et al., 2004).

1.2.3   Stellar Streams and Stellar Clouds

The halo substructures can be usually classified into two categories – stellar streams and stellar clouds, which depend on their morphology, though the boundary between the two classes is also pretty vague as the morphology of an overdensity is sometimes hard to tell. The "clouds" here are overdensities in the halo that span many kiloparsecs across the sky and could not possibly be gravitationally bound, with a cloud-like morphology rather than the linear structure like stellar streams. These structures are thought to be the remains of a dwarf galaxy – simulation shows that if a dwarf galaxy with highly eccentric orbits gets tidal disrupted by the Milky Way potential at perigalacticon of the orbit, the debris could result in a pile-up of stars at the apoGalacticon of the orbit and it would look like a large cloud when viewed from inside the Milky Way (Johnston et al., 2012).

Thanks to the massive observations on Sagittarius tidal stream, both photometrically and spectroscopically, the stellar streams are well studied. Much less studied and understood are the equally impressive stellar clouds, even though cosmological models of Milky Way formation suggest that debris should be detectable in clouds

5

as frequently as streams (Johnston et al., 2008). For example, the nature of these cloud-like overdensities, such as TriAnd, HerAq, and VOD, are still unknown or under debate. If the stellar clouds are truly the outcome from the remains of a dwarf galaxy with more eccentric orbits, then these clouds might penetrate to within ∼10 kpc of the Galactic center and can be connected with halo substructure in the solar neighborhood.

1.3   Outline of the Dissertation

This dissertation is aiming to understand the nature of the stellar clouds using the large dataset from large-area sky surveys.

In Section 2, we spectroscopically follow up the two candidate structures found in the M-giant catalog in 2MASS by Sharma et al. (2010). The two structures are named A11 and A13 in their paper. These two candidates are selected because they might have a tentative connection between nearby high-velocity streams (A13, ∼20 kpc) to distant clouds (A11, ∼100 kpc). The follow-up observations show that A13 is a real structure while A11 is a false detection due to the systematic photometric errors in 2MASS.

In Section 3, we search for new halo substructure in the Dark Energy Survey (DES), a five-year, 5,000 deg^2 optical imaging survey in the Southern Hemisphere. A new cloud-like overdensity, the Eridanus-Phoenix overdensity is discovered using the first year internal data release from DES. We discuss the possible scenarios in which this overdensity was formed.

Section 4 give a detailed description of the Dark Energy Survey and its auxiliary calibration systems, which is used for calibrating the DES photometry to better than 1%. As we show in Section 2 that the photometric errors can cause false detection in the halo substructure, in Section 5 we discuss how the auxiliary systems in DES

can be used to calibrate the photometry, especially on one type of systematic errors

– the systematic chromatic errors.

2. EXPLORING HALO SUBSTRUCTURES WITH M-GIANTS

2.1 Introduction

Over the last two decades, large-area digital sky surveys provided deep and global photometric catalogs of stars in our Galaxy. The ability to detect and characterize substructures in our halo has increased dramatically. Most well known and best studied among these substructures are stellar streams – long, sinuous, dynamically cold strands of stars. Apart from stellar streams, simulations also show that some merger events, depending on their trajectory and potential, could result in the pile-up of debris in apoGalactic patches in the Milky Way. These patches of debris are known as stellar clouds.

Johnston et al. (2012) demonstrates not only that debris clouds are distinct morphologically from streams but also that they are distinct kinematically. Unlike streams, stellar clouds can exhibit large velocity and distance gradients, with changes of 100 km s^{-1} and tens of kiloparsec possible across just tens of degrees, a result of the projection of debris stars radially receding and returning from the apoGalactic cloud. Furthermore, stellar clouds can penetrate to within $\sim$10 kpc of the Galactic center and thus are most intimately connected with halo substructure in the solar neighborhood.

However, only a few stellar clouds have been identified to date, e.g., the Triangulum-Andromeda cloud (TriAnd; Rocha-Pinto et al., 2004), Hercules-Aquila cloud (Belokurov et al., 2007), and the Virgo Overdensity (Jurić et al., 2008), etc. Stars in stellar clouds are not necessarily as tightly associated on the sky as the stars in stellar streams, making stellar clouds more difficult to identify due to their low surface brightness.

While discovery by visual inspection has proved successful so far, the scale and sophistication of the data set of the current and future sky surveys motivate an exploration of methods that can instead objectively identify structures. Recently, Sharma et al. (2010, here after S10) developed a density-based hierarchical group-finding algorithm to identify stellar halo substructures in a catalog of the M-giants from the Two Micron All Sky Survey (2MASS). This algorithm uncovered 16 substructures in the Milky Way halo, six of which were at the time unknown structures.

We spectroscopically follow up the two candidate structures found by S10. The two structures are named as A11 and A13 in their paper. These two candidates are selected because they might have a tentative connection between nearby high-velocity streams (A13, $\sim$20 kpc) to distant clouds (A11, $\sim$80 kpc). We measure the line-of-sight velocities of the stars in the candidate structures and see if their kinematics are consistent with an orbit with high eccentricity.

2.2 Sample Selection

The samples are selected from the 2MASS catalog (Skrutskie et al., 2006) with dereddening applied using the Schlegel et al. (1998) extinction maps. More detailed selection criteria can be found in S10. We give a brief description here.

The stars are selected to be M giants in the Galactic halo by applying a selection criteria similar to those used by Majewski et al. (2003) to identify the tidal tails of Sagittarius dwarf galaxy, as giants begin to separate from dwarfs in the near-infrared colorcolor diagram. Different from Majewski et al. (2003), the search of M-giants are restricted with $(J - K_S)_0 > 0.97$ and $K_{S,0} > 10$ (labeled with subscript 0 for the dereddened 2MASS system, hereafter). The former condition minimizes the contamination by disk M-dwarfs by restricting the sample to a redder population and the latter one gets rid of stars near the Sun. Furthermore, Rectangular masks are
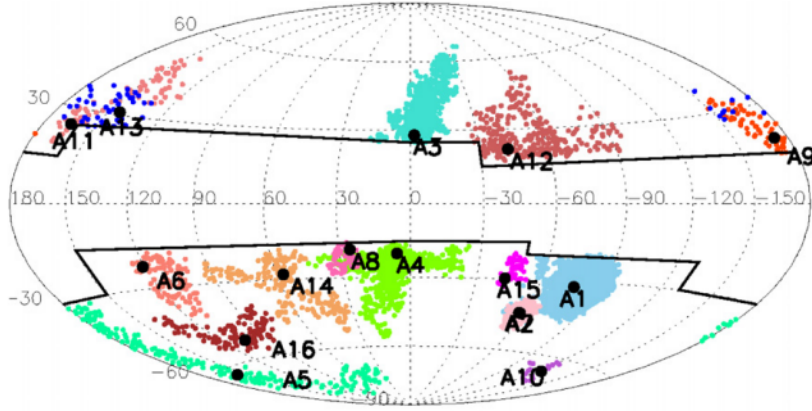
Figure 2.1: Aitoff projection map of the overdensity groups (A1–A16) found in the 2MASS M-giant sample (Sharma et al., 2010). A11–A16 are previously unknown. Large black filled circles show the position of the density peak in a group. Stars in each group are color-coded with a unique color and are shown as small filled circles. The solid black lines mark the low-latitude area that is excluded from the analysis due to high extinction.

used to cover regions of high dust extinction at low latitude. These stars are further subjected to a group-finding algorithm `Enlink` (Sharma & Johnston, 2009) to locate the structures. This algorithm uncovered 16 groups in the Milky Way halo, six of which (A11-A16) are previously unknown structures. Figure 2.1 shows the position of the 16 groups.

We spectroscopically followed up the two overdensity structure candidates revealed with the group finder, namely A11 and A13. A13 contains 54 M-giants, spanning in galactic coordinates at $130° < l < 210°$ and $25° < b < 40°$, lying right above the edge of one of the rectangular masks ($b \sim 25°$). The brightness of 54 stars in A13 ranges $10 < K_{S,0} < 11.3$ and estimated distance is 22.6 ± 11 kpc. A11 contains 79 M-giants and locates in a similar area in the sky as A13. However, the stars in A11 are much fainter ($13 < K_{S,0} < 14$) with estimated distance of 88.4 ± 44 kpc.

2.3 A13 Candidate

2.3.1 Observations and Data Reduction

Spectra for the A13 candidate were obtained over five observing runs at MDM Observatory, KPNO Observatory, and McDonald Observatory. The observing nights and the instruments are summarized in Table 2.1. The MDM run and KPNO run were conducted at the same time when spectra of the M-giant candidates in Triangulum-Andromeda cloud were collected (Sheffield et al., 2014, here after S14). For all five observing runs, biases were taken at the beginning and end of each night to verify that there were no significant variation in bias over time. Flats were taken every night using quartz lamp. In order to get accurate radial velocity measurements, arc frames were taken at the same position as each target to account for telescope flexure. For both Goldcam and Modspec, XeNeAr lamp was used; for ES2, NeAr lamp was used. All three instruments were set up so that they at least cover the spectral range 8000-8900 Å and had a spectral resolution ~ 4 Å . The spectral range covers both the Na I doublet lines around 8200 Å , which can be used to discriminate foreground M-dwarfs, and the Ca II triplet lines around 8500-8700 Å which can be used to derive the radial velocities and metallicities. The target spectra had a mean signal-to-noise ratio (S/N) ~ 25 around the CaT feature. Most spectra taken during the MDM run and McDonald run have S/N > 30, while the spectra from KPNO run have S/N ~ 15. Besides the program stars, a handful radial velocities (RV) standard stars and one telluric standard star were observed every night along with the program stars. RV standards are picked so that they have the similar spectral type as the program stars.

We reduced the data with the standard routines in IRAF. We began by subtracting the bias level using the overscan strip on each frame. Normalized flat were

Table 2.1: Summary of Observing Runs

UT	Observatory	Telescope	Spectrograph
2011 Nov 10	MDM	Hiltner 2.4 m	Modspec
2011 Nov 15–20	KPNO	2.1 m	Goldcam
2012 Nov 28–30	McDonald	Otto Struve 2.1 m	ES2
2012 Oct 27–29	MDM	Hiltner 2.4 m	Modspec
2014 Jan 09–12	McDonald	Otto Struve 2.1 m	ES2
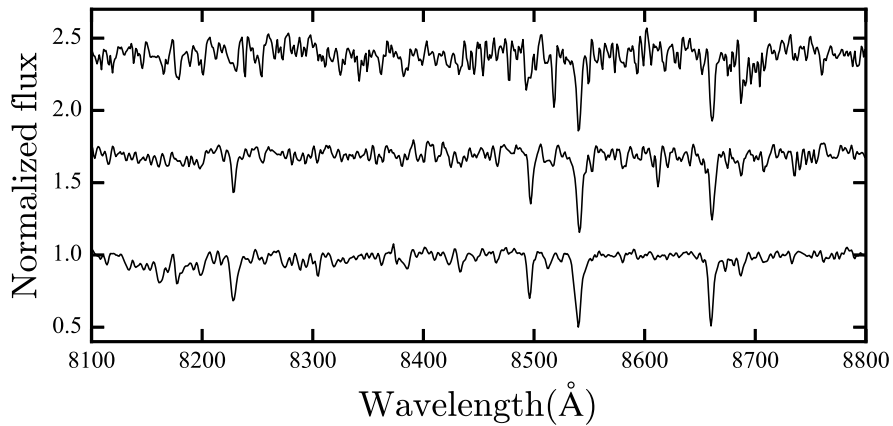
Figure 2.2: Examples of wavelength calibrated spectra at various S/N ratio from A13 sample.

created using the median-combined flats and the science frames were divided by the normalized flat. The *apall* task was used for one-dimensional extraction and *identify* task was used for wavelength calibration. The dispersion solution was finally applied to the spectra using the *dispcor* task. The wavelength calibrated spectra for several program stars are shown in Figure 2.2.

2.3.2   Data Analysis and Results

2.3.2.1   Dwarf/Giant Separation

We first checked whether or not the candidates are M-giants. The Na I doublet ($\lambda\lambda 8183, 8195$) is gravity sensitive so we can discriminate dwarfs and giants by measuring the equivalent width (EW) of the Na I doublet (see e.g., Schiavon et al., 1997). We first applied a telluric correction to our spectra using *telluric* task in IRAF with the telluric standard star to remove the water vapor absorption around 8227 Å . Then we numerically integrated the bandpass 8179–8199 Å to measure the EW, in a similar way as presented in S14. All 54 candidate has EW less than 2 Å and therefore all the candidates are giants. Since the candidates are fairly bright ($10 < K_{S,0} < 11.3$), we have no dwarf contamination in our sample. This matches with Majewski et al. (2003) where they state that contamination from M dwarfs is a concern with $K_{S,0} > 12.5$. This also matches the M-dwarf contamination rate seen in the S14 sample, where the M dwarf contamination started at $K_{S,0} \sim 11.5$ in their sample.

2.3.2.2   Radial Velocity

The program stars were cross-correlated against the nightly RV standard stars using the *fxcor* task in IRAF to calculate the relative velocities. The heliocentric velocities of the program stars were derived after the Earths motion was corrected using *rvcorrect* task.

For every night, the RV standard stars were also cross-correlated against each other to check the level of stability of the instrument. The average velocity precision from cross-correlating the RV standards were ~ 5.3 km s^{-1} . 23 out of 54 program stars were observed in multiple runs on different instruments. The average dispersion of these 23 repeated observations is 5.5 km s^{-1} , which is very close to the RV

13

precision derived from cross-correlating the standards for every night. We, therefore, conclude that $\sigma = 5.3$ km s^{-1} is the velocity precision for this study. The heliocentric radial velocities for all 54 targets are presented in Table 2.2. For the stars observed in multiple runs, the averages of velocities are presented.

We then converted the heliocentric radial velocities, v_{hel}, to the radial velocities in the Galactic standard of rest (GSR) frame, v_{GSR}. This conversion is to get rid of the motion of the sun with respect to the Galactic Center. We adopted the circular orbital velocity of Milky Way at the Suns radius $\Theta_0 = 236$ km s^{-1} (Bovy et al., 2009) and solar motion of $(U_\odot, V_\odot, W_\odot) = (11.1, 12.24, 7.25)$ km s^{-1} (Schönrich et al., 2010).

We show the distribution of v_{GSR} of 54 stars in A13 in the left panel of Figure 2.3. The stars in A13 show a prominent peak at $v_{GSR} \sim 50$ km s^{-1} . As a comparison, we also show the velocity distribution of a synthetic sample of stars generated from Galaxia model (Sharma et al., 2011). The synthetic sample is selected to be within the same patch of the sky (i.e. $130° < l < 210°$ and $25° < b < 40°$) with the same magnitude and color range as the A13 sample and is mostly composed of halo stars. It is apparent that the A13 sample has a much smaller velocity dispersion than expected for a random distribution of halo stars predicted by Galaxia.

In the right panel of Figure 2.3, we see a velocity gradient in the sense that v_{GSR} is increasing as the Galactic longitude of stars decreases, consistent with an prograde rotation. We apply an iterative clipping by fitting a linear fitting to v_{GSR} as a function of Galactic longitude and then removing 2.5-σ outliers iteratively. Three stars are removed as outliers. From linear fit with remaining 51 members, we derive the velocity dispersion, the gradient, and the velocity at $l = 180°$ to be:

$$\sigma_v \sim 40 \, \text{km s}^{-1} \tag{2.1}$$

14

Table 2.2: Heliocentric Velocities of the Program Stars

name	RA	DEC	l	b	$K_{S,0}$	$(J-K_S)_0$	$v_{hel}(\mathrm{km\ s^{-1}})$
A13-01	08:22:35.069	16:57:50.699	207.06	27.56	10.1	1.04	100.23
A13-02	08:40:52.109	17:00:07.637	208.90	31.63	10.5	0.99	-37.96
A13-03	08:25:16.774	31:06:39.055	191.74	32.61	10.4	0.98	-45.70
A13-04	07:49:24.316	38:11:15.719	181.75	27.19	10.2	1.01	-33.27
A13-05	08:14:17.175	39:52:39.025	181.03	32.27	10.3	0.98	37.72
A13-06	08:27:04.396	19:52:58.114	204.40	29.62	10.8	0.98	-98.19
A13-07	08:26:57.981	21:25:59.487	202.72	30.13	10.1	1.05	-27.74
A13-08	08:27:35.892	46:05:20.722	173.96	35.45	10.8	0.99	122.33
A13-09	07:55:14.474	45:10:21.339	174.24	29.72	10.5	0.99	14.20
A13-10	09:01:20.104	21:00:53.914	206.37	37.56	10.7	0.97	-33.91
A13-11	08:04:53.175	50:54:53.847	167.84	32.05	10.1	1.00	-48.50
A13-12	07:18:48.413	57:37:29.205	159.28	26.22	10.3	1.01	-64.50
A13-13	07:58:35.208	71:26:37.097	143.74	30.94	10.8	0.98	-54.50
A13-14	07:59:57.788	67:21:15.233	148.48	31.45	10.3	0.98	-84.30
A13-15	08:23:01.736	63:36:55.907	152.61	34.22	10.4	1.04	-62.30
A13-16	08:35:19.320	63:09:12.508	152.91	35.65	10.4	1.07	-80.50
A13-17	08:37:16.838	61:24:38.650	154.98	36.17	10.1	1.11	-16.30
A13-18	08:02:42.925	55:21:16.735	162.59	32.00	10.4	1.04	8.70
A13-19	07:29:03.287	63:32:14.931	152.86	28.23	10.6	1.00	-14.20
A13-20	07:01:29.762	65:26:34.302	150.33	25.53	10.2	1.03	-53.05
A13-21	07:03:17.681	62:10:19.597	153.93	25.13	10.0	0.98	-31.77
A13-22	08:08:19.003	46:06:53.789	173.55	32.12	10.1	1.05	9.30
A13-23	08:19:09.002	66:35:06.844	149.14	33.40	10.4	1.01	-86.60
A13-24	08:50:27.058	83:34:26.310	129.38	30.17	10.4	0.98	-161.56
A13-25	06:53:46.314	74:23:42.096	140.38	26.21	10.8	1.00	-73.98
A13-26	06:59:51.420	79:21:22.310	134.89	27.01	10.9	0.98	-171.77
A13-27	08:45:58.500	53:38:44.992	164.47	38.32	10.3	1.07	-54.32
A13-28	07:16:00.837	69:06:09.217	146.47	27.39	11.0	1.01	-45.19
A13-29	07:15:42.543	67:03:59.384	148.75	27.17	10.1	0.98	-19.70
A13-30	06:56:33.832	71:31:34.103	143.57	26.03	10.0	1.01	-220.07
A13-31	08:18:28.676	24:35:03.724	198.55	29.32	10.2	1.02	71.31
A13-32	07:34:53.223	47:01:06.875	171.42	26.61	11.0	0.98	-19.30
A13-33	09:26:08.129	76:14:12.677	136.06	35.11	11.0	1.01	-63.33
A13-34	09:06:12.992	66:48:03.906	147.46	37.85	11.3	0.98	-7.87
A13-35	09:11:42.487	70:03:57.233	143.41	37.08	10.6	0.99	-33.01
A13-36	07:49:59.852	66:26:33.043	149.60	30.52	10.3	1.09	-65.10
A13-37	08:55:51.839	61:47:33.222	153.95	38.26	11.0	1.02	-26.50
A13-38	08:17:34.609	49:28:18.893	169.73	33.98	10.2	0.97	8.34
A13-39	08:28:13.251	16:54:09.735	207.70	28.79	10.4	0.99	49.39
A13-40	08:33:42.249	43:06:22.243	177.74	36.30	10.6	1.00	15.13
A13-41	07:59:56.525	62:46:26.405	153.85	31.69	10.4	1.04	-82.40
A13-42	07:01:45.303	68:40:26.404	146.79	26.06	10.5	0.99	-49.70
A13-43	07:24:12.254	59:29:12.056	157.34	27.21	10.2	1.09	-7.00
A13-44	07:29:55.636	57:16:14.062	159.93	27.65	10.3	0.97	-11.80
A13-45	07:55:41.652	48:29:54.348	170.46	30.31	10.6	0.99	7.90
A13-46	08:49:13.885	65:01:35.053	150.24	36.73	10.1	0.99	-52.97
A13-47	08:49:36.694	71:38:03.626	142.44	34.82	10.1	1.03	-46.50
A13-48	08:49:41.649	68:02:28.969	146.62	35.95	10.2	1.03	-62.90
A13-49	07:53:27.324	65:28:07.281	150.73	30.90	10.0	0.99	-27.00
A13-50	08:54:29.650	68:49:42.966	145.53	36.13	10.1	1.01	-135.90
A13-51	10:06:27.035	78:40:29.956	132.07	35.35	10.4	1.01	-168.40
A13-52	07:18:30.077	75:01:01.695	139.82	27.88	10.3	1.06	-58.50
A13-53	07:25:52.871	73:40:51.867	141.34	28.36	10.8	0.97	-58.10
A13-54	07:34:21.413	75:17:22.661	139.49	28.89	10.6	1.05	-113.10

15
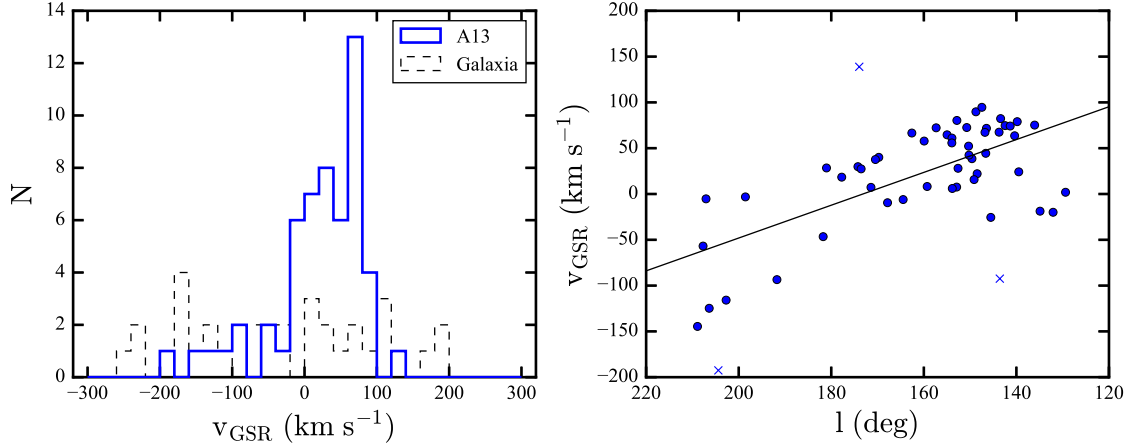
Figure 2.3: Distribution of the radial velocities in the Galactic standard of rest frame, v_{GSR}, for the stars in the A13 sample. Left panel: Histogram of v_{GSR} for 54 M-giant in A13. A clear peak shows up around 50 km s^{-1} . As a comparison, the distribution of v_{GSR} for stars in a mock catalog generated using Galaxia model (Sharma et al., 2011) with identical photometric and spatial properties as A13 is shown as the black dotted line. Right panel: A scatter plot of v_{GSR} vs. Galactic longitude for 54 M-giants in A13 is shown. v_{GSR} increases as the Galactic longitude of stars decreases, consistent with a prograde rotation. A linear fit with 2.5-σ rejected is applied and three stars are removed as outliers, shown as the crosses.

$$dv_{GSR}/dl = -1.57 \pm 0.28 \, \text{km s}^{-1}\text{deg}^{-1} \tag{2.2}$$

$$v_{GSR|180°} = -12.0 \pm 7.9 \, \text{km s}^{-1} \tag{2.3}$$

$\sigma_v \sim 40 \, \text{km s}^{-1}$ is much colder than the velocity dispersion for the kinematics of random halo stars as shown from the Galaxia sample, but hotter than the v_{GSR} dispersion of most of the known stellar streams, such as the Sagittarius tidal stream ($\sigma_v \sim 10$ km s^{-1} ; Majewski et al., 2004) and the Orphan stream ($\sigma_v \sim$ 10 km s^{-1} ; Newberg et al., 2010). The velocity dispersion of A13 is close to the kinematics of disk stars.

2.3.2.3   Metallicities

Ca II triplet (CaT) has been historically used to determine the metallicity of the stars in the globular and open clusters (see e.g., Armandroff & Zinn, 1988; Rutledge et al., 1997; Cole et al., 2004; Warren & Cole, 2009; Carrera, 2012). Battaglia et al. (2008) show that CaT–[Fe/H] relations calibrated on globular clusters can also be applied with confidence to RGB stars in composite stellar populations. Carrera et al. (2013) derived a relation between the [Fe/H] , luminosity, and strength of the CaT lines using 500 RGB stars in clusters and 55 metal-poor field stars. So far, many other works have used this calibration relation to derive the metallicities for stars, especially in the dwarf spheroidal galaxies (see e.g., Hendricks et al., 2014; Simon et al., 2015). However, most of the RGB stars used in these calibration work has temperatures higher than our M-giant sample. Furthermore, as our sample has no precise distance measurement, the luminosities of the stars are unknown and we cannot use the relation derived from the aforementioned studies.

We therefore developed an empirical relation to derive the metallicities of the M-giants in the A13 sample. We collected 22 late spectral type giants with published metallicities in our 2014 McDonald run. In order to include more calibrators, we extend the range of $J - Ks$ color from $J - Ks > 0.97$ to $J - Ks > 0.82$. The information of the 22 red calibrators are listed in Table 2.3. The most metal-poor calibration star, HD 37828, with $J - Ks = 0.83$, is also the bluest star in the calibration sample. We included this star to get a wide metallicity range even though it is much bluer than our program stars. We think that including HD 37828 should not introduce large additional errors, as the rest 21 calibration stars do not show a correlation between the [Fe/H] and $J - Ks$.

We compute the spectral index around each of the Ca II triplet lines ($\lambda\lambda 8498$,

8542, 8662). The spectral indices are pseudo equivalent width (EW) measured in Å , which is defined as:

$$\mathrm{EW} = \int_{\lambda_1}^{\lambda_2} \left(1 - \frac{F_l(\lambda)}{F_c(\lambda)}\right) d\lambda \tag{2.4}$$

where λ_1 and λ_2 are the edges of bandpasses for the CaT lines, $F_l(\lambda)$ is the flux of the line and $F_c(\lambda)$ is the continuum flux. The continuum flux is computed as a linear fit using the red and blue continuum bandpasses. We tested the line and continuum bandpass definition both from Du et al. (2012) and Cenarro et al. (2001) to calculate the EW.

We use a simple sum of the three Ca II spectral indices as the total strength of the Ca triplet CaT, i.e.

$$\mathrm{CaT} = \mathrm{EW}_{8498} + \mathrm{EW}_{8542} + \mathrm{EW}_{8662} \tag{2.5}$$

We then derive a linear empirical relation between the CaT index and the published [Fe/H]. The bandpasses defined by Du et al. (2012) gives a smaller rms between the published and derived metallicities for the 22 metallicity calibrators. We, therefore, use the bandpasses defined by Du et al. (2012) for the final metallicity calibration relation. Our derived CaT–[Fe/H] relation for the 22 metallicity calibrators is shown as the solid line in the left panel of Figure 2.4. In the right panel of 2.4, the [Fe/H] derived from the CaT index is plotted against the [Fe/H] values from literature. The two dashed lines in the right panel are $\pm$ 0.25 dex away from the one-to-one line. As most of the derived [Fe/H] values for the calibrators fall within 0.25 dex of the published values, we conclude that the estimated error in the derived metallicities is ± 0.25 dex. In both panels, we also color-code the published log g value. The

stars with higher $\log g$ tend to have smaller CaT at a given metallicity. As CaT is the absorption lines from the ionized calcium, the line strength gets smaller for stars with larger surface gravity. From our calibration sample, the errors caused by the difference in surface gravity are smaller than 0.25 dex for giants with $1.0 < \log g < 2.5$.

We next apply this derived relation to our A13 sample with S/N > 25. 27 out of 51 A13 stars (as three are rejected as outliers from their kinematics) have S/N > 25 and their metallicities are calculated. The mean [Fe/H] derived from the CaT index for the 27 stars in A13 is [Fe/H] $= -0.57 \pm 0.21$, where $\pm$ 0.21 dex is the standard deviation of the metallicities for the 27 stars. The derived [Fe/H] from the 27 A13 stars span over -1.1 to -0.1, as shown in the left panel of Figure 2.4. It is possible that there are more metal-poor stars belong to this structure, while the color-cut with $J - K_S > 0.97$ discriminate the metal-poor stars from being the candidate stars.

As we mentioned early, in order to include more calibration stars, we extend the color range of the calibration stars to $J - K_S > 0.82$, while our program stars have $J - K_S > 0.97$. We also compute the CaT – [Fe/H] relation only using the 10 calibrators with $J - K_S > 0.95$. The derived mean [Fe/H] for the 27 program stars changes from -0.57 to -0.55. Moreover, since the CaT index tends to have a weak correlation with surface gravity as mentioned earlier, we also compute the CaT – [Fe/H] relation using 11 calibrators with $1.0 < \log g < 1.7$. The derived mean [Fe/H] changes from -0.57 to -0.63. We show that the systematic errors in the metallicity calibration from changing the restrictions of our calibration sample are less than 0.1 dex.

Table 2.3: Properties of the Giant Stars for Metallicity Calibration

ID	RA	Dec	V	J	K_S	$T_{\rm eff}$	$\log g$	[Fe/H]	REF[a]	EW[b]
HD 5780	00:59:23.3126	+00:46:43.563	7.65	5.37	4.22	3848	1.07	-0.70	1	7.58
HD 6833	01:09:52.2648	+54:44:20.278	6.77	5.00	4.04	4450	1.40	-1.04	2	7.09
HD 9138	01:30:11.1140	+06:08:37.760	4.84	2.52	1.66	4040	1.91	-0.39	3	7.74
HD 13520	02:13:13.3239	+44:13:53.954	4.84	2.34	1.33	3970	1.70	-0.24	3	8.44
HD 29139	04:35:55.2390	+16:30:33.490	0.86	-2.10	-3.04	3910	1.59	-0.34	3	8.76
HD 30834	04:52:37.9807	+36:42:11.463	4.79	2.32	1.39	4130	1.86	-0.37	3	8.50
HD 37828	05:40:54.6451	-11:12:00.191	6.88	4.89	4.06	4430	1.50	-1.39	4	6.41
HD 39853	05:54:43.6303	-11:46:27.098	5.64	2.90	1.98	3994	1.00	-0.40	1	8.03
HD 50778	06:54:11.3988	-12:02:19.067	4.09	1.54	0.64	4000	1.80	-0.37	3	8.17
HD 69267	08:16:30.9210	+09:11:07.957	3.52	1.19	0.19	4010	1.71	-0.24	3	8.83
HD 70272	08:22:50.1100	+43:11:17.272	4.26	1.26	0.38	3900	1.59	-0.03	3	9.11
HD 81797	09:27:35.2427	-08:39:30.958	2.00	-0.26	-1.13	4120	1.77	-0.12	3	9.07
HD 82308	09:31:43.2275	+22:58:04.690	4.32	1.45	0.59	3900	1.60	0.05	5	9.17
HD 90254	10:25:15.1953	+08:47:05.446	5.64	2.38	1.40	3706	1.40	-0.09	6	8.85
HD 99167	11:24:36.5902	-10:51:33.559	4.82	1.93	1.01	3930	1.61	-0.38	3	8.52
HD 112300	12:55:36.2086	+03:23:50.893	3.38	-0.11	-1.19	3652	1.30	-0.09	6	8.33
HD 115478	13:17:15.6278	+13:40:32.707	5.33	3.30	2.38	4240	2.21	-0.12	3	7.88
HD 183439	19:28:42.3299	+24:39:53.652	4.45	1.71	0.71	3847	1.40	-0.38	6	8.47
HD 211073	22:13:52.7295	+39:42:53.734	4.51	2.26	1.29	4110	1.94	0.02	3	9.11
HD 216174	22:49:46.3148	+55:54:09.999	5.44	3.58	2.63	4390	2.23	-0.53	1	7.40
HD 217459	23:00:42.9002	+03:00:42.491	5.85	3.91	2.94	4170	2.07	-0.18	3	8.00
HD 220009	23:20:20.5831	+05:22:52.701	5.08	2.89	1.99	4435	1.98	-0.64	7	7.17

[a]References: (1) Cenarro (2003), (2) Fulbright (2000), (3) McWilliam (1990), (4) Ryan & Lambert (1995), (5) Fernandez-Villacanas et al. (1990), (6) Smith & Lambert (1986), (7) Luck & Heiter (2007).
[b]EW is calculated using the bandpasses defined by Du et al. (2012)
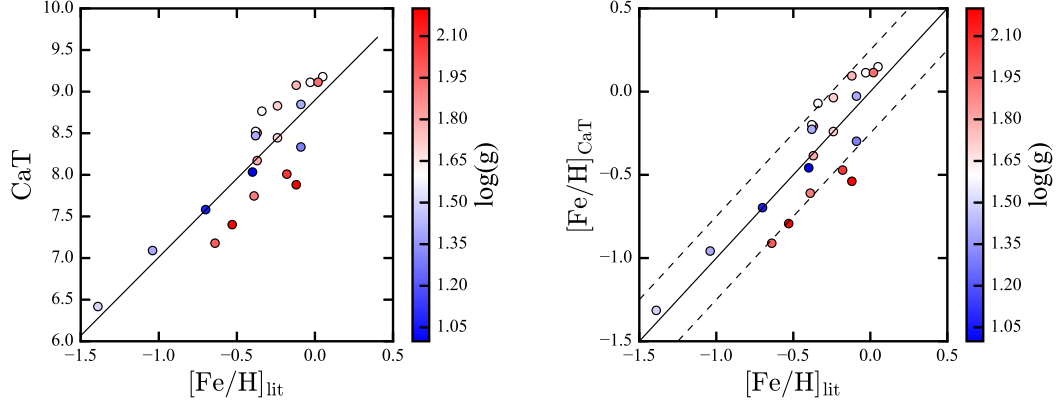
Figure 2.4: Metallicity calibration using 22 giant stars with known metallicities.Left Panel: CaT–[Fe/H] linear fit for 22 metallicity calibration giant stars, where CaT is the summation of the spectral indices from the near-IR calcium triplet. Right Panel: [Fe/H] derived from the CaT index vs. the published [Fe/H] values. The dashed lines are ± 0.25 dex away from the one-to-one (solid) line. For both panels, each symbol is also color-coded with its literature surface gravity log g.

2.3.2.4 Heliocentric Distance

In order to compute the distance, we adopted the metallicity dependent M_{K_S} – $(J - K_S)$ relation derived in S14. That is,

$$M_{K_S} = (3.8 + 1.3\,[\text{Fe/H}]) - 8.4(J - K_S). \tag{2.6}$$

For the 27 stars with calculated metallicity, the heliocentric distances were derived individually for each star using the $(J - K_S)$ color and [Fe/H] derived previously. As shown in the right panel of Figure 2.4, the heliocentric distance for A13 stars span over 10 to 22 kpc, with a mean of ∼15 kpc. S10 estimated the distance for A13 is 22.6 ± 11 kpc based on an assumption of a more metal-poor population. As a ±0.25 dex in [Fe/H] will change M_{K_S} for ±0.32 mag, the uncertainty of the distance derived here is roughly 15–20%.

21
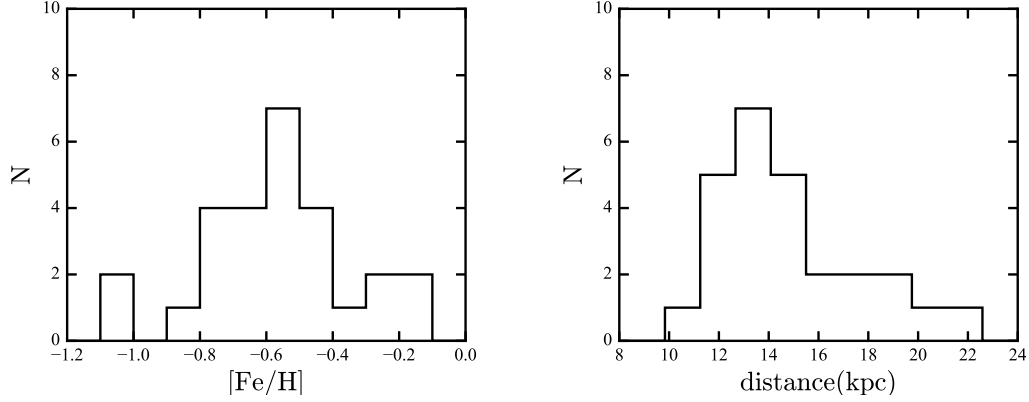
Figure 2.5: Distributions of metallicities and heliocentric distances of the A13 sample. Left Panel: Distributions of [Fe/H] derived from summing the calcium triplet spectral lines for 27 A13 stars with S/N > 25. Right Panel: Distributions of heliocentric distances of 27 stars, derived using an $M_{K_S} - (J - K_S)$ relation adopted from S14.

2.3.3   Discussion

2.3.3.1   Relation to the Galactic Anticenter Stellar Structure

Crane et al. (2003, here after C03) found a group of 53 M-giants that had a velocity distribution of $\sigma_v \sim 20\,\mathrm{km\,s^{-1}}$ in the direction of Galactic anticenter with a mean metallicity of $[\mathrm{Fe/H}] = -0.4\pm0.3$ and heliocentric distances of $d = 10-12$ kpc, which they refer as Galactic Anticenter Stellar Structure (GASS). This structure is also known as Monoceros Ring which is discovered independently using the MSTO stars from SDSS (Newberg et al., 2002). We found that our M-giant sample in A13 is also close to the Galactic anticenter and it follows a similar trend in radial velocities as the C03 sample, as shown in Figure 2.6. There is one star observed in both samples, which is the A13-01 in Table 2.2. The observed v_{hel} is 100.2 ± 5.3 km s^{-1} in our work and 95.6 ± 2.7 km s^{-1} in C03. The difference is 4.6 km s^{-1} , which is within the 1-σ joint uncertainty from both measurements.

As shown in the top panel of Figure 2.6, more than half of the C03 sample are

22
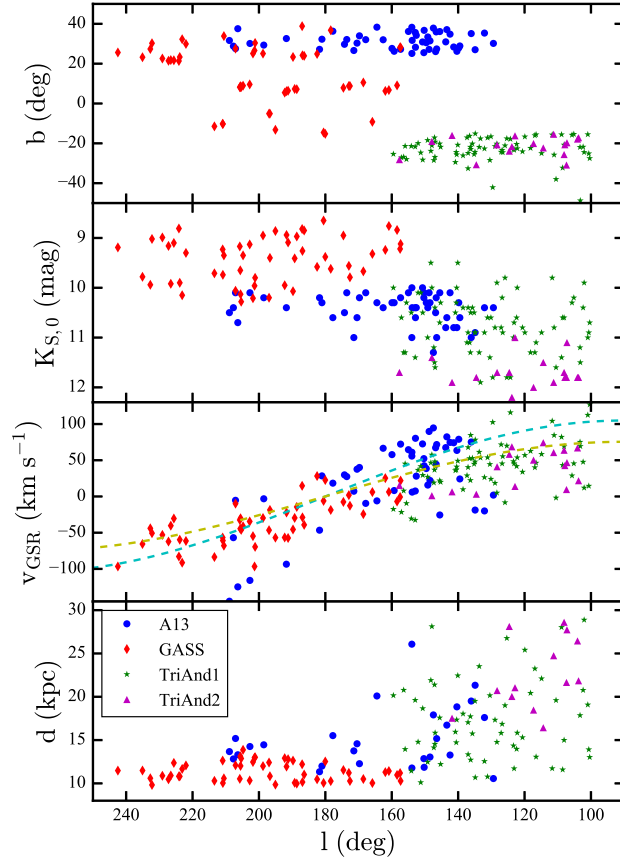
Figure 2.6: A comparison of A13, GASS, TriAnd1 and TriAnd2 on various properties. Panel (a): the position of the M-giants in different structure in Galactic coordinates. Panel (b): $K_{S,0}$ as a function of Galactic longitude. Since S10 made a cut on $K_{S,0} > 10$ so most of the A13 giants are fainter than the M-giants in GASS. Panel (c): Radial velocities in the GSR frame, v_{GSR}, as a function of Galactic longitude. Two dashed curves shows the expected v_{GSR} for an object orbiting circularly at 18 kpc (cyan) and 25 kpc (yellow) with $v_{circ} = 236$ km s^{-1} . 18 kpc is roughly the Galactocentric distance of GASS and 25 kpc is the Galactocentric distance of TriAnd (see Figure 2.7). Bottom Panel: Estimated heliocentric distance on individual M-giants using the relation shown in Section 2.3.2.4, as a function of Galactic longitude. The A13 stars with $l < 180°$ tend to be at the similar distance as GASS while those with $l > 180°$ tend to at the further distance close to TriAnd.

close to the galactic plane ($b \sim 20°$), stars in the A13 sample have $b > 25°$ due to the rectangular masks applied to avoid regions high dust extinction (see Section 3.2.2). We think the C03 sample were not picked by the group-finding algorithm in S10 as part of the A13 group mainly due to 2 reasons. First, about two-thirds of the C03 sample has $b < 25°$ and therefore they are excluded by the rectangular masks for extinction regions. Second, most of the C03 sample has $K_{S,0} < 10$ (see the second panel of Figure 2.6) while S10 made a cut of $K_{S,0} > 10$ on their initial sample selection to exclude the nearby stars.

Considering the location on the sky and velocity trend of the two structures, it is very likely that A13 structure is related to GASS or is part of GASS extended towards lower Galactic longitude. However, as most of the stars in A13 is fainter than GASS, the average heliocentric distance of A13 ($d \sim 15$ kpc) is further than GASS. As the heliocentric distance of some of the A13 stars extends to 20 kpc, it is further than any of the known extension of the Monoceros Ring from other tracers such as MSTO stars.

2.3.3.2   Relation to the Triangulum-Andromeda Cloud

Triangulum-Andromeda cloud (TriAnd) is another prominent substructure at distances of roughly $\sim$20–30 kpc at low Galactic latitude. It was first discovered as a "cloud-like" spatial overdensity by Rocha-Pinto et al. (2004) using the M-giants from 2MASS catalog, spanning the range $100° < l < 160°$ and $-50° < b < -15°$. Martin et al. (2007) subsequently detected two main-sequences in the region of TriAnd – referred as TriAnd1 and TriAnd2 – using the data from the MegaCam Survey. S04 conducted an expanded survey of M giants in the TriAnd region using 2MASS catalog, building on the M giant study of Rocha-Pinto et al. (2004). S04 found a brighter RGB sequence in additional to the faint one discovered by Rocha-Pinto
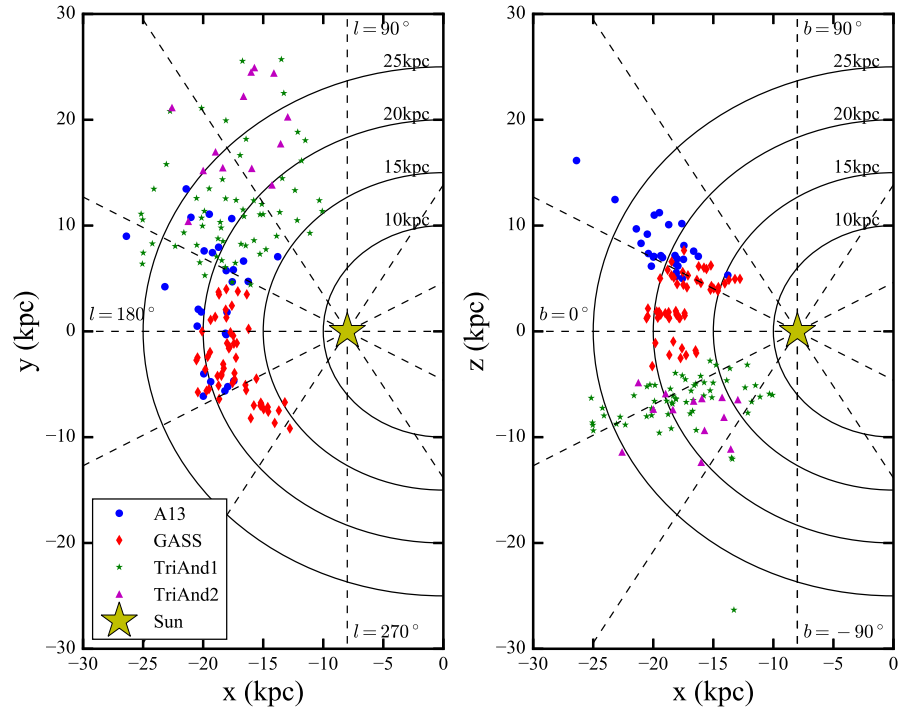
Figure 2.7: Distributions of M giants in A13, GASS, TriAnd1 and TriAnd2 shown in Galactocentric Cartesian coordinates. The Galactic Center is at (0, 0, 0) and the Sun is at (−8, 0, 0) kpc. Galactic longitude and latitude (dashed) and curves at constant Galactocentric radius (solid) are shown.

et al. (2004). The brighter sequence (TriAnd1) is younger (6-10 Gyr) and closer (distance of ∼15-21 kpc), while the fainter sequence (TriAnd2) is older (10-12 Gyr) and further (distance of ∼24-32 kpc). The velocity dispersion for both sequences is $\sigma_v \sim 25\,\mathrm{km\ s^{-1}}$.

Member stars in TriAnd1 and TriAnd2 from S04 are shown in Figure 2.6, together with the stars in A13 and GASS. Though the TriAnd stars are in a different part of the sky, the velocity trend of these four structures are similar – all of them follows a prograde rotation at $v_{GSR} = 236$ km s^{-1}, shown as the dashed curves in the third panel of Figure 2.6. For the M-giants with S/N > 25, the heliocentric distances of individual stars in each population are calculated in the same way as described in Section 2.3.2.4 and presented in the bottom panel of Figure 2.6. Although the uncertainty of distance measurements is large ($\sim 20\%$), there is a clear trend that the A13 stars with $l < 180°$ tend to be at the similar distance as GASS while those with $l > 180°$ tend to be at the further distance close to TriAnd. This could be obviously seen when we transfer the M-giants from Galactic spherical coordinates (l, b, d) to Galactocentric Cartesian coordinates (X, Y ,Z), assuming the Sun is at $(-8, 0, 0)$ kpc, shown in Figure 2.7.

Xu et al. (2015) suggested that Monoceros Ring (or GASS) and TriAnd are primarily the results of disk oscillations, where the northern ring associated with the Monoceros Ring is closer to the sun compared to the southern ring associated with TriAnd. If A13 is related to GASS, the fact that heliocentric distance of A13 spans to the distance of TriAnd could not be fit in this model, as we would expect the overdensity of M-giants in the north is closer to the sun than those in the south. If A13, GASS, TriAnd are from the same origin, the distance gradient we see as a function of galactic longitude (see the left panel of Figure 2.7) would be more in favor of the scenario where these M-giant overdensities are the result of an accretion event

from a dwarf galaxy, as suggested by Peñarrubia et al. (2005). However, such gradient is also possible due to some selection bias as the samples from GASS, TriAnd and A13 have different cut in color range as well as magnitude range when the samples were selected. A complete and unbiased study on all these M-giants with precise distance measurement from GAIA will help solve the mystery.

2.4 A11 Candidate

2.4.1 Observations and Data Reduction

62 stars out of 79 stars were observed using the High-Resolution Spectrograph (HRS) – a single object echelle spectrograph – on the Hobby-Eberly Telescope during Jan-Mar 2013 in queue observing mode. The exposure for each star is 10 minutes, with additional 10 minutes overhead time. The wavelength coverage is 5860–7860 Å with a spectral resolution of R~15,000. The typical signal-to-noise ratio of the spectra is around 10 per pixel. Bias frame and dome flats were taken in the afternoon before the observation starts. Arc frames with ThAr lamp were taken right before or after each exposure. Radial velocity standard stars and flux standard stars were also taken every night when the program stars were observed.

The data were reduced using the standard IRAF routine in the *echelle* package after bias subtraction and flat-fielding using the afternoon calibration frames. The *apall* task was used for one-dimensional extraction and *ecidentify* task was used for wavelength calibration. The dispersion solution was finally applied to the spectra using the *dispcor* task. All the spectra were then flux calibrated using the spectra of the flux standard star taken with the same echelle spectrograph. An example of the flux-calibrated multi-order combined spectra is shown in Figure 2.8. Since HRS has two chips, there is a gap around 6800 Å.
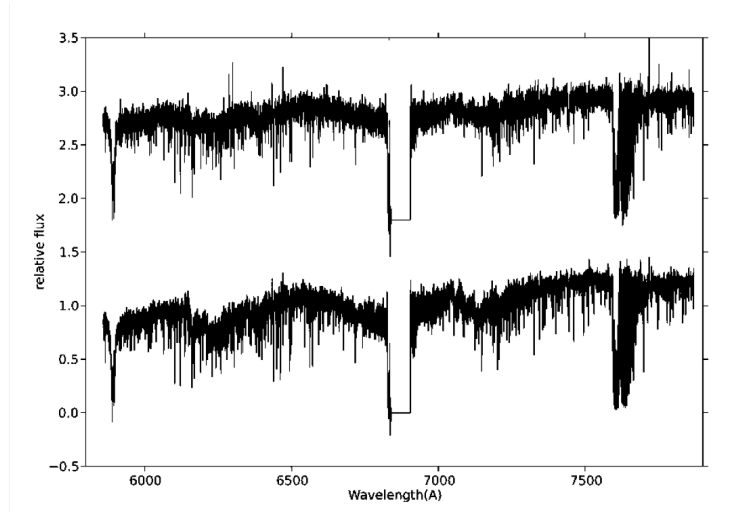
Figure 2.8: Example of flux-calibrated multi-order combined spectra of two stars in A11.

Table 2.4: Definitions of Spectroscopic Indices (Mann et al., 2012)

Index Name	Band (Å)	Continuum (Å)
Na D	5868–5918	6345–6355
Ba II/Fe I Mn I/Ti I	6470–6530	6410–6420
CaH2	6814–6846	7042–7046
CaH3	6960–6990	7042–7046
TiO5	7126–7135	7042–7046
K I	7669–7705	7677–7691, 7802–7825

2.4.2   Results and Discussion

We first examine whether or not these stars in A11 are giants. We measure the spectroscopic indices defined in Table 2.4, adopted from Mann et al. (2012). Surprisingly, the spectroscopic indices of these 62 A11 stars fall in the M-dwarf track (see Figure 2.9). As a comparison, we also compute the indices for the radial velocity standards, which are known as M-giants. It is very obvious that the majority of the A11 stars do not follow the track where M-giants lie.
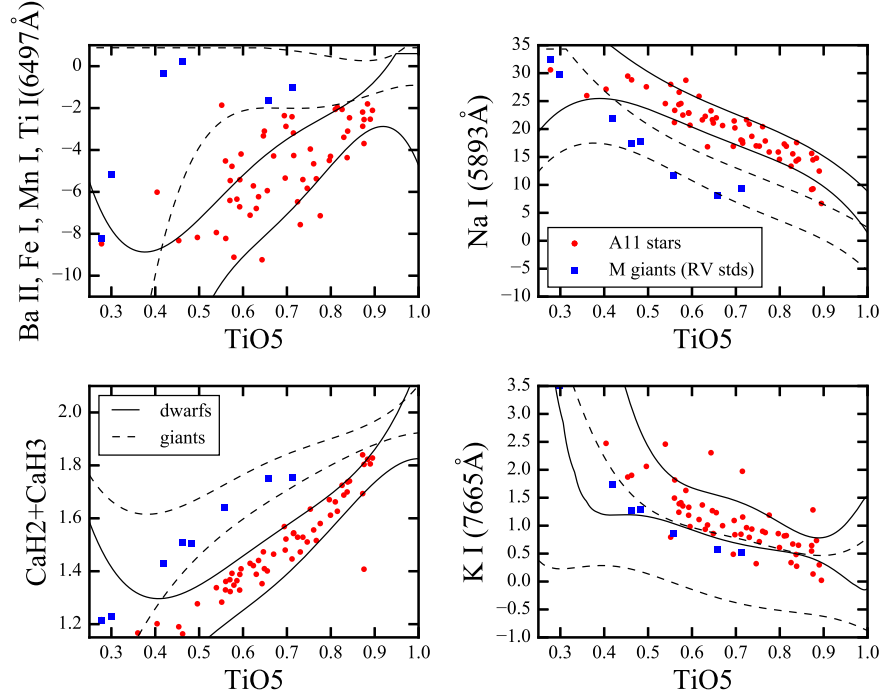
Figure 2.9: Spectroscopic indices for the stars in the A11 sample. The indices are adopted from Mann et al. (2012). Also plotted are the spectroscopic indices for the radial velocity standards from the same run, which are known as M-giants. Dashed and solid curves correspond to 90% intervals of giants and dwarfs training sets, adopted from Mann et al. (2012). It is obvious that the candidate stars in A11 do not follow the track where the M-giants lie.

Therefore, we conclude that most of the stars in A11 are foreground M-dwarfs instead of distance M-giants and A11 is a false detection. There are the following two possible explanations that this structure was selected as false positive. First, the structure might be associated with dust extinction in the low Galactic latitude. Second, there might be some position dependent systematic errors in 2MASS that some area has larger photometric errors than the other area. Since the M-giants are selected based on a color-color cut, the non-uniformity of photometric errors can cause false detection like the one discovered here.

2.5   Conclusions

We spectroscopically follow up the two candidate structures found by S10, named A13 and A11, which are selected using an M-giant catalog from 2MASS. The follow-up observations show that A13 has velocity dispersion of ~ 40 km s^{-1} and is a genuine structure. It is also kinematically consistent with the GASS structure found by Crane et al. (2003), so A13 is possibly associated with GASS. The Galactic latitude of this structure extends to $b \sim 40°$ and has a mean heliocentric distance of $\sim$15 kpc. On the other hand, most of the A11 stars turn to be foreground M-dwarfs, instead of expected M-giants. A11 is a false detection, probably due to the systematic photometric errors in 2MASS or dust extinction.

3. DISCOVERY OF A STELLAR OVERDENSITY IN ERIDANUS-PHOENIX IN THE DARK ENERGY SURVEY*

3.1   Introduction

Great progress has been made towards a better understanding of the formation mechanisms of the Milky Way and especially its stellar halo in recent years. This is due in large part to the deep, wide-field imaging surveys such as the Two Micron All Sky Survey (2MASS; Skrutskie et al., 2006) and the Sloan Digital Sky Survey (SDSS; York et al., 2000), which have enabled large-scale studies of the Milky Way Galaxy to its outermost radii, and have resulted in the discovery of a variety of new and interesting substructures that lie within the Milky Way's halo (Ivezić et al., 2012). Our understanding of the formation of the Galactic halo has therefore evolved from a simple Eggen, Lynden-Bell & Sandage (ELS; Eggen et al., 1962) monolithic collapse model to a much more complex and dynamic structure that is still being shaped by the merging of neighboring smaller galaxies (Searle & Zinn, 1978). This merger process is predicted by hierarchical ΛCDM models of galaxy formation (Steinmetz & Navarro, 2002; Bullock & Johnston, 2005; Font et al., 2011).

In addition to classical globular clusters (Harris, 1996, 2010) and classical dwarf galaxies (Mateo, 1998), these modern surveys have also discovered many low luminosity globular clusters (Koposov et al., 2007; Balbinot et al., 2013), a large number of ultra-faint dwarf galaxies (Willman et al., 2005a,b; Belokurov et al., 2006a; Zucker et al., 2006; Belokurov et al., 2007; Walsh et al., 2007), and stellar streams, which are thought to have originated from the tidal disruption of either dwarf galaxies (see, e.g.,

---

the Sagittarius stream; Majewski et al., 2003; Belokurov et al., 2006b) or globular clusters (see, e.g., the Palomar 5 tidal tails; Odenkirchen et al., 2001).

However, there are other structures that cannot be classified by one of these familiar designations. Modern wide field deep imaging surveys have enabled for the first time the discovery of large scale highly diffuse halo structures that can cover up to several hundred square degrees on the sky. Examples of these recently identified extended stellar distributions include the Virgo overdensity (Jurić et al., 2008) and the Hercules-Aquila cloud (Belokurov et al., 2007), both located about 20 kpc from the Sun, and the Pisces overdensity (Sesar et al., 2007) at a distance of about 85 kpc.

These overdensities have generally been identified by noting excesses of a particular stellar tracer in a restricted area of the sky. For example, excess halo stars were first found in the Virgo constellation (Vivas et al., 2001), $(l, b) = (285°, 60°)$, by using RR Lyrae stars as tracers. This structure is known as the Virgo stellar stream (VSS) and lies about 20 kpc from the Sun (Duffau et al., 2006). In a similar location in the sky, Jurić et al. (2008), working with a large sample of Milky Way disk and halo stars from SDSS, identified a very extended overdensity that stood out from smooth models of the Galaxy's thin/thick disks and halo at a heliocentric distance of $\sim$6–20 kpc. This structure is dubbed the Virgo overdensity (VOD) and appears to encompass an area as large as 1,000 deg^2. Bonaca et al. (2012) used a later data release from SDSS and estimated that the VOD spans at least 2,000 deg^2, with the true extent likely closer to 3,000 deg^2. There is likely a connection between the VSS and the VOD; however, the exact nature of that connection is still being debated as is the full orbit of the Virgo structures (Carlin et al., 2012).

The Hercules-Aquila (HerAq) cloud is another nearby, extended structure, covering a few hundred square degrees in the constellations of Hercules and Aquila. In

Galactic coordinates it is located near $l = 40°$ and spans from $b = +40°$ to $-40°$ in latitude. Its distance, inferred from the brightness and colors of the stars, is about 10-20 kpc from the Sun. Simion et al. (2014) also found a strong excess of RR Lyrae stars in a similar part of the sky, with a distance peaking at 18 kpc from the Sun.

The other similar halo structure currently known is the Pisces Overdensity (POD), which was identified at a distance of ~ 85 kpc in Pisces using RR Lyrae stars (Sesar et al., 2007; Watkins et al., 2009). Spectroscopic follow-up observations on the RR Lyrae stars confirmed that it is a genuine structure and suggested that it may be composed of two distinct kinematic groups (Kollmeier et al., 2009; Sesar et al., 2010). Analysis of M-giant candidates also showed an overdensity in approximately the same direction (Sharma et al., 2010). Furthermore, Nie et al. (2015) used the blue horizontal branch stars as tracers to determine its spatial extent, finding that POD may be part of a stream with a clear distance gradient.

These structures share a common diffuse cloud-like morphology with large extended structure in the sky. It is still unclear what the origin of these structures might be; they may be the remnants of dwarf galaxies that have been severely disrupted by interaction with the Milky Way's tidal field. It is also possible that they are stellar streams in the later stages of disruption, or streams which are viewed at certain points in their orbit (apogalacticon, perigalacticon) where the tidal dispersal mechanism is particularly effective (Johnston et al., 2008, 2012).

There are also two prominent low-latitude overdensities – the Monoceros Ring structure (Newberg et al., 2002; Yanny et al., 2003) and the Triangulum-Andromeda overdensity (TriAnd; Rocha-Pinto et al., 2004), one or both of which may be classified with the extended overdensities. The origins of these two overdensities are still under debate. While many studies argue that the Monoceros Ring and TriAnd are the remnants of past accretion events (Crane et al., 2003; Martin et al., 2004;

Peñarrubia et al., 2005; Sollima et al., 2011; Slater et al., 2014), recent works suggest the possibility that the Monoceros Ring and TriAnd may be the result of a strong oscillation in the outer disk which throws thin disk and thick disk stars to large scale heights (Xu et al., 2015; Price-Whelan et al., 2015).

We report here the discovery of an extended, diffuse stellar overdensity in the direction of constellations Eridanus and Phoenix using imaging from the first year of the Dark Energy Survey. We refer to this structure as the Eridanus-Phoenix (EriPhe) overdensity. Much like the structures described above, EriPhe covers an area of at least 100 $\deg^2$ and has a heliocentric distance of ~16 kpc.

We structure this section as follows: in Section 3.2, we describe our data sample and our search for extended overdensities using main sequence turn-off (MSTO) stars. We then perform a series of checks to confirm that the overdensity is genuine. We also estimate the surface brightness and total luminosity of EriPhe. In Section 3.3, we discuss the relation of this new stellar overdensity candidate to the other known overdensity structures. We also search the vicinity of EriPhe and note a possible association between this structure, the globular cluster NGC 1261, and a newly discovered stellar stream (Phoenix Stream, Balbinot et al., 2015). We conclude in Section 3.4.

3.2   Data and Analysis

3.2.1   The Dark Energy Survey

The Dark Energy Survey (DES, Abbott et al., 2005) is a wide-field optical imaging survey in the $grizY$ bands performed with the Dark Energy Camera (DECam) (Flaugher et al., 2015), which is installed at the prime focus of the 4-meter Blanco telescope at Cerro Tololo Inter-American Observatory. The DECam focal plane is comprised of 74 CCDs: 62 2k×4k CCDs dedicated to science imaging and 12 2k×2k

CCDs for guiding, focus, and alignment. DECam has a hexagonal 2.2 deg wide field-of-view and a central pixel scale of 0.263 arcseconds. The full survey is scheduled for 525 nights distributed over five years from 2013 August to 2018 February. This five-year survey will eventually cover 5,000 deg^2 in the Southern Galactic Cap to depths of $g = 24.6$, $r = 24.1$, $i = 24.4$, $z = 23.8$, and $Y = 21.3$ mag with 10 sigma detection for point sources (Rossetto et al., 2011). The first year of imaging data (Diehl et al., 2014) have been processed and the calibrated images are now public[1]. DES has internally constructed catalogs of sources from this first year of imaging data, which we refer to as the Year 1 Annual 1 (Y1A1) release, and we use the catalogs from the internal release to search for coherent stellar structures in the halo.

3.2.2 Sample

The Y1A1 release consists of $\sim$ 12,000 science exposures taken between 2013 August 15 and 2014 February 9 in the wide survey area. Most of the Y1A1 footprint is covered by 2 to 4 overlapping exposures. Each exposure is 90 s in $griz$ and 45 s in Y. The Y1A1 data release covers $\sim$1,800 deg^2, including $\sim$200 deg^2 overlapping with the Stripe 82 region of SDSS and a contiguous region of $\sim$1,600 deg^2 overlapping the South Pole Telescope (SPT) footprint (Carlstrom et al., 2011). This paper considers the data from the SPT footprint.

The science exposures are processed by the DES data management (DESDM) infrastructure (Gruendl et al., in prep). The pipeline consists of image detrending, astrometric calibration, nightly photometric calibration, global calibration, image coaddition, and object catalog creation. The SExtractor toolkit is used to create object catalogs from the processed and coadded images (Bertin & Arnouts, 1996; Bertin, 2011). The Y1A1 data release contains a catalog of $\sim$ 131 million unique

---

[1]http://www.portal-nvo.noao.edu/

objects detected in the coadded images. For a more detailed description of the DESDM image processing pipeline and the Y1A1 release, we refer to Sevilla et al. (2011), Mohr et al. (2012), Balbinot et al. (2015).

We selected our stellar sample from the Y1A1 coadd object catalog. The objects in the sample are classified using $spread\_model$, a star-galaxy indicator, provided by SExtractor. The $spread\_model$ variable is a normalized linear discriminant between the best-fit model of local point spread function (PSF) and a more spatially extended model. A good criterion to select stars is $|spread\_model| < 0.003$ (Desai et al., 2012). To avoid issues arising from fitting the PSF across variable-depth coadded images, we utilized the weighted-average (wavg) of the $spread\_model$ measurements from the single-epoch exposures. Here we use the weighted-average of the $spread\_model$ measurements in i-band $|wavg\_spread\_model\_i| < 0.003$ for star selection. Bechtol et al. (2015) shows that with this star selection criteria, the stellar completeness is $> 90\%$ down to magnitude $g \sim 22$, at which point it drops to $\sim 50\%$ by $g \sim 23$. We selected stars with $16 < g < 23$, as fainter sources $(g > 23)$ have an increased galaxy contamination rate, and brighter sources $(g < 16)$ are typically saturated in DECam exposures. We also apply two additional criteria based on the output from SExtractor, $flags\_\{g, r, i\} < 4$ [2] to ensure sample quality and $magerr\_psf\_\{g, r, i\} < 1$[3] to discard objects with large photometric errors. The typical statistical photometric errors for the sample are ~ 0.02 for $g < 21.5$ in the g-band and increase to ~ 0.05 at the faint limit $(g \sim 23)$.

Finally, the sample is corrected for Galactic extinction using dust maps from Schlegel et al. (1998) and the recalibrated scaling relation from Schlafly & Finkbeiner

---

[2] $flags < 4$ implies that object may have bright neighbors $(flags = 1)$ and/or might be deblended $(flags = 2)$.

[3] $magerr\_psf\_\{g, r, i\} < 1$ implies the photmetric errors in PSF magnitude are less than 1 mag in $g-$, $r-$ and $i-$band.

(2011) according to a Fitzpatrick (1999) reddening law.

3.2.3   Overdensity in MSTO Stars

MSTO stars have been used extensively in SDSS as a tracer to map the halo structure and probe new substructures within 30 kpc (see, e.g., Newberg et al., 2002; Jurić et al., 2008; Newberg et al., 2010). Here, we use our sample to select halo MSTO stars by including only those stars having $0.2 < (g - r)_0 < 0.4$, where the subscript 0 denotes the dereddened magnitude. We then study the density map of MSTO stars in different magnitude bins (i.e. different distances) to search for overdensities via visual inspection.

The upper panel of Figure 3.1 shows the density map of stars with $20.5 < g_0 < 22$. Assuming the average F turnoff star with age ~ 12 Gyr has $M_g \sim 4.5$, this magnitude range corresponds to a heliocentric distance of $\sim$15–30 kpc. The density is calculated as the number of stars per pixel area in unit of $counts/deg^2$. We define the *pixel area* as

$$\delta\Omega = \Delta l \times \Delta b \cos b \tag{3.1}$$

where Δl and Δb are 0.5°. The $\cos b$ factor is included so that the actual area of each pixel considered in the density calculation is proportional to the solid angle projected on the sky, even though the Cartesian projection is not an equal area projection. The map is then smoothed using a 2-D Gaussian kernel with a standard deviation of 0.5° in both l and b.

The two highest density regions in this map are located near $(l, b) \sim (270°, -35°)$ and $(l, b) \sim (345°, -40°)$. The former part belongs to the outskirts of the LMC; the latter one is likely the outskirts of the Galactic bulge as it is close to the center of the Galaxy. Apart from those two, we also see an extended overdensity at $270° < l <$
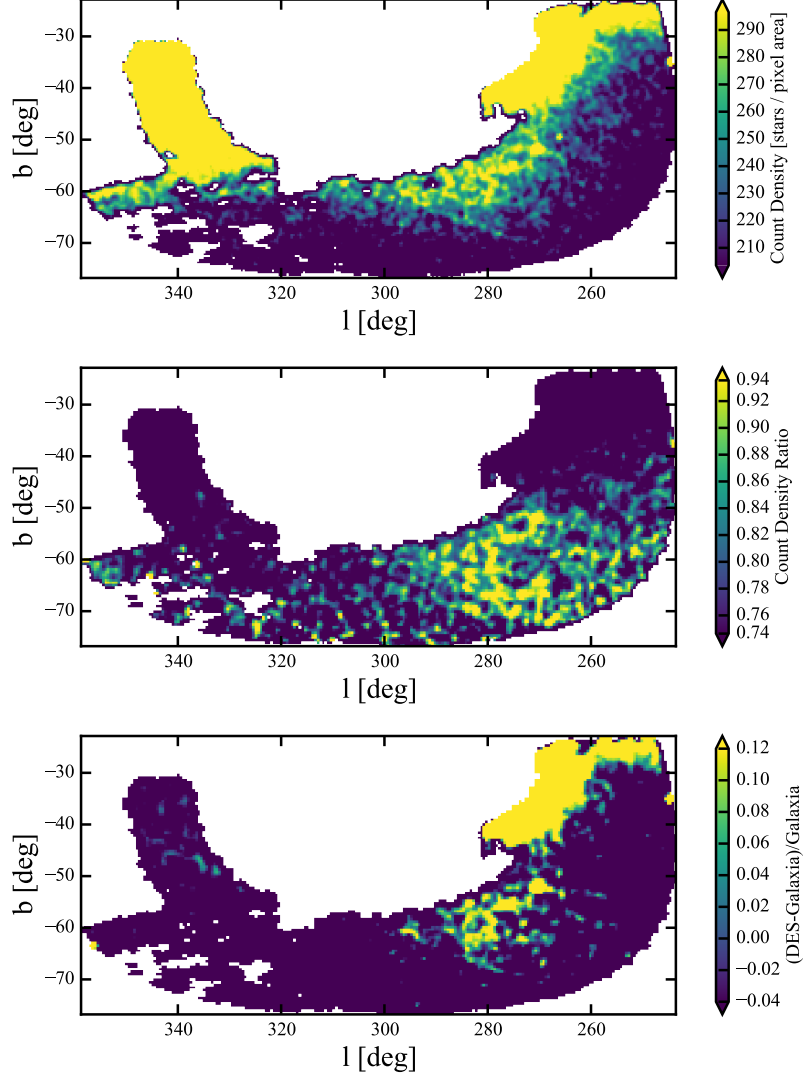
Figure 3.1: The surface density map from the Y1A1 data release. **Top Panel**: The surface density map for the DES SPT field from the Y1A1 data release. The sample is selected to be stars with $0.2 < (g - r)_0 < 0.4$ and $20.5 < g_0 < 22$. Each pixel is $\Delta l \times \Delta b = 0.5° \times 0.5°$. The histogram is then smoothed using a 2-d Gaussian kernel with a standard deviation of one bin in both l and b. **Middle Panel**: The density ratio map for the same area. The density of the stars with $0.2 < (g - r)_0 < 0.4$ and $20.5 < g_0 < 22$ is the numerator and the density of the stars with $0.2 < (g-r)_0 < 0.4$ and $18 < g_0 < 20.5$ and $22 < g_0 < 22.5$ is the denominator. **Bottom Panel**: The fractional difference density map (see text for details) between observed data from DES and mock data taken from a model galaxy constructed using `Galaxia`. The same cut, $0.2 < (g - r)_0 < 0.4$ and $20.5 < g_0 < 22$, is applied to both the DES data and the mock data. In all three panels, an overdensity around $l \sim 285°$ and $b \sim -60°$ is clearly seen, which is the EriPhe overdensity we refer to in this paper.
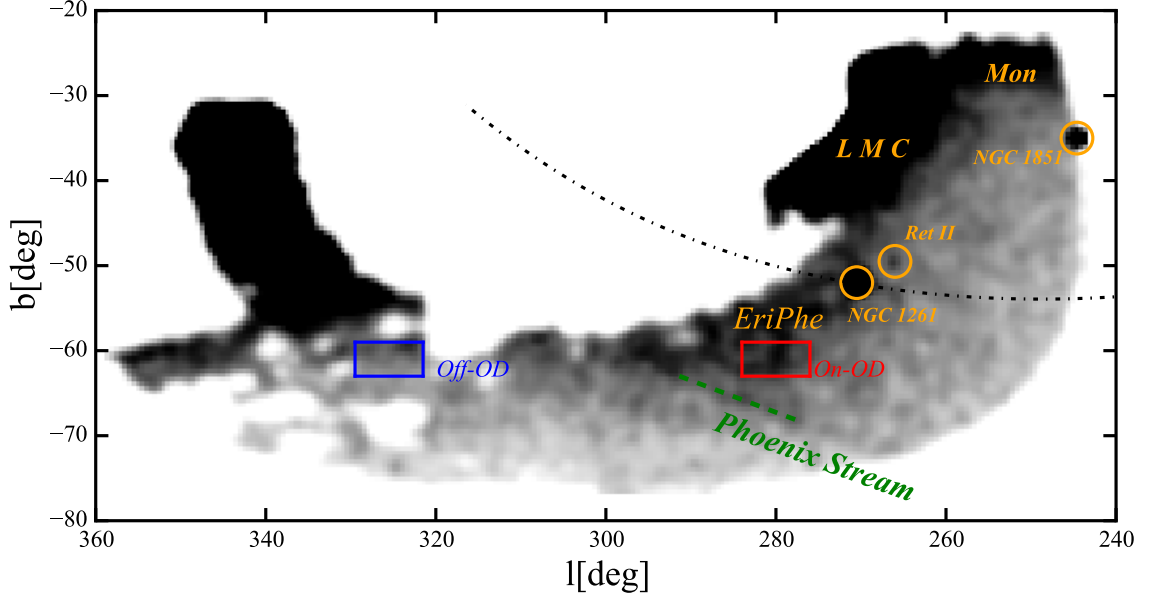
Figure 3.2: Reproduction of the density map with previously known Galactic structures identified. We highlight the overdensities from the LMC, the Monoceros Ring (Mon), and the newly discovered EriPhe. Other interesting objects such as NGC 1261, NGC 1851 and Ret II are labeled in the figure. The red square box and the blue square box are the on-OD field and off-OD field that used to construct the Hess diagram in Figure 3.4. Also plotted are the location of the Phoenix Stream (green dashed line) discovered by Balbinot et al. (2015), along with the integrated orbit of NGC 1261 (black dashed line) calculated using `galpy` (Bovy, 2015) and literature values for the proper motions (Dambis, 2006) and radial velocity (Harris, 2010).

$300°$ and $-65° < b < -55°$. We refer to this overdensity as the Eridanus-Phoenix (EriPhe) overdensity. Figure 3.2 shows a similar density map to the top panel of Figure 3.1, but with all the relevant substructure and fields used in our subsequent analysis explicitly labeled. For instance, it shows that the globular cluster NGC 1261, at $l \sim 270.5°$ and $b \sim -52°$, is located very near the EriPhe overdensity on the sky, as is the stellar stream in the Phoenix constellation (Balbinot et al., 2015), whose position is also indicated (see more discussion about this in Section 3.3).

In the middle panel of Figure 3.1, we compute the density ratio map. The numerator is the density of stars with $20.5 < g_0 < 22$ and the denominator is the density of stars with $18 < g_0 < 20.5$ and $22 < g_0 < 22.5$. This is essentially the ratio of the number of stars at a distance of $\sim$15–30 kpc, to the number of stars at closer or farther distances. In this density ratio map, the overdensities from the LMC and the center of the Galaxy in the density map disappear, as the LMC is located at $\sim$ 50 kpc and the stars from the Galactic bulge are located at < 10 kpc. The EriPhe overdensity stands out much more prominently in the middle panel. It is also worth noting that in this ratio map, the overdensity structure extends as low as b$\sim -70°$. However, this extension is not seen in the density map in the top panel. It is possible that EriPhe could extend beyond $b < -65°$, but it is hard to determine from the simply binned density map (i.e. top panel), as the background stellar density decreases with increased Galactic latitude.

We also compared the observational data with mock data generated by the `Galaxia` Galactic modeling code (Sharma et al., 2011). `Galaxia` is a code for generating a synthetic catalog of the Galaxy, using either an analytical input model or one obtained from N-body simulations. The synthetic datasets may be compared to wide-field imaging survey datasets like DES. Here we generated the mock data with a smooth analytical input model. The same color cut $0.2 < (g - r)_0 < 0.4$ and magnitude cut $20.5 < g_0 < 22$ are applied to the mock data from the `Galaxia` model. We then compute the fractional difference of the density map for the observed data from DES minus the `Galaxia` model to the `Galaxia` model, i.e.

$$\text{fractional difference} = \frac{\texttt{DES} - \texttt{Galaxia}}{\texttt{Galaxia}} \qquad (3.2)$$

as shown in the lower panel of Figure 3.1. `Galaxia` systematically overpredicts the

number of stars in the Galaxy relative to DES observations, because 1) the observed data from the DES Y1A1 catalog is not 100% complete at $g_0 \sim 22$ for stars and 2) the stellar counts predicted by `Galaxia` may also not be accurate at the depth of $g_0 \sim 22$. Nevertheless, the EriPhe overdensity stands out from a smooth background. Besides the EriPhe overdensity and the aforementioned LMC outskirts near $(l, b) \sim (270°, -35°)$, another overdensity near $(l, b) \sim (250°, -25°)$ is also visible. This overdensity is very likely to be associated with the Monoceros Ring, which is also labeled in Figure 3.2. We leave further discussion of this overdensity to future work.

From the three plots in Figure 3.1, we conclude that the EriPhe overdensity spans at least $270° < l < 300°$ and $-65° < b < -55°$. The full scope of the structure may extend farther; our current sample is limited by the coverage of the Y1A1 footprint.

We also perform a series of checks to make sure that this overdensity is not associated with any other systematics. We first check whether the overdensity appears at other heliocentric distance. The upper panel of Figure 3.3 shows the density map of stars with $18 < g_0 < 19.5$ (corresponding to a heliocentric distance of $\sim$5-10 kpc). The red dashed lines highlight the region of EriPhe. It is obvious that there is no overdensity in the same part of the sky at this heliocentric distance. The middle panel of Figure 3.3 shows the density map of non-stellar objects (selected using criteria $|wavg\_spread\_model\_i| > 0.003$) with $20.5 < g_0 < 22$ and same color range $0.2 < (g-r)_0 < 0.4$. This panel shows that EriPhe is not associated with the background galaxy distribution. We plot the distribution of the $E(B-V)$ color excess map from Schlegel et al. (1998) in the lower panel of Figure 3.3. The area enclosed by the red lines has a slightly higher $E(B-V)$ than other areas at the same latitude, by $\Delta E(B-V) \sim 0.015$. This difference in the color excess corresponds to a difference of extinction in $g-$band of $\Delta g \sim 0.05$ mag, provided that the reddening scaling relation $A_g/E(B-V) = 3.237$ from Schlafly & Finkbeiner (2011). We therefore investigate

the impact of dust obscuration on the EriPhe overdensity. We recalculate the density maps in the same way as in Figure 3.1 with a uniform dust map correction of $E(B - V) = 0.02$, and with no extinction correction. In both cases, the overdensity is still highly significant. We therefore conclude that dust extinction is not a likely explanation of the EriPhe overdensity structure.

3.2.4   Hess Diagram

We now examine the EriPhe overdensity in color-magnitude space. We build Hess diagrams constructed for the region of the sky that includes the overdensity (hereafter the on-OD field) and for a background region that appears less affected by this structure (hereafter the off-OD field). We construct a Hess diagram using stars having $-0.5 < (g - r)_0 < 1.0$ and $16 < g_0 < 23$. We select a 10° x 5° box centered at $(l, b) \sim (280°, -61°)$ as the on-OD field (red square in Figure 3.2); and another box of the same size centered at $(326°, -61°)$ as the off-OD field (blue square in Figure 3.2). The two fields are chosen to lie at the same latitude to minimize any latitude-dependent density changes. The coordinates are selected to minimize gaps in the off-OD field. However, there is still a small gap in the off-OD field, which is about 2% of the total area. The number of stars is therefore scaled to the sky coverage of the off-OD field.

The Hess diagrams for these two fields are shown in the left and middle panels of Figure 3.4. The total numbers of stars in the on-OD and off-OD field are 48,710 and 53,525, respectively. The off-OD field has more stars than the on-OD field in total, as it is closer to the Galactic bulge. However, the on-OD field possesses more stars with $0.2 < (g - r)_0 < 0.4$ and $20.5 < g_0 < 22$ than the off-OD field, 6,409 as compared to 5,429. Considering that the off-OD field has more stars in total, the Poisson significance of the detection is at least 9σ. We use the same color scale for these two
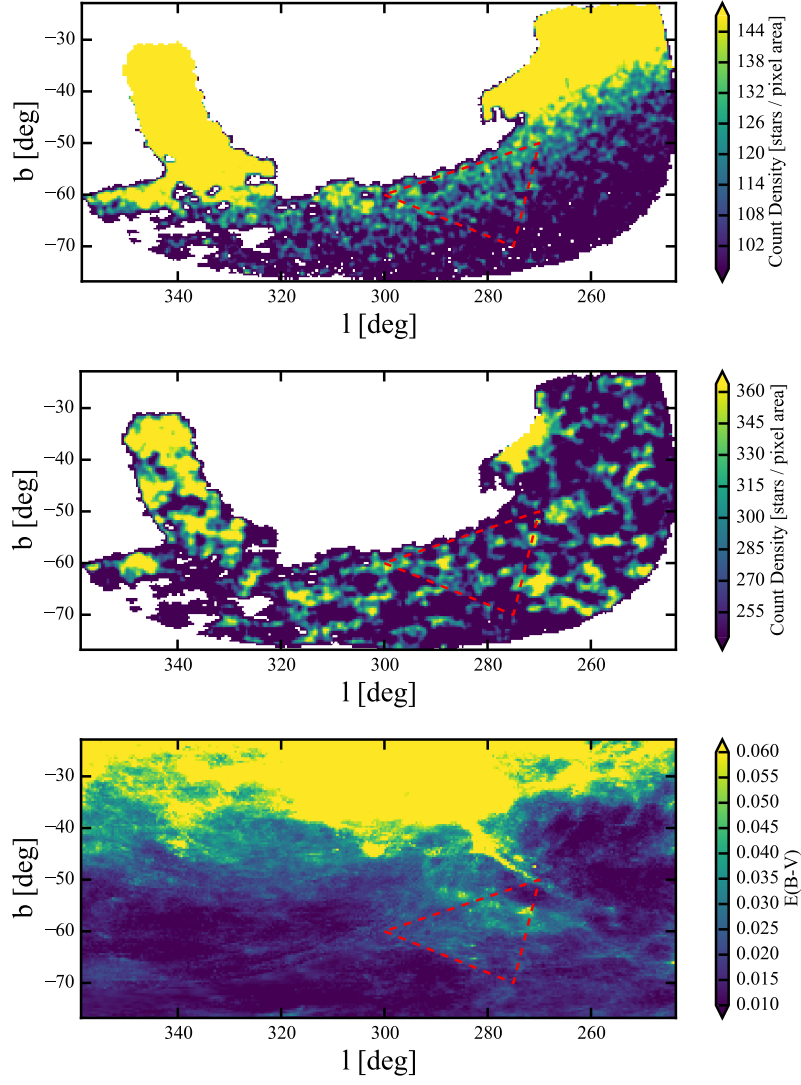
Figure 3.3: The surface density maps and extinction map of the same area. **Top Panel**: Similar surface density map as the top panel in Figure 3.1, but with $0.2 < (g - r)_0 < 0.4$ and $18 < g_0 < 19.5$, to check for overdensities at a difference distance. **Middle Panel**: Surface density map for non-stellar objects with $0.2 < (g - r)_0 < 0.4$ and $20.5 < g_0 < 22$. The non-stellar object are selected using criteria $|wavg\_spread\_model\_i| > 0.003$. **Bottom Panel**: $E(B - V)$ color excess map from Schlegel et al. (1998). In all three panels, the red lines highlight the region of the EriPhe overdensity.

43
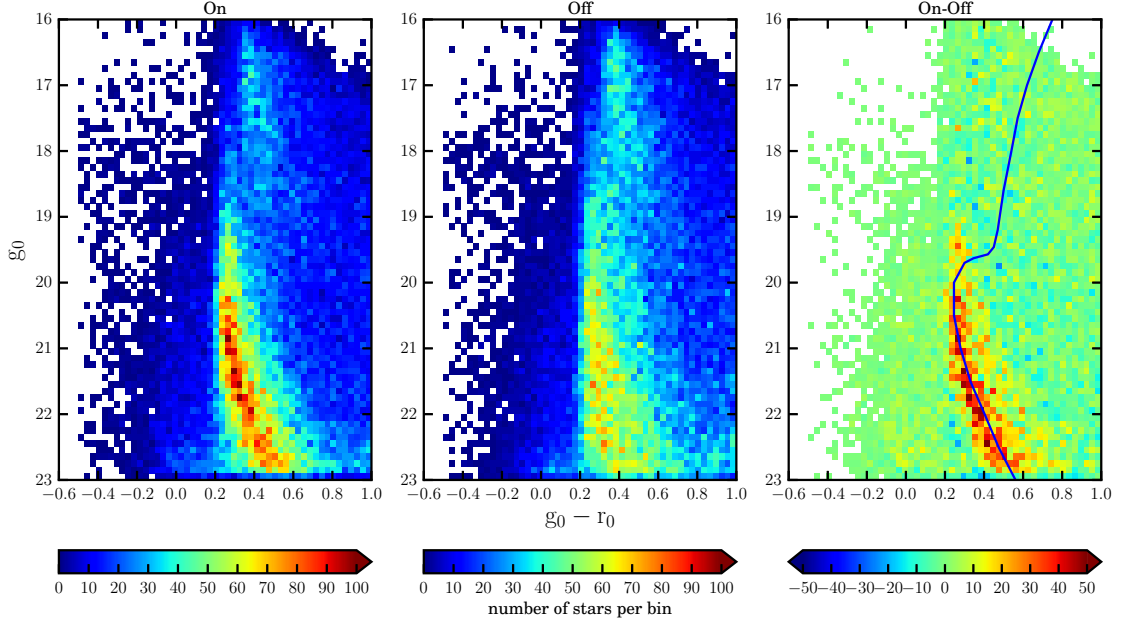
Figure 3.4: Hess diagram for the on-OD field (left panel) – a 10° x 5° box centered at $l = 280°$, $b = -61°$ (i.e. $275° < l < 285°$, $-63.5° < l < -58.5°$), off-OD field (middle panel) – box with same size centered at $l = 326°$, $b = -61°$ (i.e. $321° < l < 331°$, $-63.5° < l < -58.5°$), and the difference between the two (right panel). The coordinates are selected to minimize gaps in the survey coverage in the off-OD field. However, a small gap in the off-OD field is unavoidable and the off-OD counts are scaled with the sky coverage in this region. The pixel size in each of the three Hess diagrams is $\delta(g-r)_0 \times \delta g_0 = 0.03 \times 0.1$ mag. Also shown as the blue line in the right panel is the ridgeline of NGC 1261 from the DES data.

panels to make it apparent that the stars in the on-OD field have a narrower main sequence structure than the off-OD field, even though the on-OD has fewer stars in total. The difference map of the two fields, shown as the right panel in Figure 3.4, reveals a strong overdensity at $0.2 < (g - r)_0 < 0.5$ and $20.5 < g_0 < 22.5$. Also shown as a blue line in the right panel of Figure 3.4 is the ridgeline of NGC 1261. We obtained the photometry of the stars in NGC 1261 from the DES dataset and derived this empirical isochrone by calculating the median color for each magnitude bin in a step of $\delta g_0 = 0.2$ for MS stars and $\delta g_0 = 0.5$ for RGB stars. The isochrone matches the excess in the main sequence in EriPhe, showing that EriPhe has a heliocentric distance that is similar to that of NGC 1261. NGC 1261 has an age of ~ 10 Gyr, a metallicity of $[\text{Fe/H}] = -1$ and a heliocentric distance $d = 16.3$ kpc (Marín-Franch et al., 2009; Forbes & Bridges, 2010; Harris, 2010). While the NGC 1261 empirical isochrone fits the turn off fairly well, some differences in population are quite possible: there is some evidence that the age of the overdensity may be younger than that of the cluster as it may have a slightly brighter turnoff, though the red giant branch of the overdensity is too diffuse to be clearly seen in this color-magnitude diagram (see Figure 3.4).

We conclude that the Hess diagram analysis demonstrates the existence of a significant population of stars at a common distance around $l \sim 280°$ and $b \sim -61°$, with a magnitude range $20 < g_0 < 22.5$.

3.2.5   Surface Brightness and Total Luminosity

We follow a similar procedure as Jurić et al. (2008) to estimate the surface brightness of the EriPhe overdensity. We sum the fluxes of excess stars in the on-OD field compared to the off-OD field and then divide the total flux by the area of the $10°$ x $5°$ box centered at $b = -61°$, which is roughly 25 deg^2 or 3.2 x 10^8 arcsec^2 projected

on the sky. We only count the fluxes of stars satisfying $0 < (g - r)_0 < 0.7$ and $19 < g_0 < 22.5$ to minimize the contamination from the background. As the off-OD field has a larger total number of stars than the on-OD field, as stated in Section 3.2.4, the total sum of the number of counts in the difference map is actually negative – it is clear to see the overdensity of a main sequence (yellow-to-red coded) and the underdensity elsewhere (blue-coded) in the difference map (right panel of Figure 3.4). We therefore first scaled the number of stars in the off-OD field by a scale factor of 0.80. This is the ratio of the stars with $17 < g_0 < 19$ in two fields, as we assume that the background distribution in this magnitude range is not affected by the overdensity structure. We then calculate the excess stars by using the number of stars in the on-OD field minus the scaled number of stars in the off-OD field. We obtain a value of $\Sigma_r \sim 32.8$ mag arcsec^{-2}. This is about 1.8 mag fainter than the surface brightness of the Sagittarius dwarf Northern stream (Martínez-Delgado et al., 2004) and 0.3 mag fainter than that of the Virgo Overdensity (Jurić et al., 2008). This value is effectively a lower limit because it does not account for stars brighter than $g_0 \sim 19$ and dimmer than the limiting magnitude ($g_0 \sim 22.5$). We therefore applied a luminosity correction by adopting the luminosity function and isochrone from Dotter et al. (2008) with age = 10 Gyr, [Fe/H] = -1 and distance modulus $m - M = 16.06$, assuming that the age, metallicity and heliocentric distance of EriPhe are the same as NGC 1261. The surface brightness corrected to the full magnitude range is $\Sigma_r \sim 31.7$ mag arcsec^{-2}. It is worth noting that this calculation assumes that the EriPhe overdensity fully covers the entire 10° x 5° box. The surface brightness will be underestimated if this $10° \times 5°$ box is much larger than the region where an excess of stars related to EriPhe is present.

We also estimate the total luminosity for EriPhe. First, we assume the surface brightness derived above is uniform across the overdensity structure and equal to

$\Sigma_r \sim 31.7$ mag arcsec^{-2}. Second, we assume it spans over ~ 150 deg^2 ($270° < l <$ 300° and $-65° < b < -55°$ is about ~ 150 deg^2 projected on the sky). Then, from the surface brightness, we estimate the integrated apparent r-band magnitude to be $m_r = 8.4$. Assuming the heliocentric distance is the same as the globular cluster NGC 1261, we convert the integrated absolute r-band magnitude to be $M_r = -7.7$. Using the relation from Jurić et al. (2008), we estimate that EriPhe has a total luminosity of $L_r \sim 9 \times 10^4 L_\odot$. We acknowledge that this estimate has very large uncertainties. First, the distribution of EriPhe is not uniform and may also be smaller or larger than the assumed 150 deg^2. Second, as mentioned earlier, the full scope of EriPhe is limited by the Y1A1 coverage; the structure may extend farther.

We also estimate the total luminosity in an independent way as follows. We first calculate the total number of stars with $0 < (g - r)_0 < 0.7$ and $20.5 < g_0 < 22$ that belong to the EriPhe overdensity by scaling the mock data from `Galaxia` so that the number of stars in `Galaxia` and the number of stars in the DES data match in the region where the counts are not affected by the EriPhe overdensity, and then summing the counts of the difference between the DES data and the scaled mock data. We get a total of $\sim 21,000$ stars in EriPhe with $0 < (g - r)_0 < 0.7$ and $20.5 < g_0 < 22$. Second, we again adopt the luminosity function and isochrone from Dotter et al. (2008) and scale the luminosity function so that there are a total of 21,000 stars within the magnitude range $20.5 < g_0 < 22$. Then we sum over the full magnitude range and get a total luminosity of $\sim 11 \times 10^4 L_\odot$. The results estimated using these two different methods are roughly consistent.

3.3   Discussion

In the past few years, much theoretical work on the formation of the Milky Way's stellar halo has focused on the tidal stripping and disruption of satellite galax-

47

ies (White & Frenk, 1991; Bullock & Johnston, 2005; Cooper et al., 2010) that are accreted by the Milky Way according to the hierarchical halo formation picture. N-body numerical simulations have predicted that the stellar halo is not a single smooth component, but instead a superposition of many tidal features. Indeed, many halo substructures have been found in the past decade, many of which are believed to be the remnants from past merging events.

In this section, we suggest two possible origins of the existence of the EriPhe overdensity formed from tidal stripping and disruption of satellite galaxies.

3.3.1 Connection to NGC 1261 and the Phoenix Stream

The globular cluster NGC 1261 (highlighted as a circle in Figure 3.2), at $l \sim 270.5°$, $b \sim -52°$ (Harris, 2010), is located near the edge of the EriPhe overdensity. We note that Carballo-Bello et al. (2014) report an unexplained background population around NGC 1261, with similar Galactocentric distance to the cluster, when the region is compared to a Galactic model. They suggested that this population either is disrupted material from the cluster or is an unknown stellar population in the halo. We believe this background is very likely to be part of the EriPhe overdensity. The discovery of EriPhe supports the second suggestion since a disrupting cluster is unlikely to create such a large overdensity on only one side of the cluster.

The EriPhe overdensity is also located very near to the Phoenix Stream found by Balbinot et al. (2015). Specifically, the Phoenix Stream lies at one edge of the EriPhe overdensity at $(l, b) = (284.4°, -66.0°)$ to $(l, b) = (294.8°, -61.1°)$ (highlighted as dashed green lines in Figure 3.2). The heliocentric distance of the Phoenix stream is ~ 17.5 kpc. It is noteworthy that the Phoenix stream, NGC1261, and EriPhe are all located at similar Galactocentric distances (~ 18 kpc) and projected locations.

To determine whether NGC 1261 could be associated with EriPhe and the Phoenix Stream, we compute the orbit of NGC 1261 with `galpy` (Bovy, 2015) using its proper motions (Dambis, 2006) and radial velocity (Harris, 2010). The integrated orbit is shown as a black dash-dotted line in Figure 3.2. This orbit roughly aligns with the orientation of the elongated structure of the Phoenix stream, suggesting that these two objects could have shared a Galactic orbit before the presumably more massive structure that resulted in the stream was tidally disrupted along its orbit. Therefore, a possible accretion scenario is that EriPhe is the remains of a dwarf galaxy that initially carried NGC 1261 and the progenitor of the Phoenix stream. EriPhe and the progenitor of the Phoenix stream could have been tidally disrupted as they were drawn into the Milky Way potential, while NGC 1261 was compact enough to avoid major tidal stripping, or at least none observable with current photometric data. NGC 1261 has an age of $\sim$10 Gyr and a metallicity of [Fe/H]$= -1.0$, suggesting that it is a quite young globular cluster (Marín-Franch et al., 2009). Many of the Milky Way's other young globular clusters are thought to have originated in dwarf galaxies (Zinn, 1993; Marín-Franch et al., 2009), and we suggest that the same is true for NGC 1261.

3.3.2 A Possible Polar Orbit Formed by EriPhe, VOD, and HerAq?

As discussed in the Introduction, the VOD is a large, diffuse stellar overdensity that extends over 1,000 deg^2 in the Northern hemisphere, while HerAq is a similarly diffuse overdensity extending several hundred square degrees. In comparison with EriPhe at a heliocentric distance of $\sim$16 kpc, the VOD is located at a heliocentric distance of 6-20 kpc, while HerAq has a heliocentric distance of 10-20 kpc.

Jurić et al. (2008) proposed a possible explanation for the existence of the VOD as part of a larger "Polar Ring" structure, forming a ring of overdense regions at the

same Galactocentric radii and centered on the Galactic center. However, they were unable to locate a counterpart in the Southern hemisphere by searching the 2MASS catalog for M giants as tracers of the potential ring structure. The discovery of EriPhe makes such a hypothesis more plausible. We carry the Polar Ring suggestion one step further by noting that a circular orbit with radius ~ 18 kpc from the Galactic center passes through both EriPhe and VOD and intercepts as well the HerAq cloud on the opposite side on the Galactic plane around $l \sim 40°$ at a heliocentric distance ~ 20 kpc. We suggest that the existence and location of these three structures could possibly be explained by a circular Galactic polar orbit. An illustration of the locations and rough spatial extents of the three structures, along with the projected circular polar orbit, is given in Figure 3.5. This polar plane is also very close to the Vast Polar Structure (VPOS) plane, which is fit to the distribution of Milky Way satellite galaxies (see, e.g., Pawlowski et al., 2012, 2015). It is, therefore, possible that EriPhe, VOD, and HerAq are the remnants left behind by a single dwarf satellite near the VPOS plane that has been largely or completely destroyed by the Milky Way's tidal field.

Carlin et al. (2012) measured the three-dimensional space velocities of stars and showed that the Virgo progenitor was on an eccentric ($e \sim 0.8$) orbit with an inclination of 54°. This observational evidence seems to disprove our polar orbit argument. However, Duffau et al. (2014) suggested that VOD appears to be composed of several halo substructures. If the scenario of multiple substructures in the VOD is true, then it is possible that one of them has a polar orbit.

We also note that the circular polar orbit hypothesis would predict the motion of the stars in EriPhe in the opposite directions to the alignment of the Phoenix stream. Furthermore, the circular orbit cannot explain the discontinuities between VOD, HerAq, and EriPhe. Since the separations of these three overdensities are
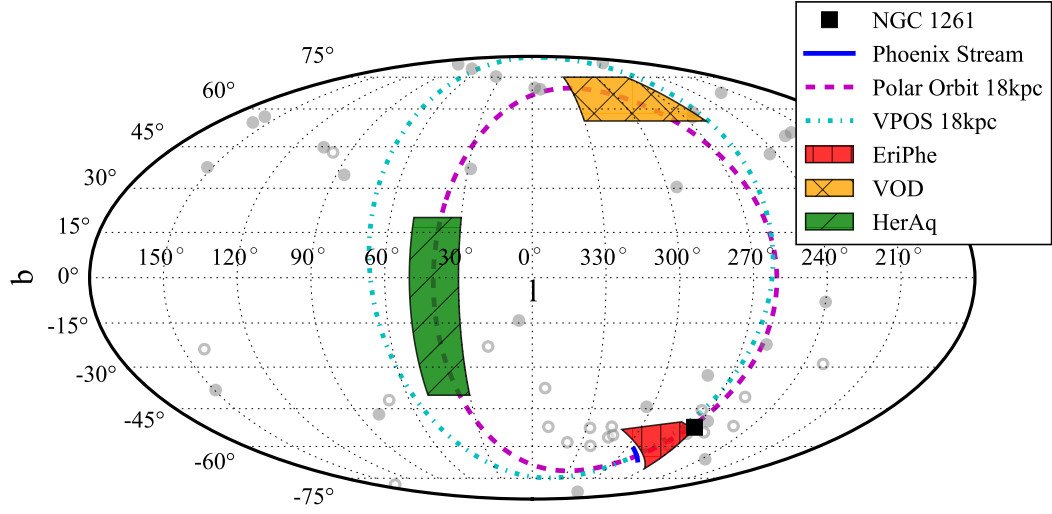
Figure 3.5: Mollweide projection of the known overdensities discussed in Section 3.3. A circular polar orbit at a Galactocentric distance of 18 kpc is shown as the purple dashed line. This orbit connects the EriPhe (red), VOD (orange) and HerAq (green), which are highlighted as patches using different colors. As comparison, an orbit at Galactocentric distance of 18 kpc on the VPOS plane using the VPOS+new fit from Pawlowski et al. (2015) is shown as the cyan dashed-dotted line, together with the confirmed dwarf galaxies in grey filled circles and dwarf galaxy candidates in grey open circles (McConnachie, 2012; Bechtol et al., 2015; Koposov et al., 2015; Drlica-Wagner et al., 2015; Kim et al., 2015; Kim & Jerjen, 2015; Martin et al., 2015; Laevens et al., 2015). Also plotted are NGC 1261 (black filled square) and the Phoenix Stream (blue solid line).

roughly 120° from each other, it is also possible that the disrupted progenitor satellite is in an eccentric orbit with a "trefoil" shape. These overdensities could be the remnants from the satellite disrupted over several passages, piling up approximately at turning points (see, e.g., spherical shells in Figure 4 of Hayashi et al., 2003). Alternatively, these three structures could each have had separate progenitors and have fallen into the Milky Way halo as a group or been accreted along a filament (Libeskind et al., 2005; Zentner et al., 2005; Wang et al., 2013). N-body simulations show that tidal stripping is most efficient when the satellites have close passage to the Galactic center and may even lead to total disruption of satellite galaxies (Bullock & Johnston, 2005; Cooper et al., 2010). The resulting diffuse structures are particularly common at small distances from the Galactic center and can be tidal debris from either one single massive progenitor or multiple smaller ones (Helmi et al., 2011). The validation of either of these hypotheses needs further studies from both observations and simulations.

3.4   Conclusions

We report the discovery of a Galactic halo stellar overdensity in the Southern hemisphere from the first annual internal release catalog of the first year DES data. This overdensity resides in the constellations of Eridanus and Phoenix, centered around $(l, b) \sim (285°, -60°)$ and spanning at least 30° in longitude and 10° in latitude. The full scope of the Eridanus-Phoenix (EriPhe) overdensity may extend farther, but it is limited by the coverage of the first year data. The stellar population in the overdense region has a similar distribution in color-magnitude space as the nearby globular cluster NGC 1261, indicating that the heliocentric distance of EriPhe is about $d \sim 16$ kpc and the Galactocentric distance is about $d \sim 18$ kpc. We propose two possible scenarios for the creation of the EriPhe overdensity which

both involve the tidal stripping and disruption of satellite galaxies. One suggests that EriPhe might be associated with the Phoenix stream and NGC 1261; the other one suggests a possible polar orbit structure formed by EriPhe, VOD, and HerAq stellar overdensities.

Whether or not EriPhe is part of the polar orbit structure, or it is the remnant of a dwarf galaxy with two globular cluster companions (i.e. NGC 1261 and the progenitor of the Phoenix Stream), needs to be tested with future observations. Proper motions measured by Gaia may further inform which hypothesis is favored. Moreover, spectroscopic follow-up on the Phoenix stream and EriPhe can provide more information on the kinematics and metallicities of these two structures, and improve our understanding of the nature of the EriPhe overdensity. Further study of cloud-like overdensities like EriPhe can also provide insight to probing the gravitational potential of the Milky Way (Sanderson & Helmi, 2013).

Finally, the second year of DES observations expand the sky coverage of the survey data by adding $\sim$3,000 deg^2. The third, fourth, and fifth years of DES observations will increase the depth and uniformity of imaging over the entire 5,000 deg^2 survey footprint. Since EriPhe is located near the edge of the footprint of the first year data, a more complete view of EriPhe will be revealed as additional data are acquired.

4. THE AUXILIARY SYSTEMS IN THE DARK ENERGY SURVEY [*]

4.1   The Dark Energy Survey and the Dark Energy Camera

The Dark Energy Survey (DES) is an imaging survey of 5,000 $\deg^2$ of the Southern sky, using the Dark Energy Camera (DECam; Flaugher et al., 2015), a new imager with a 2.2° diameter field-of-view mounted at the prime focus of the Victor M. Blanco 4 meter (4m) telescope on Cerro Tololo Inter-American Observatory (CTIO) near La Serena, Chile. The camera was designed and constructed by the DES Collaboration. The 570-megapixel focal plane comprises 62 2k $\times$ 4k CCDs for imaging and 12 2k $\times$ 2k CCDs for guiding and focus. The CCDs have 15 μm $\times$ 15 μm pixels with a central pixel scale of 0.263" pixel^{-1} and 20 seconds readout time.

The main science goal of DES is to determine the Dark Energy equation of state w and other key cosmological parameters to high precision. DES will measure w using four complementary probes: counts of galaxy clusters, weak gravitational lensing, galaxy power spectra from large scale structure and Type Ia supernovae. DES is expected to measure 300 million galaxies with photometric redshifts in the 5,000 $\deg^2$ main survey field and thousands of Type Ia supernovae in 10 supernova fields over a total of 27 $\deg^2$ (Dark Energy Survey Collaboration et al., 2016).

The first light of DES was obtained in September 2012, followed by commissioning of DECam and scientific verification from November 2012 to February 2013. The full survey is scheduled for 525 nights distributed over five years from 2013 August to 2018 February (approximately 100 nights per year). Five optical filters ($grizY$) were used throughout the five-year survey, with typical single exposure times of 90 seconds

---

[*]Part of this session is reprinted with permission from "Monitoring the atmospheric throughput at Cerro Tololo Inter-American Observatory with aTmCam" by Li et al., 2014. Proceedings of the SPIE, Volume 9147, Ground-based and Airborne Instrumentation for Astronomy V, id. 91476Z, 12 pp., Copyright 2014 by SPIE.
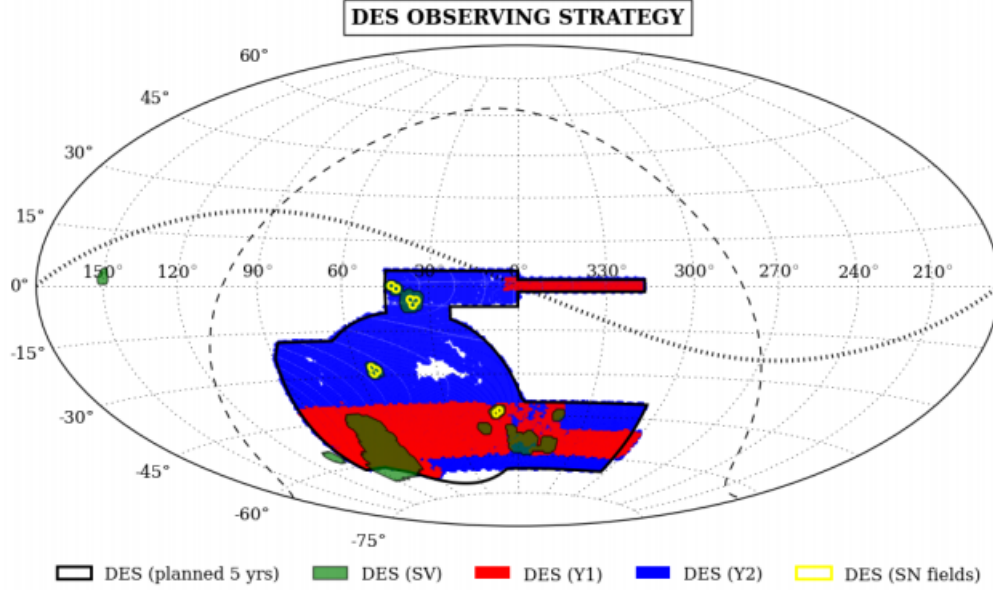
Figure 4.1: DES survey footprint for the science verification (SV), year 1 (Y1), year 2 (Y2) and the final 5-year survey (Dark Energy Survey Collaboration et al., 2016). This is a Hammer projection in equatorial coordinates, with the dashed and dotted lines indicating the Galactic plane and the ecliptic plane, respectively.

in $griz$ and 45 seconds in Y for the main survey. The DES footprint is shown in Figure 4.1. Over the five-year observation, the whole footprint will be imaged 10 times (or 10 tilings) and reach depths of $g = 24.6$, $r = 24.1$, $i = 24.4$, $z = 23.8$, and $Y = 21.3$ mag with 10σ detection for point sources (Rossetto et al., 2011).

In order to accomplish the science goal, high photometry precision is needed to measure photometry redshift and distance to the supernovae. DES collaboration therefore builds two auxiliary systems, namely DECal and aTmCam, to achieve 1% photometry precision or better. In this section, we describe these two systems. In Section 5, we discuss why and how these auxiliary systems can be used for photometry calibrations.

4.2   DECal

The DECam calibration system, DECal, is a spectrophotometric calibration system that is used to measure the relative throughput of the complete optical system (including both the Blanco 4m telescope and the DECam) as a function of both wavelength and position on the focal plane. DECal uses a monochromator to project quasi-monochromatic light ($\sim$2 nm bandwidth) on the flat-field screen at a given wavelength ranging from 320 nm to 1000 nm. DECam takes exposures at every wavelength while four NIST calibrated photodiodes placed around the top ring of the telescope also monitor the amount of light on the screen at the same time. The signal received by the photodiodes is proportional to the intensity of light received by the DECam. The DECam images are then compared with the photodiode output to determine the relative sensitivity of the entire optical system as a function of wavelength for every pixel on the CCDs. Note that the system provides a relative (not absolute) throughput measurement. The full spectrophotometric characterization (a scan for throughput versus wavelength with different filters) is performed several times per year. The data are used to spectrophotometrically calibrate the DES survey data and to monitor the DECam instruments sensitivity as a function of time. More information about the DECal spectrophotometric calibration system can be found in (Rheault et al., 2012) and in a future paper (Marshall et al. in prep).

The DECal system has been used to perform multiple spectrophotometric calibration scans of the DECam system since its commissioning in late 2012. We will also discuss how the products from the scans can be used to calibrate the DES photometry in Section 5. As the DES progresses, the scans taken at different time of the survey will be compared to examine any potential changes in the overall throughput as a function of time.

56

4.3 aTmCam

The Atmospheric Transmission Monitoring Camera (aTmCam) is a calibration system designed to enable the improved photometric calibration of data acquired by the DECam. aTmCam is housed in a new dome on the CTIO summit and consists of a robotic telescope mount, four small telescopes (commercial photographic camera lenses) and four CCD detectors each with a different narrowband filter that monitor the brightness of suitable bright stars throughout the night. Each narrowband filter is selected to monitor a different wavelength region of the Earth's atmospheric transmission such as water vapor and aerosol. The colors of the stars are measured by this multi-narrowband imager system simultaneously. The measured colors, a model of the observed star, and the measured throughput of the system can be used to derive the atmospheric transmission of the site on sub-minute timescales. We deployed a prototype system to CTIO and executed two one-month-long observing campaigns in Oct-Nov 2012 and Sept-Oct 2013 (Li et al., 2014). The final version of aTmCam was deployed and commissioned to the CTIO in the summer of 2014 and it started autonomous observations from August 30, 2014.

4.3.1 Concept

DES has an overall photometric precision goal of $\sim$0.01 mag in the primary survey bands. Although traditional photometric observing techniques – numerous standard star measurements, observations over a large range of airmass, selection of standard stars with a range of colors – can produce photometric precision at these levels, assembling a large survey with such precision is very challenging. For example, the Sloan Digital Sky Survey (SDSS) achieved a relative photometric precision of roughly 1-2% (Padmanabhan et al., 2008). The source of precision error in large surveys is thought to be a combination of various calibration uncertainties. One of

these is related to the exact bandpass and response function of the imaging system (including optics, filters, detectors, etc.). But it is believed that the largest source of photometric precision error is due to variations in atmospheric throughput. For example, Ivezić et al. (2007) found that assuming a standard atmosphere can induce 0.01 mag offsets in some colors due to differences in the real atmosphere during observing relative to the assumed standard. Stubbs et al. (2007) also show that expected changes in the transmission of the atmosphere can produce 1–2% photometric precision errors.

Atmospheric transmission in the optical wavelength is mainly determined by 1) Rayleigh scattering from molecules, 2) aerosol and dust scattering from small particles, and 3) molecular absorption. Figure 4.2 shows a model of fiducial atmospheric transmission at CTIO at airmass X=1.3. Another water-free atmospheric model is also plotted as a contrast to see particularly the absorption from H_20. In Section 5, we discuss in details why the variation of the atmospheric transmission is a non-negligible error budget towards sub-1% photometry precision. As it will be shown in Section 5, we conclude that the variation of these four parameters in atmospheric transmission can affect the photometry precision up to 1%: 1) airmass X of the observation, 2) aerosol optical depth τ, 3) Ångström exponent α, and 4) column density of precipitable water vapor PWV.

The throughput of the atmosphere has been measured by astronomers in great detail using spectroscopic observations. For example, Wallace et al. (2007) gives a high-resolution transmission spectrum of the atmosphere from Kitt Peak National Observatory obtained during the course of observing the Sun. Of course, characterization of the atmosphere is of general interest and is the specific interest of a wide range of scientists. There are, for example, many atmospheric modeling packages available: e.g., MODTRAN (Berk et al., 1998); libRadtran (Mayer & Kylling,
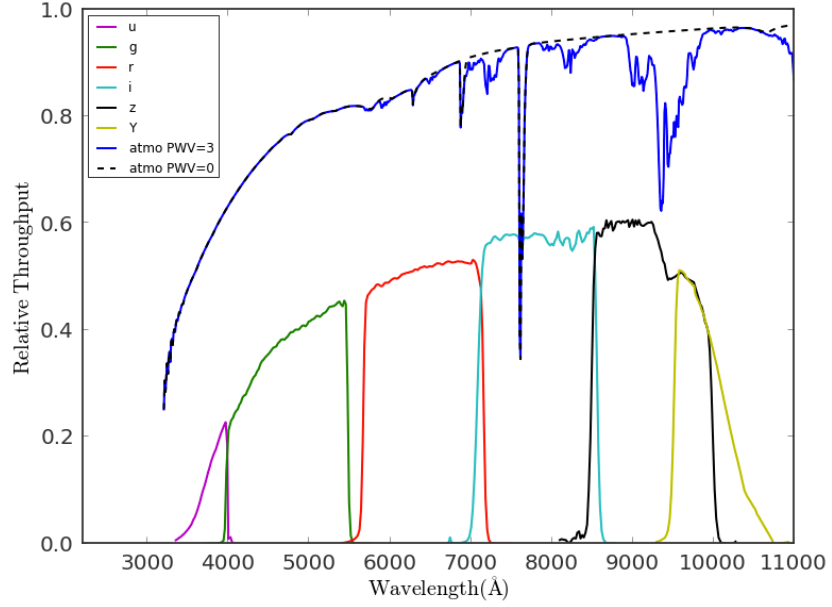
Figure 4.2: DES filter bandpasses ($ugrizY$) and model of atmospheric transimission. A model of fiducial atmospheric transmission at CTIO is shown, with altitude 2.24 km, barometric pressure $P = 780$ mbar, aerosol optical depth $\tau = 0.05$ at 550nm, and precipitable water vapor PWV=3 mm at airmass $X = 1.3$, generated by libRadTran. Another PWV-free atmospheric model is plotted as contrast to see where the absorptions from H20. For reference, the system response function of ugrizY bandpasses currently installed in DECam are shown.

2005); ATRAN (Lord, 1992). These packages are used to aid interpretation aimed at projects such as atmospheric ozone concentration determination, pollution monitoring, solar irradiance measurements, meteorological effects on agriculture, and other areas of interest to the atmospheric science community.

In general, astronomical spectroscopic determination of the atmospheric transmission proceeds by observing a specific set of targets with well-understood spectral energy distributions (SEDs) at various airmasses. In particular, spectroscopic observations of standard stars at $\sim$5 minute cadence, over a range of airmasses, and at wavelengths of $400 < \lambda < 1000$ nm can produce high-quality atmospheric absorption profiles. While this approach is ideal, it has a major drawback in requiring a high level of personnel commitment to aligning a relatively small aperture ($\sim$10 arcsec) on the target stars, a relatively large telescope, and a stable spectrograph.

The philosophy for aTmCam is to use simultaneous measurements of stars with known SEDs through a set of narrow-band filters. The filters are chosen to allow determination of specific features in the atmospheric transmission spectrum, which then can be used to develop a model that accurately represents the throughput of the atmosphere. The system is similar to that suggested by Stubbs et al. (2007). In Li et al. (2012), we demonstrate that brightness measurements of stars at a few wavelengths by narrow-band imager can be used to derive a model for the transmission of the atmosphere that is as precise as what can be derived with spectroscopic measurements.

In the system described below, we used four narrow-band filters with full-width at half maximum of 10 nm. The four filters are centered at 394 nm, 520 nm, 854 nm, and 940 nm, respectively (see Figure 4.3). These wavelengths are chosen to be near a part of the atmospheric transmission spectrum sensitive to a particular component of the atmospheric throughput. We refer to the measured magnitudes from the four
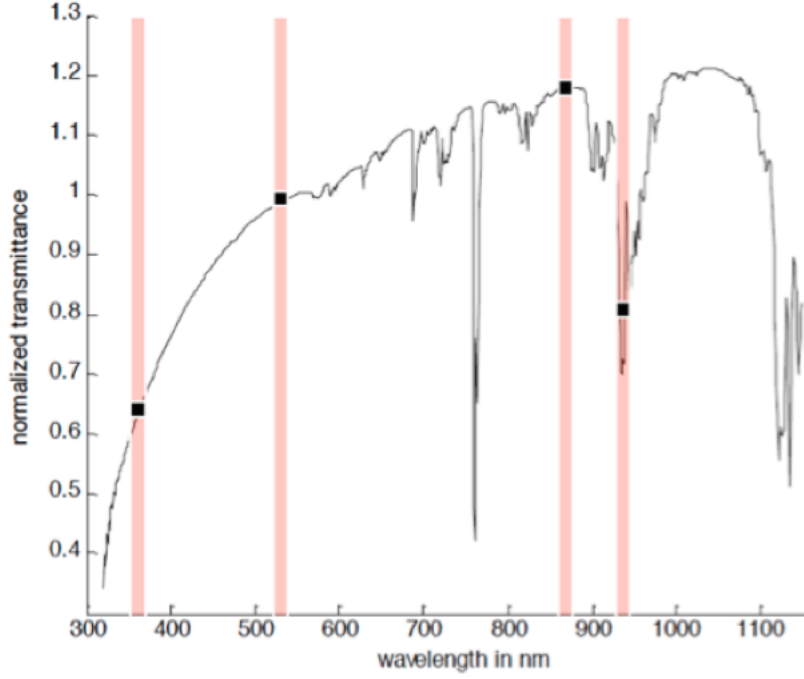
Figure 4.3: The central wavelengths of the four filters overplotted on a fiducial atmospheric model.

narrow bands as m_{380}, m_{520}, m_{854} and m_{940}. We generated a grid of models of the Earths atmospheric transmission using libRadTran. We calculated the synthetic color with those models, the expected throughput of the system and the SED of an A0V star. The synthetic colors are then compared with the observed ones to derive the best fit atmospheric models.

For example, $m_{854} - m_{940}$ color index is most sensitive to PWV but not other atmospheric parameters. We therefore could derive the PWV from $m_{854} - m_{940}$. The left panel of Figure 4.4 plots the synthetic color index $m_{854} - m_{940}$ and airmass X at various PWV. The color is proportional to $X^{0.58}$ and converges at X=0. Using this relationship, we could derive the PWV by measuring the color at a given airmass. Especially, on the nights that the PWV was stable, the slope also allows estimation of the PWV of that night as a consistency check.
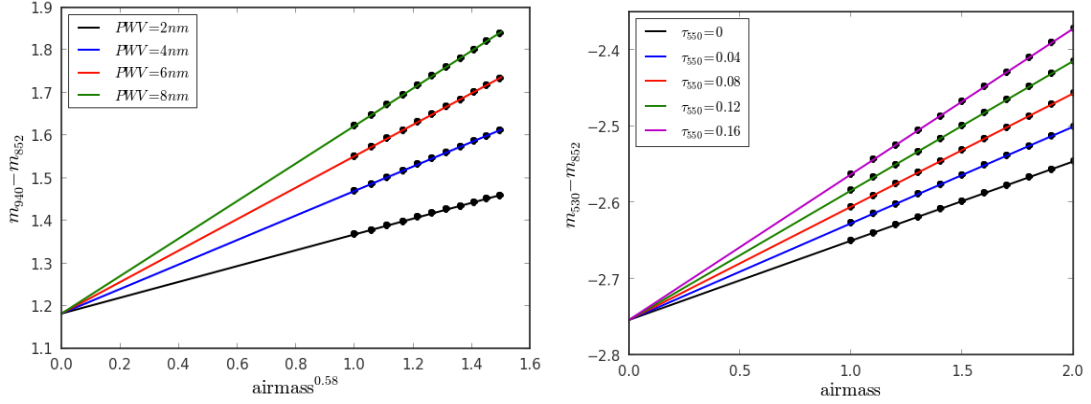
Figure 4.4: Synthetic color indices vs. airmass at various PWV (left) and aerosol optical depth (right).

The aerosol optical depth τ is sensitive the $m_{520} - m_{854}$ color index. A relation between the synthetic color index $m_{520} - m_{854}$ and airmass X at various τ_{550} (aerosol optical depth at 550 nm) is shown in the right panel of Figure 4.4. Note that $m_{520} - m_{854}$ is proportional to X while $m_{854} - m_{940}$ is proportional $X^{0.58}$. This is because m_{940} is centered on a wavelength at which the strength of the H_2O absorption feature is not linear with the H_2O column density.

In the rest of this section, we describe this system, including hardware, software, operation and data reduction.

4.3.2   Description of the System

The aTmCam system payload is composed of four individual Nikon lenses served as telescopes, each attached to an SBIG ST-8300M CCD and a narrow-band filter. The SBIG ST-8300M CCDs have 3326×2504 pixels and each pixel is 5.4 μm $\times$ 5.4 μm. All four telescopes have a same focal length of 300 mm, which results in a plate scale of 3.7" pixel^{-1} and a $3.4° \times 2.5°$ field-of-view. The reddest filter (i.e. central wavelength 940nm) is attached to a f/2.8 camera lens as the CCDs has relative low

quantum efficiency in the wavelength range > 900 nm, while the other three filters are attached to f/4.5 camera lenses.

Each telescope and detector subsystem is powered using its own power adaptor and is connected to a USB hub using a USB 2.0 Standard-A connector wire to Standard-B connector wire for data transfer. Mounting brackets are attached to both the lens and the SBIG ST-8300M CCDs for each of the telescope/detector subsystems. The subsystems are co-aligned to image simultaneously the same position on the sky. These mounting brackets are attached to a mounting plate, which is then attached to a Losmandy dovetail plate. The complete assembly of the telescope, detector, mounting brackets, and dovetail plate constitute the full aTmCam instrument payload which is eventually attached to the Paramount MX+ telescope mount, a commercial German Equatorial Mount.

The complete aTmCam system (see Figure 4.5) is contained inside a 7-foot (2.1m) diameter AstroHaven powered dome which is permanently attached to a concrete pad on the CTIO summit, near the 1m telescope. The dome works by means of two individual electric motor assemblies controlled by a common control panel or by computer through an RS-232 serial port, which we have coupled to a USB interface using a Serial-to-USB converter.

The layout of the data flow and power flow for the whole system is shown in Figure 4.6 and 4.7, respectively. A Mac-Mini computer sits inside the dome and controls the dome, the mount, and four cameras (via a USB hub). Four SBIG Cameras and the Paramount MX+ are connected to an IP Power Switch. The IP Power Switch can be controlled to turn on/off power remotely so that the CCDs and mount will be powered on before the observation starts and be powered off when the observation ends. All the data are saved on an external hard drive and are synchronized to a computer in the computer room of the Blanco 4m dome every day.

Figure 4.5: A photo of aTmCam sitting in the 7-foot AstroHaven dome. Image Credit: Brian Nord.

Apart from the hardware, we have also developed our own control software *OBSAutomation* under the OS X operating system using Apple's native object-oriented application programming interface *Cocoa*. *OBSAutomation* will automatically load a pre-programmed observing script every day. According to the script, it will power up the cameras and the mount before the observing starts and shut down the system after the observing stops. *OBSAutomation* also sends the commands to the equatorial mount for slewing to different targets (via TheSkyX, a proprietary program written by the mount manufacturer) and sends commands to the cameras for taking simultaneous images. The four cameras are read out serially (with about a ~20 s total readout time). The whole system almost runs autonomously. The only hardware interaction with the system from on-site personnel will be to open the
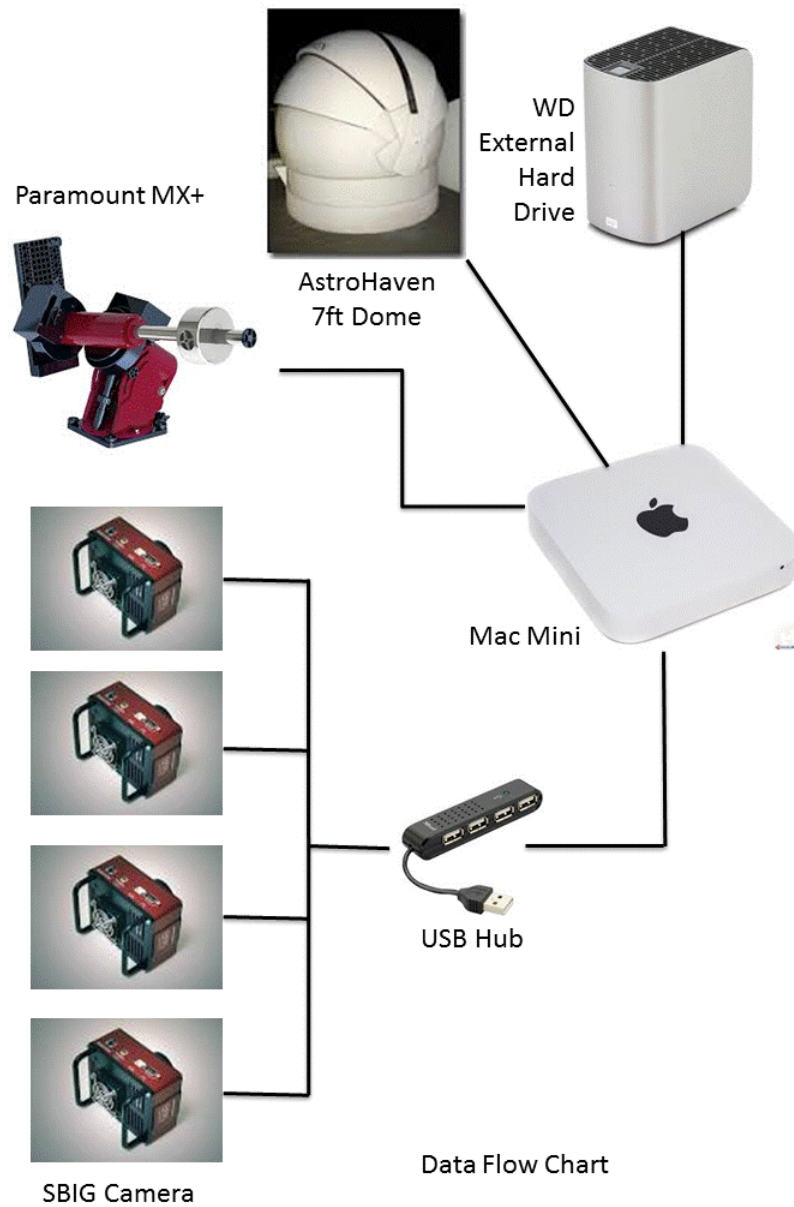
Figure 4.6: Data flow chart for aTmCam. Four SBIG Cameras are connected to the Mac Mini via a USB hub. The Paramount MX+ is connected to the Mac Mini USB port directly. The AstroHaven 7ft Dome is connected to Mac Mini USB port via a RS-232 to USB converter. The WD External Hard Drive is connected to Mac Mini via Thunderbolt directly.
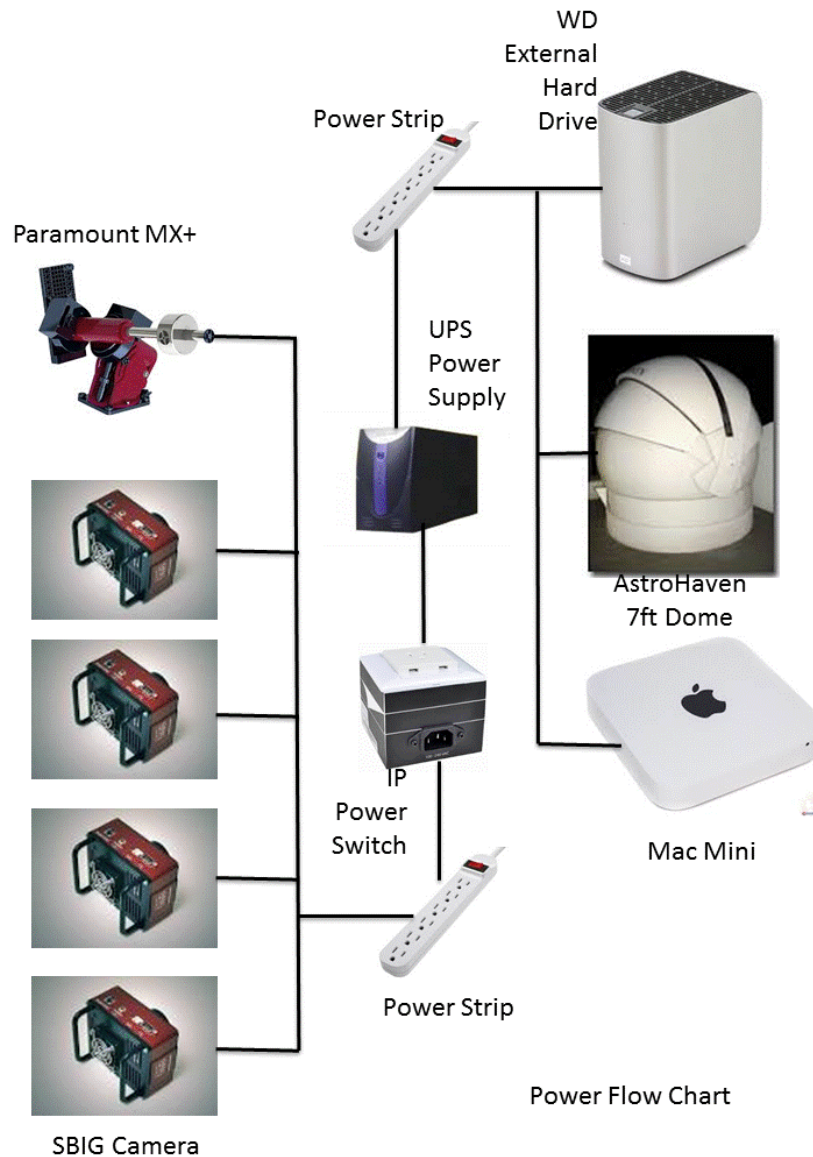
Figure 4.7: Power flow chart for aTmCam. Four SBIG Cameras and the Paramount MX+ are connected to a power strip which is connected to an IP Power Switch then to the UPS power supply. The IP Power Switch can be controlled to turn on and turn off power remotely. The Mac Mini, the dome, and the external hard drive are connected to a second power strip and then connected to the UPS power supply directly. The second power strip is powered on at all times.

dome at the beginning of the night and to close the dome at the end of the night and in the case of bad weather. This is done by the telescope operators at 4m dome remotely, that is, the aTmCam dome is open/closed when 4m dome is open/closed.

4.3.3   Operation

aTmCam is designed to measure the brightness of well-modeled stars at a few wavelengths and then derive a model for Earth's atmospheric transmission for each exposure that matches the best with the observed color index of the star. We selected A0V stars since the SEDs of A0V stars are well understood.

We selected three A0V stars with $V \sim 4.5 - 5$ mag and dec$\sim -30°$ as our main program stars. They are HIP 117452, HIP 42334 and HIP 75501. The RAs of these three stars are about eight hours apart. Therefore, at any given time, one of the three main program stars will be in the sky at airmass < 2. Besides those three main program stars, we also selected about 80 B7V-A1V stars with $3.5 < V < 5.5$ mag and dec $< +30°$ from the Hipparcos catalog (Perryman et al., 1997).

Every night, the mount and the four CCDs are powered up 30 minutes after sunset and start the observations. The exposure time was set to equal across four bands but varies from target-to-target to avoid saturation and obtain adequate S/N, with an average exposure time of 30 s on a $V \sim 4.5$ mag star. With additional 20 s readout time, aTmCam get about one exposure per minute. The observation will be conducted according to the preloaded script for that night, and the strategy is described as follow:

1) After the mount and CCDs are powered on, CCDs will first start electronic cooling at $-10°C$, and the mount will slew to one of the three main program stars which has the smallest airmass. This slew process usually takes 5-30 seconds to finish, depending on the location of the target.

2) One minute after last slew motion is triggered, the four CCDs start to taking exposures on the main program star. It will take sequence exposures for 19 minutes.

3) 20 minutes after last slew motion is triggered, the mount will slew to one of the 80 B7V-A1V stars that are above the horizon (airmass < 3).

4) One minute after last slew motion was triggered, the four CCDs will take sequence exposures for 9 minutes.

5) 10 minutes after the last slew motion is triggered, the system will go back to the main program stars and repeat the whole process.

Therefore, the system will spend 20 minutes on a main program star and then 10 minutes on another program star randomly picked. This 20-10-20-10 process is repeated until 30 minutes before sunrise. The mount is then sent to park position and the whole system is powered off.

Every night, aTmCam can cover about 66% of the total observing time on the main program stars to derive water vapor and aerosol. Moreover, it can observe 15–20 other program stars at a different part of the sky to study the spatial variation in the future.

In the case of the bad weather, the telescope operators for the Blanco Telescope will remotely close the aTmCam dome, but the system will run in the same way no matter whether the dome is open or close.

4.3.4   Data Reduction

aTmCam obtains about 600 images per filter per night in a total size of ∼40 GB data. The data reduction process is also fully automated. Every morning at 8:00 am Chilean local time, the images taken from the previous night will be transferred to a computer inside the computer room in the 4m dome. At 10:00 am Chilean local time, the reduction pipeline will automatically start the process the data from the

previous night.

All the data are first bias subtracted and flatted using sky-flats taken at the beginning of every DES season. The brightest star in each image is usually the program star. The instrumental magnitude of the brightest star in each image is measured using SExtractor. The measured value is then compared with a grid of atmospheric transmission models to derive the parameters, including PWV and aerosol optical depth. A summary of the nightly results is updated to http://instrumentation.tamu.edu/~ting/atmcam_summary/ around noon Chilean local time.

5. ASSESSMENT OF SYSTEMATIC CHROMATIC ERRORS THAT IMPACT SUB–1% PHOTOMETRIC PRECISION IN LARGE-AREA SKY SURVEYS[*]

5.1 Introduction

In traditional astronomical photometry, a set of standard stars, such as those from Landolt's (Landolt, 1992) or Stetson's (Stetson, 2000, 2005) catalogs, is observed over a wide range of airmasses during the course of a night to calibrate all sources observed on the same night. The observed instrumental magnitude m_b and the standard magnitude m_b^0 for a given bandpass b have the following relation,

$$m_b - m_b^0 = a_b + k_b \cdot X + c_b \cdot color \tag{5.1}$$

where a_b is the photometric zeropoint, k_b is the first order atmospheric extinction coefficient, X is the airmass for each exposure, c_b is the color term coefficient, and *color* is the color of the stars (e.g. $g - r$ or $V - R$, depending on the photometric systems and the filter bandpasses). On a photometric night – i.e., a night in which the atmospheric extinction coefficient is stable over time and uniform over the sky – the nightly a_b and k_b are derived. The color term c_b is a first-order correction to compensate for the difference in the *shape* of the filter bandpass of the standard system and that of the filter bandpass actually used in the night's observations. This term corrects for the full system response for that filter bandpass, including both the instrument throughput and the atmospheric transmission. Fortunately, for most optical passbands, the color term coefficients are reasonably constant over the

course of a typical observing run ($<$1 week), and by fitting the above relation to observations of standard stars and applying the results to the science exposures, all the program target objects can be calibrated to a standard photometric system with reasonable precision.

We note that tying data to a standard system serves two aspects of photometric calibration: *relative* calibration and *absolute* calibration. Relative calibration refers to creating a data set whose photometry is internally consistent: e.g., the measured brightness and color of a (non-variable) star is, all else being equal, independent of its time of observation or its location on the sky. Absolute calibration refers to creating a data set whose photometry can be tied to physical units of specific flux (see e.g. Scolnic et al., 2015, for a review). By tying data to a standard system, one ensures that the data are consistent with the standard photometric system and can connect the apparent brightnesses and colors of stars in one's own data to those of stars that have calibrated magnitudes that are convertible to units of specific flux in ergs s^{-1} cm^{-2} Hz^{-1} (Holberg & Bergeron, 2006).

In recent years, large imaging surveys like the Sloan Digital Sky Survey (SDSS) have opted to create their own standard photometric systems – ones based on the "natural" photometric system of their instruments[1] – rather than try to transform their immense quantities of data to a previously defined standard system, like the Johnson-Cousins $UBVR_cIc$ system (Bessell, 1990). A practical advantage of this is that it effectively decouples the photometric calibration of data taken in one filter with data taken in another filter: in other words, one need not match data from one filter to data in another filter in order to apply a color term, and this works

---

[1]A natural system is one in which the color term coefficients c_b are all identically zero. Since system responses can and do change with time or even spatially across a survey instrument's field-of-view, surveys tend to *define* their natural systems by their instrument's mean system response, thus ensuring any color terms are very small and average to zero.

sufficiently well for calibrating large optical imaging surveys at the $\sim$2% (0.02 mag) level.

With the success of these earlier surveys, photometric calibration has become an important factor in the systematic error budgets in the era of precision cosmology. Therefore, many current and future ground-based wide-field imaging surveys have the ambitious calibration goal of "breaking the 1% barrier", which requires that calibrated broadband photometry is both stable in time and uniform over the sky to $< 1\%$ (0.01 mag or 10 millimag) rms precision. These sub–1% precision requirements are driven by the specific science needs of photometric redshift accuracy, the separation of stellar populations, detection of low-amplitude variable objects, and the search for systematic effects in Type Ia supernova light curves (see more details at e.g., the Large Synoptic Survey Telescope Science Book, LSST Science Collaboration et al., 2009).

Traditionally, photometry with $\sim$1% level precision is reachable when careful analysis is taken on the flat fielding, such as star flats (Manfroid, 1995), across a small field-of-view (FOV), and when observations are done under photometric conditions, i.e. atmospheric conditions are stable and free of clouds. Thanks to the continuous and rapid observing cadence of these dedicated surveys, overlapping areas with multi-epoch observations can be used to calibrate the illumination pattern of the imaging system with a large FOV. Indeed, Padmanabhan et al. (2008) applied the "Ubercal" procedure to the SDSS data taken in good photometric conditions and reached rms of 1-2% relative photometry. Many other sky surveys, such as Pan-STARRS (Schlafly et al., 2012) and Deep Lens Survey (Wittman et al., 2012) have also adopted this calibration procedure for their photometric calibrations.

In order to maximize survey efficiency, imaging surveys might also be conducted in less than ideal conditions, i.e. cloudy or partly cloudy nights. Again, owing

to the overlapping area in multi-epoch observations, the repeated measurements of a large number of stars allow an internal global calibration of the frame-to-frame zeropoint offset (Glazebrook et al., 1994), which links the instrumental magnitude and natural magnitude of the survey. This zeropoint offset can be a combination of the instrumental zeropoint change, the atmospheric extinction at a given airmass, and cloud extinction. One zeropoint offset is computed and applied to each exposure or each CCD detector, depending on the airmass of the exposure as well as photometric condition. For example, when the airmass is small and the night is photometric, the zeropoint offset could be computed on an exposure-by-exposure level; when the airmass is large or the night is cloudy, then the zeropoint offset could be computed on a CCD-by-CCD level. MacDonald et al. (2004) used this technique on the global calibration of Oxford-Dartmouth Thirty Degree Survey.

The Dark Energy Survey (DES) is a wide-area photometric survey of 5,000 square degrees using the Dark Energy Camera (DECam) at the Cerro Tololo Inter-American Observatory (CTIO) 4m Blanco telescope. DECam is composed of 74 $250\mu m$ thick fully-depleted CCDs – 62 for science imaging, plus 12 CCDs for real-time guiding and focus – with a FOV of 2.2° (3.1 deg^2 in area) and a pixel scale of 0.26 arcsec/pixel. The filters are 620 mm in diameter and fully cover the 62 science CCDs. For further details on DECam itself, see Flaugher et al. (2015). DES has a requirement for relative photometric calibrations: the survey calibrations must be internally consistent both spatially over the survey footprint and temporally over the 5 years of the survey to at least 2% with a goal of 1% or better. However, one of its four main probes of cosmological parameters – the Hubble Diagram of Type Ia supernovae – requires photometric precision better than 1% for the 10 supernova fields. To achieve these relative calibration requirements, DES uses a combination of calibration methods mentioned above. First, star flats are obtained at the beginning of each DES season

73

and during engineering nights in order to obtain robust pupil ghost and illumination corrections for the flat-fielding exposures (G. Bernstein et al., in prep.). Second, over its 5-year run, DES will cover its full footprint 10 times (in 10 "tilings") in each of its 5 filters (DES-$grizY^2$), and it uses the large overlaps between exposures in different tilings to tie together the relative calibrations globally across the full survey footprint. Meanwhile, a sparse grid-work of stars extracted from the multiple DES tilings and calibrated via nightly DES standard star solutions serves both to "anchor" the relative calibrations against large-scale (but low-amplitude) systematic gradients that are often inherent to Ubercal techniques and to tie the relative calibrations to an absolute flux calibration (Tucker et al. 2007; Tucker et al., in prep.).

However, most of the calibration techniques discussed above consider only the relative frame-by-frame zeropoint offset and position dependent illumination corrections, which are independent of the source color, i.e. grey-scale zeropoint corrections, or grey-term. In reality, variations in the wavelength dependence of the system response (i.e. atmospheric transmission + instrumental throughput) can also induce changes in measuring the brightness of an object that depend on the spectral energy distributions (SEDs) of the object. We refer to such changes as systematic chromatic errors, or SCE, throughout this dissertation. We use the word "chromatic", since this effect could be considered as approximately linear to stellar colors, which is similar to a linear color-term correction (e.g. c_b in Equation 5.1) used to transform from one photometric system to another. It is essentially the change of the *shape* of the system response. At 1% level photometric precision, SCE are significant components of the total photoemtric error budget when calibration techniques only include grey-scale

---

[2]DECam has seven filters. They are DECam-u, DES-g, DES-r, DES-i, DES-z, DES-Y, and DECam-VR. DES has no u-band component in its primary survey. However, we include discussion of DECam-u here since it is available for all DECam community users. For simplicity, we will refer to the six bands as $ugrizY$.

zeropoint corrections. In a few previous imaging surveys, SCE have been partially considered. For example, Ivezić et al. (2007) applied color-term corrections for different transmission curves from six camera columns when making the SDSS standard star catalog for Stripe 82. The Supernova Legacy Survey (SNLS) built a photometric response map to correct the non-negligible color-term variations between photometric measurements obtained at different focal plane positions of the wide field imager MegaCam (Regnault et al., 2009). Betoule et al. (2013) also considered such color-term variations in a combined photometric calibration of the SNLS and the SDSS supernova survey. Most past surveys, however, did not include corrections for SCE in their photometric calibration, especially the SCE from the atmospheric variation, as these corrections are small and hard to determine using the data alone. In this dissertation, we calculate the SCE and show that these errors are caused by not only the non-uniformity of system response function over the focal plane, but also the change of airmass in each exposure and the change of the precipitable water vapor and aerosol in the atmosphere over time. We also demonstrate that our calculations match what we observe in the DES data.

We structure this section as follows: In Section 5.2, we discuss possible variations in the system response and define a fiducial system response for the DES natural system. In Section 5.3, we calculate the synthetic SCE for stellar objects when the system response deviates from a fiducial system response. In Section 5.4, we compare these synthetic SCE with actual DES data and show the SCE could be corrected using the synthetic SCE when the actual atmospheric transmission and instrumental throughput are measured directly. We then calculate the synthetic SCE for non-stellar objects, e.g. SNe Ia and galaxies, at different redshifts in Section 5.5. Section 5.6 has a discussion of our results and presents our conclusions.

5.2 Variation in the System Response

Given a specific flux of an object at the top of the atmosphere, $F_\nu(\lambda)$, the total ADU counts F that are measured by a camera with a photon detector (e.g., Charge Coupled Device, or CCD) can be calculated as:

$$F = C \int_0^\infty F_\nu(\lambda) S_b(\lambda) \lambda^{-1} d\lambda \tag{5.2}$$

Here $S_b(\lambda)$ is the system response function for a given bandpass b. The system response includes the Earth's atmospheric transmission along the line-of-sight, the reflectivity of the mirrors on the telescope, the transmission of the camera lenses and filters, and the quantum efficiency of the detector. C is a constant and related to the effective collecting area of the primary mirror A, the inverse gain of the CCD g ($electron/ADU$) and the exposure time Δt:

$$C \propto \frac{A \Delta t}{g} \tag{5.3}$$

The constant C is not strictly necessary for the calibration, as the observations of spectrophotometric standards (such as DA white dwarfs) using the same instrument can tie a specific natural system onto an AB magnitude system without knowing the actual value of C (see e.g. Holberg & Bergeron, 2006).

Stubbs & Tonry (2006) proposed that the process of photometric calibration can be separated into the measurement of the atmospheric transmission and a measurement of the instrumental throughput, so that the system response could be separated as

$$S_b(\lambda) = S^{atm}(\lambda) \times S_b^{inst}(\lambda) \tag{5.4}$$

The atmospheric transmission $S^{atm}(\lambda, alt, az, t)$ could change over time and could also depend on the position of the object in the sky (alt, az). It may vary in both a grey-scale (wavelength-independent) and a non grey-scale (wavelength-dependent or the *shape* of the transmission curve) manner. Studies have shown that the atmosphere, especially the precipitable water vapor, is homogeneous across the sky (Querel & Kerber, 2014; Li et al., 2014); we therefore do not discuss the spatial variation of atmospheric conditions in the rest of the paper.

The instrumental throughput $S_b^{inst}(\lambda, x, y, t)$ is similar, except that it may vary over time as well as over the position (x, y) on the detector focal plane. Again, the throughput can also vary in both a grey-scale and a non grey-scale manner. It is therefore convenient to separate the system response into a wavelength-independent normalization factor N and a wavelength-dependent *shape* factor $\phi(\lambda)$ for each bandpass b:

$$S_b(\lambda) = N_{atm} \times \phi^{atm}(\lambda) \times N_{inst}^b \times \phi_b^{inst}(\lambda) \tag{5.5}$$

Equation 5.2 then can be rewritten as

$$F = C \times N_{atm} \times N_{inst}^b \int_0^\infty F_\nu(\lambda)\phi^{atm}(\lambda)\phi_b^{inst}(\lambda)\lambda^{-1}d\lambda \tag{5.6}$$

Over a wide area imaging survey that might be conducted for months or years, both N and $\phi(\lambda)$ could be slightly different from one exposure to another, or even within one exposure. For example, airmass extinction and clouds affect N_{atm}; dust on the mirror affects N_{inst}. As described in Section 1, multiple tilings of the survey area, with the repeated measurements of a large number of stars, allow the monitoring of the zeropoint offsets over time and the illumination correction over the focal plane. This paper will not discuss the calibration for the grey-scale variation, i.e. variation

77

of N, as the grey-scale correction procedure mentioned in Section 5.1 is adequate to calibrate those variations. In this paper we will focus on the variation of the *shape* of the system response (i.e. atmospheric transmission + instrumental throughput), $\phi_b(\lambda) = \phi^{atm}(\lambda, t) \times \phi_b^{inst}(\lambda, x, y, t)$. The variation of ϕ_b will essentially induce the SCE.

5.2.1 Variation in the Atmospheric Transmission ϕ^{atm}

Atmospheric transmission in the wavelength range covered by DES (300nm–1100nm) is mainly determined by the following four processes in the Earth's atmosphere (Stubbs et al., 2007): Rayleigh scattering from molecules, aerosol scattering from small particles, molecular absorption, in particular by O_2, O_3, and H_2O, and cloud extinction. The size of water droplets and ice crystals that make up clouds are larger than the wavelength of visible light, and the attenuation by clouds is wavelength independent (Ivezić et al., 2007; Burke et al., 2014; Li et al., 2014). Cloud extinction is therefore calibrated with gray-scale corrections so we do not consider it in this paper.

The cross sections of Rayleigh scattering and aerosol scattering both vary smoothly with the wavelength of the incident light. The optical depth of Rayleigh scattering has a wavelength dependence of λ^{-4} (Rayleigh, 1899). At zenith, it can be simply scaled with the barometric pressure P_0 (Hansen & Travis, 1974).

The optical depth of aerosol scattering at zenith could be approximately described by the Ångström formula (Ångström, 1924):

$$\tau_{aerosol} = \tau_0 (\frac{\lambda}{\lambda_0})^{-\alpha} \tag{5.7}$$

where τ_0 is the aerosol optical depth at reference wavelength λ_0, where $\lambda_0 = 550$ nm is a convenient reference wavelength. The Ångström exponent α is inversely related

to the average size of the particles in the aerosol: the smaller the particles, the larger the exponent. In general, α ranges from 0 to 3 with typical values around 1 to 1.3, depending on the geographic location. $\alpha < 1$ indicates size distributions dominated by coarse mode aerosol that are usually associated with dust and sea salt, and $\alpha > 2$ indicates size distributions dominated by fine mode aerosols that are usually associated with urban pollution and biomass burning (Schuster et al., 2006). $\alpha = 0$ and $\alpha = 4$ are essentially the two extreme cases of cloud extinction and Rayleigh scattering.

Absorption by molecules only occurs at specific wavelengths. The strong absorption lines by O_2 at 690 nm and 760 nm (Fraunhofer "B" and "A" bands) are saturated and are closely proportional to the square root of the barometric pressure, so they can be computed and scaled with Rayleigh scattering (Burke et al., 2010). O_3 absorption mainly affects atmospheric transmission shortwards of 350 nm and in the Chappuis band (450–700 nm). The optical depth of ozone scales with the ozone column density. Ozone column density is usually measured in Dobson units (DU). Each Dobson unit is equivalent to a thickness of 0.01 mm of ozone at standard temperature and pressure. H_2O absorption mainly influences the atmospheric transmission at wavelengths longer than 600 nm. The optical depth can be scaled with the precipitable water vapor (PWV) column density in mm.

Both the optical depth and the column density mentioned correspond to the vertical path from the observer's location to the top of Earth's atmosphere. For a given atmospheric condition, the atmospheric transmission T of the light also depends on the airmass of the observation. For molecular and aerosol scattering, the transmission T at airmass $X = 1$ and at airmass $X = n$ has the simple relation:

$$T(\lambda, X = n) = T^n(\lambda, X = 1) \tag{5.8}$$

The transmission due to molecular absorption, however, has a nonlinear curve of growth with respect to the optical depth or the airmass because the absorption departs from the optically thin limit.

We conclude here that the following six parameters determine a specific *shape* of the atmospheric transmission $\phi^{atm}(\lambda)$: 1) airmass X of the observation, 2) barometric pressure P_0 , 3) aerosol optical depth at 550nm AOD_{550}, 4) Ångström exponent α, 5) ozone column density $Ozone$, and 6) precipitable water vapor column density PWV. We define the six parameters for a fiducial atmospheric transmission curve at CTIO using $X = 1.2$, $P_0 = 779$ hpa (1hpa = 100 pascal), Ozone column density = 270 DU, $PWV = 3$ mm, $AOD_{550} = 0.02$, and $\alpha = 1$, which are also listed in Table 5.1. We choose an airmass of 1.2 as one that is typical of observations in DES wide-field survey. Meteorology data from CTIO show that the average barometric pressure during the year 2014 was 779hpa with standard deviation of 3hpa. Ozone column density at CTIO ranged from 240 DU to 300 DU with a mean of roughly 270 DU in 2014 according to the NASA Ozone Mapping and Profiler Suite (OMPS) Nadir Mapper.[3] CTIO does not have instrumentation to examine PWV, AOD and α. DES therefore deployed the Atmospheric Transmission Monitoring Camera (aTmCam, Li et al., 2012, 2014) in the summer of 2014, preceded by prototype tests in Oct-Nov 2012 and Sep-Oct 2013, to study the water vapor and aerosol at CTIO. aTmCam is a robotic multi-band imaging system. During DES observations, aTmCam takes simultaneous images in four narrow ($\sim$10 nm) bands centered at 394 nm 520 nm, 854 nm and 940 nm. The aTmCam analysis derives the parameters of the atmospheric transmission models at CTIO including PWV and AOD.[4] $PWV = 3$ mm and $AOD_{550} = 0.02$ were the average values at CTIO from those early results. The

---

[3]http://ozoneaq.gsfc.nasa.gov/tools/ozonemap/

[4]For more information, please see the cited papers or visit http://instrumentation.tamu.edu/aTmCam.html

long-term variation range of PWV and AOD at CTIO is not yet clear, but preliminary aTmCam results indicate that that PWV varies between 0–20 mm and AOD varies between 0–0.2. Using the aforementioned parameters, we generated the fiducial atmospheric transmission $\phi_{ref}^{atm}(\lambda)$ using $libRadTran^5$ (Mayer & Kylling, 2005), as shown in Figure 1.

5.2.2   Variation in the Instrumental Throughput ϕ_b^{inst}

Instrumental throughput is a combination of the mirror reflectivity, lens transmission, filter transmission, and detector sensitivity. The *shape* of the throughput may vary over time as the detector temperature changes or the filter coatings age. It may also have a spatial dependent variation over the focal plane. Furthermore, each CCD has its own response function. DES has deployed a spectrophotometric calibration system (DECal) that scans the instrument response for all bandpasses by measuring the relative instrumental throughput as a function of wavelength (Rheault et al., 2012). DECal is used to scan the wavelength range of each filter several times a year, typically during cloudy nights, to monitor the instrumental throughput over time. DECal measurements indicate that the filter bandpass edges vary with focal plane position, primarily with radial position and in $i-$band in particular. This effect is largely due to slightly inhomogeneous filter transmission with incident angle. Here, we define the fiducial instrumental throughput $\phi_{ref}^{inst}(\lambda)$ from the results of DECal scans obtained during Sep-Nov 2013. We use the average throughput over the entire focal plane as the fiducial instrumental throughput, which is also shown in Figure 5.1.

---

[5]libRadTran is a collection of C and Fortran functions and programs for calculation of solar and thermal radiation in the Earth's atmosphere, see more details at http://www.libradtran.org/
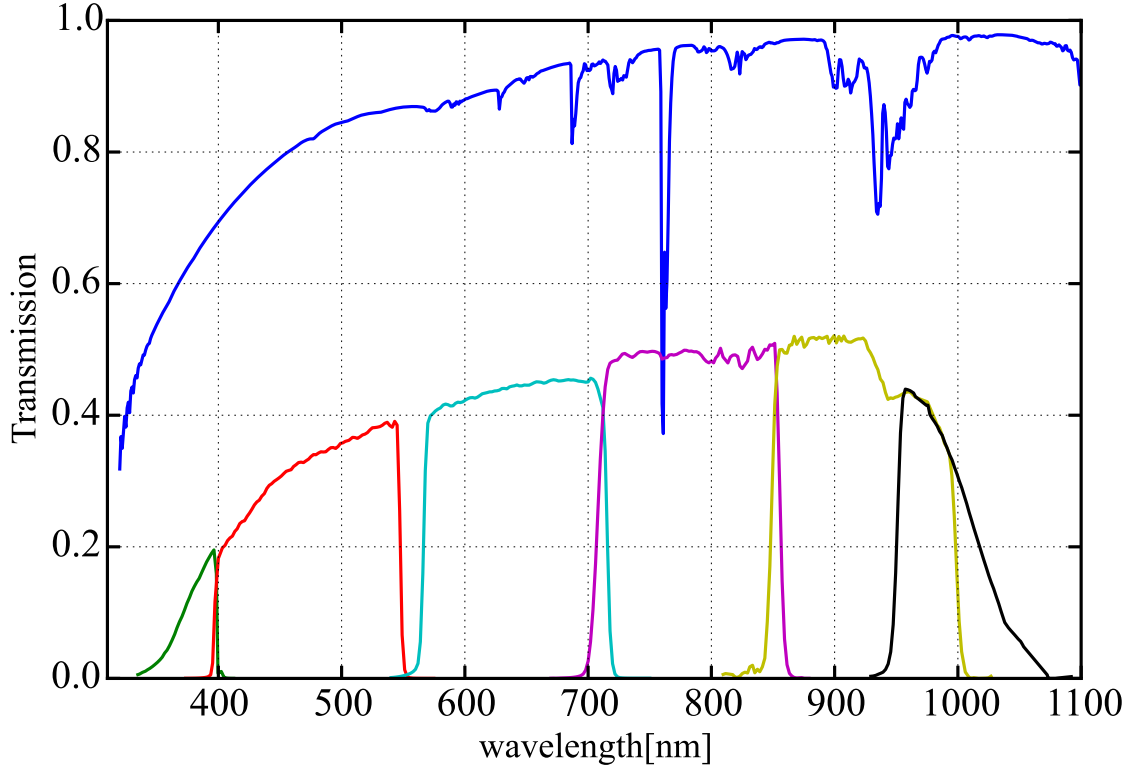
Figure 5.1: The fiducial atmospheric transmission $\phi_{ref}^{atm}(\lambda)$ at CTIO (upper curve) and the fiducial instrumental throughput $\phi_{b,ref}^{inst}(\lambda)$ of the DES-*ugrizY* filter band-passes (lower curves). As DECal only provides a relative throughput measurement, the scale of the lower curves is arbitrary to provide a better visualization.

5.3 Synthetic Systematic Chromatic Errors

In this section, we calculate the synthetic SCE when the atmospheric transmission $\phi^{atm}(\lambda)$ and the instrumental throughput $\phi^{inst}(\lambda)$ deviate from the fiducial values defined in Section 2. We define the synthetic SCE, Δm, as:

$$
\Delta m = -2.5 \log_{10} \frac{\int_0^\infty F_\nu(\lambda)\phi^{atm}(\lambda)\phi_b^{inst}(\lambda)\lambda^{-1}d\lambda}{\int_0^\infty F_\nu(\lambda)\phi_{ref}^{atm}(\lambda)\phi_{b,ref}^{inst}(\lambda)\lambda^{-1}d\lambda}
$$
$$
+ 2.5 \log_{10} \frac{\int_0^\infty F_\nu^{ref}(\lambda)\phi^{atm}(\lambda)\phi_b^{inst}(\lambda)\lambda^{-1}d\lambda}{\int_0^\infty F_\nu^{ref}(\lambda)\phi_{ref}^{atm}(\lambda)\phi_{b,ref}^{inst}(\lambda)\lambda^{-1}d\lambda} \quad (5.9)
$$

The first term is the change in magnitude for an object with SED $F_\nu(\lambda)$ when ϕ^{atm} and/or ϕ_b^{inst} deviate from fidicual values. We use the SEDs of Main-Sequence stars O5V-M6V from the Pickles Atlas (Pickles 1992) as $F_\nu(\lambda)$ for this calculation. The second term is the change in magnitude for a reference star. $\Delta m = 0$ when the SED of the object is the same as the reference star. This reference star plays a similar role that calibration stars play in the zeropoint computation from the global calibration or the illumination correction in the calibration procedure of DES. The only difference is that the actual survey calibration stars have a range of colors, and the grey-term correction is derived for the average color of the calibration stars. We pick a solar-type (G2V; $g - i \sim 0.6$) star as the reference star, i.e. a G2V star will have zero Δm due to the change of atmospheric transmission and/or instrumental throughput.

5.3.1 Synthetic SCE due to the Variation in Atmospheric Transmission

We first generate a grid of atmospheric transmission curves for a range of airmass, barometric pressure, AOD, α, PWV and Ozone using *libRadTran*. We then com-

pute SCE due to the variation in atmospheric transmission using Equation 5.9 by varying one atmospheric component at a time but keeping the fiducial instrumental throughput unchanged.

We calculate Δm when the airmass changes from $X = 1.2$ to $X = 1.8$. Figure 5.2 shows the ratio of atmospheric transmission at two different airmasses and Δm for O5V-M6V stars introduced by this airmass change, as a function of $g - i$ color. Δm due to the airmass change is more than ± 10mmag in g-band for O stars and M stars, and a few mmag in u- and r-band. Δm in i-, z- and Y-band is small. The SCE due to the airmass change are essentially the "second-order extinction coefficient" or "airmass color extinction coefficient", which is known to increase towards bluer wavelengths (Henden & Kaitchuck, 1990).

We run a similar calculation for the change in PWV from $PWV = 3$ mm to $PWV = 10$ mm and show the results in Figure 5.3. Δm due to the PWV change is mainly in the z- and Y-band. The errors can be as large as $+10$ mmag in z-band and -4 mmag in Y-band and thus an error of > 10 mmag in $z - Y$ color. As mentioned earlier, molecular absorption does not vary linearly with column density, and therefore Δm caused by a PWV change from $PWV = 3$ mm to $PWV = 10$ mm is about the same as that from $PWV = 0$ to $PWV = 3$ mm or from $PWV = 10$ mm to $PWV = 20$ mm.

We also perform a similar calculation for Δm when barometric pressure, aerosol and ozone change in the atmosphere. We list Δm in Table 5.1 for an M6V star ($g - i \sim 4$) as a summary for all above cases, after the grey-term has been removed using a G2V star. Δm caused by a change of the barometric pressure is very small. An extreme case of the barometric pressure change from 779 hpa to 789 hpa results in photometric errors of no more than 0.5 mmag in any band.

Δm caused by ozone variation is also small; an ozone change from 270 DU to 230

DU, which is an extreme case of the smallest ozone column density measured by the OMPS Nadir Mapper at the longitude and latitude of CTIO, results in $\Delta m < 1$ mmag in any band, and of only a few tenths of mmag in g- and r-band due to the Chappuis band. The DECam optics essentially has no throughput below 350 nm, so the ozone variation impact on u-band photometry is also negligible. This might not be the case for other cameras with greater response below 350 nm.

The change in aerosol optical depth affects mostly g- and r-band. As shown in Table 5.1, increasing AOD_{550} from 0.02 to 0.20 and keeping α unchanged results in $\Delta m = -11$ mmag in g-band. If the increase of the aerosol optical depth is due to the larger size of the aerosol particles, then α would decrease and Δm would be smaller compared to the unchanged α case. Equation 5.7 shows that an increase of AOD makes the atmospheric transmission spectrum redder and a decrease of α makes the transmission spectrum bluer. Therefore, larger particle size (i.e. smaller α) with larger AOD might introduce very small Δm in one or more bands. AOD and α are somewhat degenerate for the *shape* of the atmospheric transmission.

The synthetic SCE in Table 5.1 are calculated when one of the atmospheric components changes from the fiducial while the other components remain unchanged. Under some conditions, the SCE can be significantly larger. For example, Δm for a PWV change from 3 mm to 10 mm will be much larger than 10 mmag if the airmass is at $X = 2.0$ instead of the fiducial $X = 1.2$. Of course, cumulative effects can also be larger.

In this section, we calculated the synthetic SCE on stellar photometry caused by the variation in the atmospheric transmission. The SCE caused by the variations in barometric pressure and ozone are very small. Variations in airmass and aerosol mainly affect the DES photometry in the ugr-bands; variations in PWV mainly affect the DES photometry in the zY-bands, as shown in Table 5.1. This is the primary

Table 5.1: Synthetic SCE on a M6V Star ($g - i \sim 4$) with respect to a G2V Star ($g - i \sim 0.6$).

Component	Fiducial	Changed[a]	Synthetic SCE (mmag)					
			u	g	r	i	z	Y
Pressure	$P_0 = 779$ hpa	$P_0 = 789$ hpa	−0.2	−0.4	−0.08	−0.06	0.04	−0.02
Aerosol	AOD= 0.02, $\alpha = 1$	AOD= 0.20, $\alpha = 1$	−3	−11	−6	−4	−1	−0.2
	AOD= 0.02, $\alpha = 1$	AOD= 0.20, $\alpha = 0.5$	−41	−5	−3	−2	−0.8	−0.1
PWV	PWV = 3 mm	PWV = 10 mm	0	0	3	−0.6	+10	−3
Ozone	Ozone = 270 DU	Ozone = 230 DU	0	−0.7	0.9	0.1	0	0
Airmass	$X = 1.2$	$X = 1.8$	−9	−13	−6	−2	+2	−0.8
Instrument	DECal scan	shift 2 nm	−24	−15	−16	−19	−10	−5

[a]The "changed" conditions here are just examples. For pressure and ozone, we used the extreme examples since the SCE are small; for aerosol, PWV and airmass, we give the examples where the change could introduce about 1% or 10 mmag SCE. For the instrument, we choose 2nm shift as it's about the average value from the DECal scans.

reason that DES built and deployed aTmCam: to measure the PWV and aerosol at CTIO during DES operations. Furthermore, in order to provide a cross-check of the amount of PWV measured by aTmCam, DES has also installed a high-precision dual-band Global Positioning System (GPS). The GPS is used to measure the PWV, as the variation of PWV affects arrival time of the GPS signal via the increased index of refraction (Blake & Shaw, 2011). The measured PWV by aTmCam and GPS agrees within the joint uncertainties of the two measurements. More details about a direct comparison can be found in (Li et al., 2014).

5.3.2 Synthetic SCE due to the Variation in Instrumental Throughput

In this section, we study the synthetic SCE, Δm, due to the variation in the instrumental throughput. For reference, SDSS discovered variations of the instrumental throughput over its survey period (Doi et al., 2010). Such variations could introduce SCE similar to those caused by the variation in the atmospheric transmission. DES so far has not seen a variation in instrumental throughput over time from the DECal scans in the past three years; however, data from DECal have shown a shift of either the blue or red edges of the filter bandpasses over the focal plane.

We shift the fiducial instrumental throughput $\phi_{ref}^{inst}(\lambda)$ 2 nm towards the longer

Figure 5.2: Synthetic SCE caused by an airmass change. Top panel: The ratio of the atmospheric transmission for two airmass values, $X = 1.2$ and $X = 1.8$. The fiducial instrumental throughput $\phi_{ref}^{inst}(\lambda)$ for $ugrizY$-bands is also shown in the plot as reference. Bottom panels: Synthetic SCE in $ugrizY$-bands for O5V-M6V stars introduced by this airmass change, as a function of $g - i$ color.
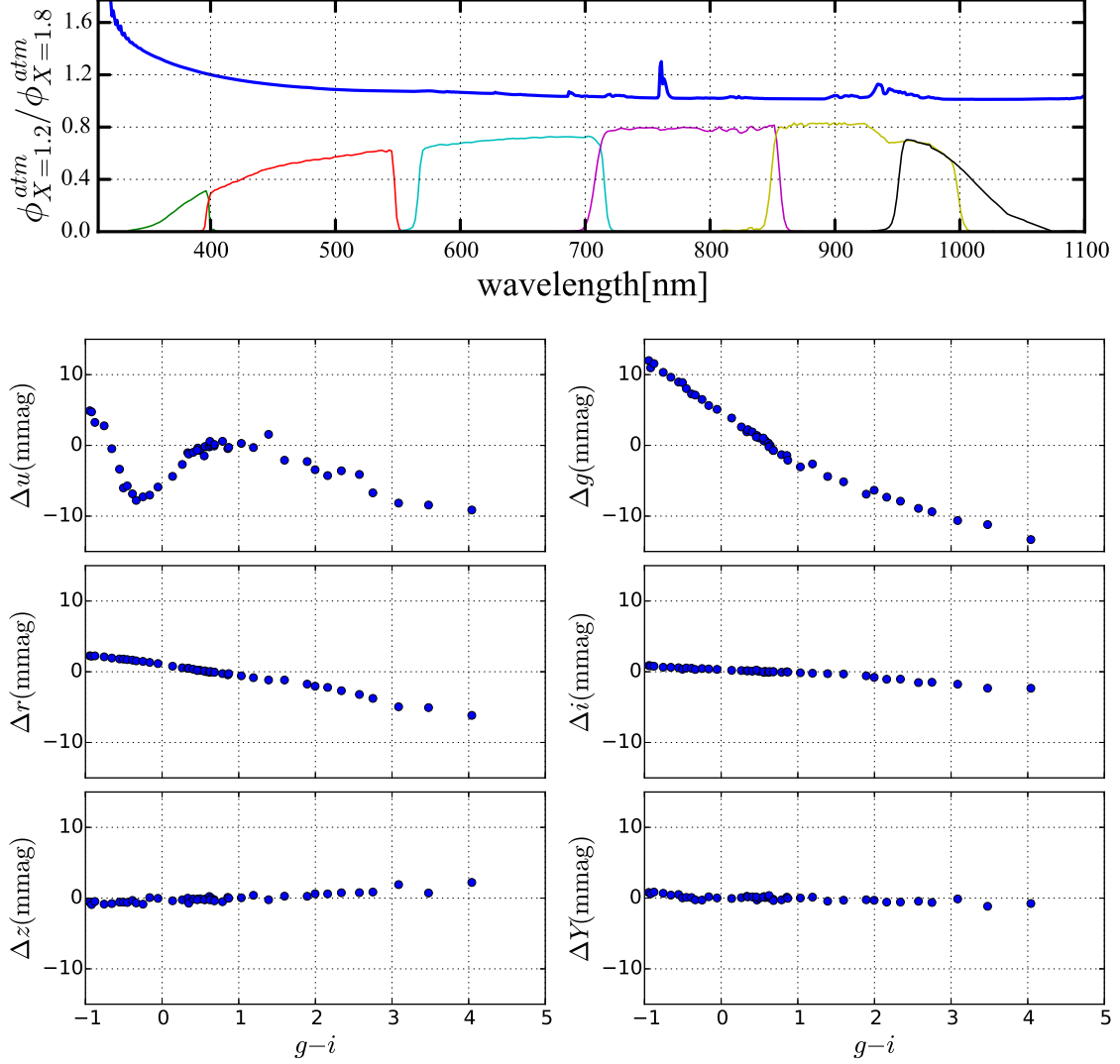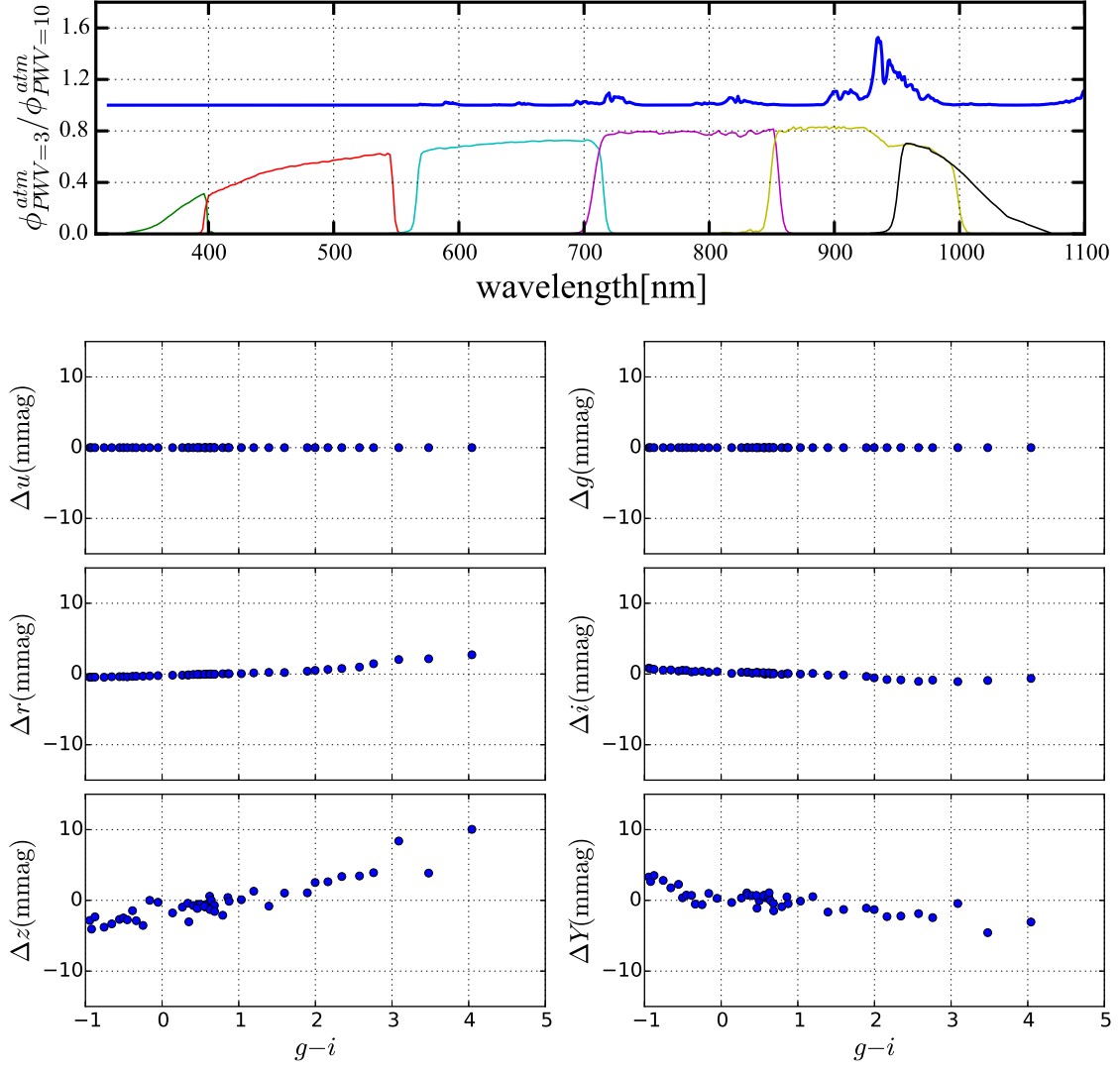
Figure 5.3: Synthetic SCE caused by a change in PWV. Top panel: The ratio of the atmospheric transmission for two PWV values, $PWV = 3$ mm and $PWV = 10$ mm. Bottom panels: Synthetic SCE in $ugrizY$-bands for O5V-M6V stars introduced by this PWV change, as a function of $g - i$ color.

wavelength and define it as a changed instrumental throughput $\phi^{inst}(\lambda)$. We then calculate Δm due to this shift for O5V-M6V stars, shown in Figure 5.4 and Table 5.1. We again use a G2V star as reference to remove the grey term, as this is removed by the illumination correction using star-flats in the calibration procedure of DES. Except for u-band, Δm in the other 5 bands are at the level of 1-2%. The actual bandpass shifts from the DECal scans in $griz$ bandpasses are roughly 1, 3, 6 and 2 nm respectively, but only one of the bandpass edges shift, instead of both. The u- and Y-band show almost no edge shift. More details about DECal and bandpass variations will be presented in Marshall et al. in prep.

5.4 Systematic Chromatic Errors in Stars as Seen in DES Observations

As noted earlier, DES obtains its data with the DECam camera on the Blanco 4m telescope at CTIO. The data are transferred in near real-time over the course of each night to the National Center for Supercomputing Applications (NCSA) at the University of Illinois at Urbana-Champaign, where the DES Data Management (DESDM) team performs an initial nightly processing of the data, including image detrending, cataloging, and astrometric calibration of the individual exposures. There is also an annual re-processing, which includes a full re-processing of the single-epoch exposures, a global photometric calibration of the data, and a coadd of overlapping exposures. An overview of the process is described in Balbinot et al. (2015), and details can be found in Gruendl et al. (in preparation). The current global photometric calibration only considers the grey-scale zeropoint correction, and therefore the SCE have not been corrected in the current catalog. In order to show that SCE exist in the catalog, we used the calibrated photometry derived using single epoch exposures from DES.

In this section, we give two examples using a test sample from DES data. We
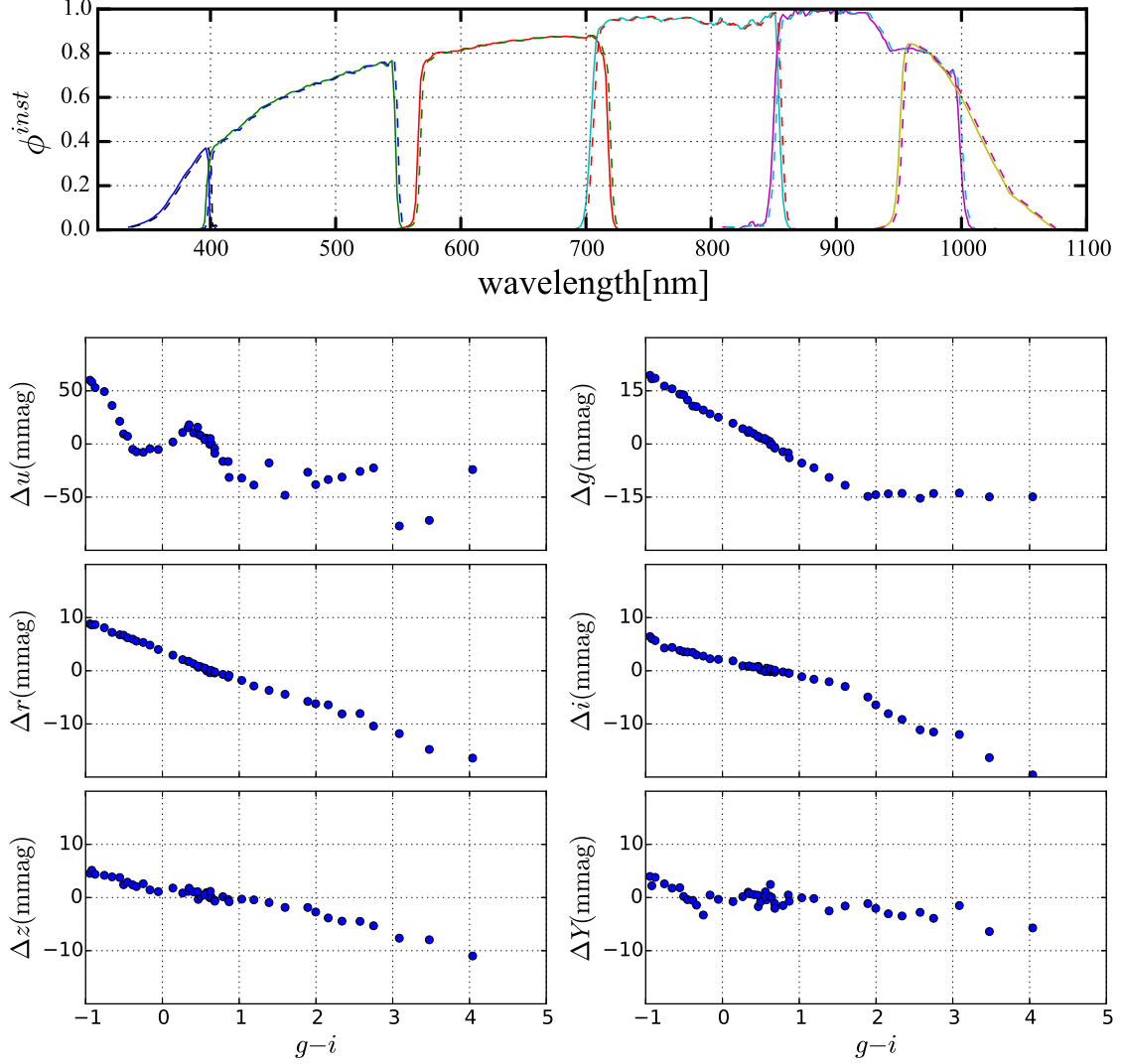
Figure 5.4: Synthetic SCE caused by a bandpass shift. Top panel: Solid lines are the fiducial instrumental throughput $\phi_{ref}^{inst}(\lambda)$ for $ugrizY$-bands. Dashed lines are the instrumental throughput with a 2 nm shift towards the longer wavelength. Bottom panels: Synthetic SCE in the $ugrizY$-bands for O5V-M6V stars introduced by this 2 nm bandpass shift, as a function of $g - i$ color. Note that the scales for the $u-$ and $g-$band are different from the other four bands.

present the SCE due to the PWV variation and due to the location on the DECam the focal plane. We show that SCE in DES observations match synthetic SCE to within a few mmag, which suggests that corrections based on measurements from the auxiliary calibration system (aTmCam + DECal) can be used to significantly improve photometric precision.

5.4.1   SCE due to PWV Variation

We first show how the change of the PWV in the atmosphere affects the photometry in DES. The PWV was measured by aTmCam during DES observations.

Standard star fields are observed on every photometric night in the DES during evening and/or morning twilight. For one of DES standard star fields SDSSJ2300+0000 (~ 3 deg^2), Figure 5.5 shows the $z-$band stellar photometry difference, Δz, between two exposures taken on different nights, as a function of $g - i$ color of the stars. Δz is derived from the photometry in the single epoch catalog from the standard star calibration exposures. The position of the stars on the CCD focal plane in two standard star exposures is constant to within the pointing error of the telescope (roughly 5 arcsec), so there are no significant SCE from the variation of the instrumental throughput over the focal plane. The exposures are selected to be taken at the same airmass to ensure there are no SCE from the airmass change. The selection criteria of -0.002 $< spread\_model\_i^6 <$ 0.002 and $z < 18$ mag are applied in order to ensure that the targets are all bright stars so that the statistical errors from photon fluctuations are negligible (< 5mmag on average). We adopted the $g - i$ color for each star from the photometry in the coadd catalog. Since the coadd photometry is essentially the average over many exposures taken under different conditions, the

---

[6]Spread model is a parameter measured by SExtractor (Bertin & Arnouts, 1996). It describes whether an object is better fit by the PSF or a broadened version of the PSF. It may be used as an indicator for star-galaxy separation.(Desai et al., 2012)

$g - i$ color from coadd catalog is averaged over different SCE and might be slightly different from the $g - i$ color from a single-epoch. However, this should not be a problem as such a color difference would be a second-order effect to the SCE and should be negligible (i.e. < 1 mmag).

We first calculate Δz for two exposures for nights 2014-11-13 and 2014-11-12, which has $PWV = 3.6$ mm and $PWV = 4.2$ mm from the measurements by aTm-Cam, shown in the top left panel of Figure 5.5; we then perform the same calculation on nights 2014-11-13 and 2014-11-15, which have $PWV = 3.6$ mm and $PWV = 13.6$ mm, shown on the top right panel. In both cases, there are more than 3000 stars matched from 2 exposures. There is an obvious trend in the top right panel showing that Δz is correlated with $g - i$ when there is a large difference between the PWV values.

We divide these stars into 8 equal-width bins over the range $0.2 < g - i < 3.7$. Except for the last bin which only has about 60 stars, all bins have more than 300 stars. We calculate the average of Δz in each bin, shown as the red filled circles in the middle panels of Figure 5.5. The error bars show the error of the mean in each bin. On nights with similar PWV, the average of Δz is consistent with zero for all types of stars, as shown in the middle left panel. However, on the nights with a large difference in PWV, the average of Δz deviates from zero for red stars, as shown in the middle right panel. The most significant difference is at $g - i \sim 3.5$, where Δz is almost 4-σ away from zero. This is strong evidence showing the existence of SCE when the PWV changes.

We calculated the synthetic Δz when the atmospheric transmission changes from PWV=3mm to PWV=13mm. We followed the same steps as discussed in Section 3.1, except that instead of using a G2V star as the reference star, we used stars with $g - i \sim 2$ as reference stars to remove the grey-term variation, as stars with $g - i \sim 2$

tend to have zero errors in Δz between these two exposures. Furthermore, instead of using the Pickles Atlas, we used the stellar template from Next Generation Spectral Library[7] (NGSL), which contains flux calibrated stellar templates for more than 350 stars. We note that the synthetic SCE calculated using NGSL and the Pickles Atlas generally show the same trend. As shown in Figure 5.3, the synthetic SCE using the Pickle Atlas have a few millimag of scatter in z- and Y-band. We therefore adopted NGSL to compare with DES data as it contains a much larger sample of stellar templates. The synthetic SCE calculated using each stellar template in NGSL are shown as open circles in the middle right panel of Figure 5.5.

We then fit a third-order polynomial to the computed synthetic Δz, and show this curve as a green line in middle right panel of Figure 5.5. The difference between the DES data and a fit to the synthetic SCE using the NGSL templates are shown in the lower panels of Figure 5.5. The difference is less than 2 mmag over the $g-i$ color range. We emphasize that the fit is *NOT* to DES data, but rather it demonstrates that the SCE due to the measured PWV change between the two nights are removed exceptionally well.

5.4.2   SCE due to Location on the DECam Focal Plane

Here we show how the variation of instrumental throughput over the DECam focal plane affects the photometry in DES. We use i-band as the example since i-band has the largest bandpass edge shift measured from the results of DECal scans.

We divide the DECam focal plane into 4 regions based on the location of the center of the 62 CCD chips on the focal plane: Region 1 (0-$0.1R_{max}$), Region 2 ($0.1R_{max}$-$0.3R_{max}$), Region 3 ($0.3R_{max}$-$0.6R_{max}$), and Region 4 ($0.6R_{max}$-R_{max}), where R_{max} is the maximum radius of the focal plane. The relative throughputs from DECal
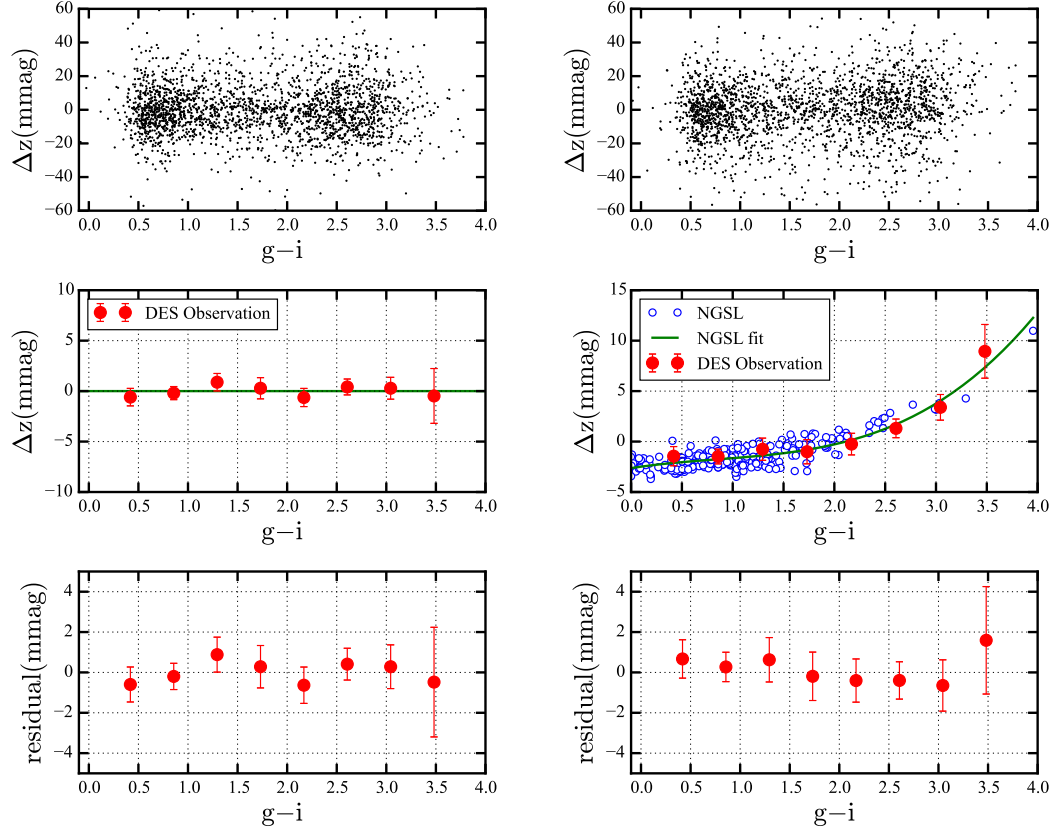
---

[7]https://archive.stsci.edu/prepds/stisngsl/

Figure 5.5: Measurements of the differences of z-band photometry, Δz, on two nights with similar PWV (left) and two nights with different PWV (right), as a function of the $g-i$ color of stars. Top panels: Each black dot is a Δz from one star. Middle panels: Stars with $0.2 < g - i < 3.7$ are divided into 8 bins and the average of Δz in each bin is calculated and shown as the red filled circles. The error bars show the error of the mean in each bin. A green line of $\Delta z = 0$ is shown on the left as the PWV is similar on those two nights. On the right panel, the green line is a third-order polynomial fit to the synthetic SCE calculated using the atmospheric transmission models and the stellar templates, shown as the blue open circles. Bottom panels: Residuals of the average of Δz in each bin, after corrections with the fit to the synthetic errors (i.e. green lines) in the middle panels.

scans around the blue (red) edge are shown in the top (bottom) left panel of Figure 5.6. The average throughput in four different regions is normalized to the value at 770 nm. The figure shows that there is about a 6 nm shift at the blue edge when comparing the center of the focal plane to the edge of the focal plane.

We use the calibrated DES data in the same area as the standard star field SDSSJ2300+0000 to calculate the SCE in i-band. We use the single epoch results from the survey exposures instead of the standard star calibration exposures. Since the tilings from the survey exposures have some small spatial offset (i.e. "dithered"), each star has been observed multiple times using different regions of the DECam focal plane. The same selection criteria as in Section 4.1 ($-0.002 < spread\_model < 0.002$ and z < 18 mag) are applied in order to ensure that the targets are all bright stars. We also make an airmass requirement ($1.12 < X < 1.22$) to ensure minimal SCE from the change of airmass. We then determine the $i-$band magnitude in four regions as described above, i_1, i_2, i_3, and i_4 for Region 1 to 4, respectively. For each star observed in Region 4, we find the same star in the other three regions when it is available and calculate the difference Δi. We found 291 matches for Regions 1 & 4; the differences $\Delta i_{14} = i_1 - i_4$ are calculated and shown in the top left panel of Figure 5.7. We bin the DES data in a similar way as in Section 4.1 and calculate the synthetic SCE using the stellar spectra from NGSL, the instrumental throughputs for Regions 1 & 4 from the DECal scans and the fiducial atmospheric transmission model, shown in the middle left panel of Figure 5.7. A fourth-order polynomial fit to the synthetic SCE is shown as the green line in the same panel. We repeat the calculation and show the Δi for Regions 2 & 4 and Regions 3 & 4 in the middle column and right column of Figure 5.7. There are 1890 matches for Regions 2 & 4 and 4189 matches for Regions 3 & 4, respectively. The bottom panels show the residuals of the binned Δi after correction using the fit from the synthetic SCE
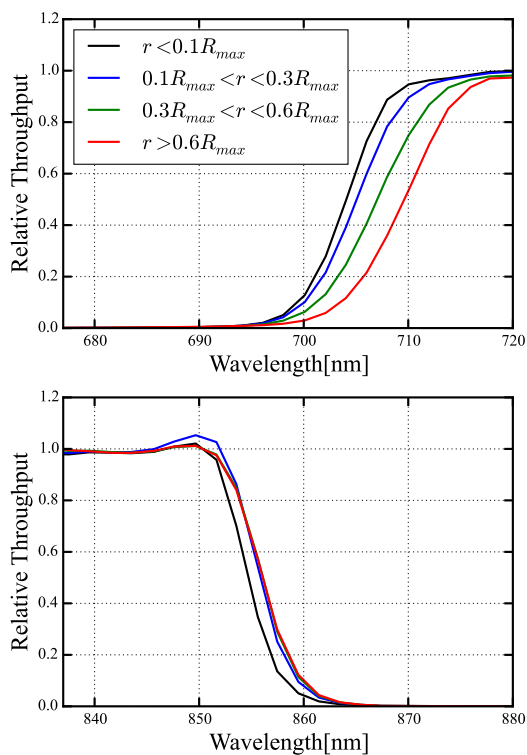
Figure 5.6: The relative throughput from a DECal scan around the cut-on (cut-off) wavelength in the top (bottom) panel from 4 regions defined in the text. The throughput is normalized at 770 nm. Note there is about a 6 nm shift from the center of the focal plane to the edge of the focal plane.

calculation. We show here that Δi after the correction is less than $< 3\text{mmag}$ for any stars at any position of the focal plane.

The SCE due to position change are essentially the instrumental color-term over the DECam focal plane. It is usually calculated empirically using stars to get the correction to first order. Such empirical linear color corrections are good for stars with $0 < g - i < 2$. However, for very red stars and non-stellar objects, an empirical linear correction is not sufficient.
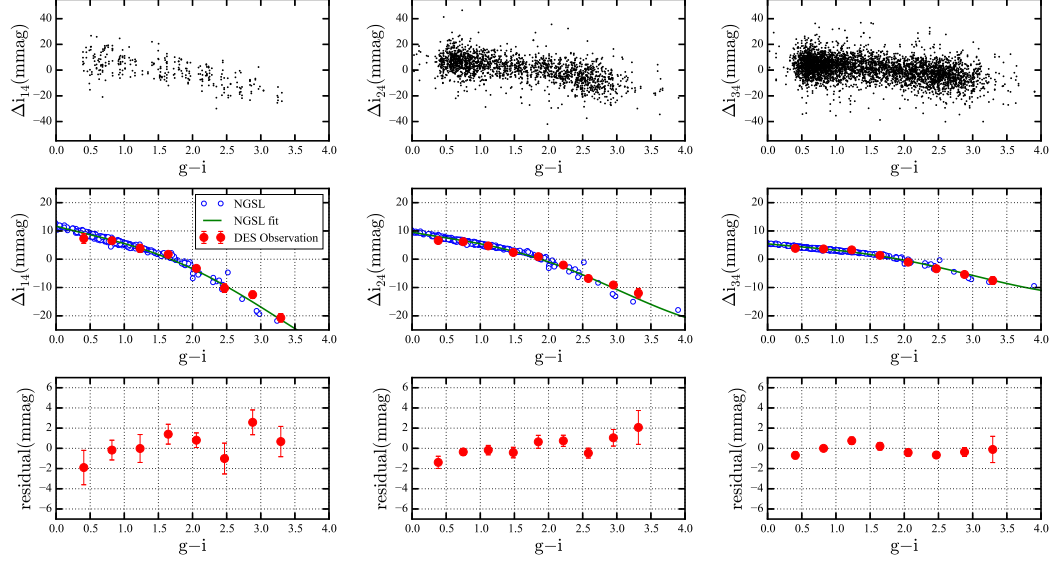
Figure 5.7: Measurements of the differences of i-band photometry, Δi, from 4 regions defined in the text, as a function of the $g-i$ color of stars. Top panels: Δi for Regions 1 & 4 (left), Regions 2 & 4 (middle) and Regions 3 & 4 (right), as a function of $g-i$ color. There are 291, 1890, and 4189 points in the left, middle and right panels, respectively. Middle panels: We divided these stars into 8 bins and then calculated the average of Δi in each bin, shown as the red filled circles. The error bars show the error of the mean in each bin. Also calculated are the synthetic SCE using the stellar spectra from NGSL, shown as the blue open circles. A fourth-order polynomial fit to the synthetic SCE is shown as the green line. Bottom panels: Residual plots of the binned Δi minus the fit from the synthetic SCE. Note that the vertical scale for each panel is different.

Table 5.2: Residual Errors on a M6V Star ($g - i \sim 4$) When a Measurement by an Auxiliary Instrument Has Small Uncertainties.

Component	Measured	True	Synthetic Residual SCE (mmag)					
			u	g	r	i	z	Y
Aerosol	AOD= 0.02, $\alpha = 1$	AOD= 0.04, $\alpha = 1$	−0.36	−1.3	−0.68	−0.41	−0.15	−0.02
	AOD= 0.20, $\alpha = 1$	AOD= 0.20, $\alpha = 0.9$	0.47	1.4	0.58	0.28	0.08	0.01
PWV	PWV = 3 mm	PWV = 3.3 mm	0	0	0.25	−0.05	0.92	−0.27
Instrument	DECal scan	shift 0.2 nm	−6.9	−1.5	−1.6	−1.9	−1.0	−0.74

5.4.3   Residual Errors After Correction

Above we show that measurements of the atmospheric transmission and instrumental throughput can be used to correct imaging data to high photometric precision. Any system that determines the shape of the atmospheric transmission, however, will not produce perfect results and there will be errors in the determined values of the PWV, AOD, etc. Table 5.2 shows the effects of uncertainties in the determination of the important parameters. Notably, measurements of the PWV that are accurate to ∼10% generally are adequate to ensure that residual errors after correction are less than 1 mmag in all DECam bands. Similarly, AOD and α determinations accurate to 0.02 and 0.1 also generally produce corrections that give less than ∼1 mmag residual errors.

Measurement of the variation in instrumental throughput across the focal plane generally require determination of the wavelengths of any shift in the bandpass to ∼0.2 nm precision. Determination of the bandpass to this level will give < 2 mmag residual error in most bands.

5.5   Synthetic Systematic Chromatic Errors on Non-Stellar Objects

Since the SED of a non-stellar object is significantly different from a star, the SCE on some of the non-stellar objects can be larger than what we have seen for stars. We show two examples in this section: Type Ia supernovae (SNe Ia) and

elliptical galaxies. We calculate the synthetic SCE Δm for these two types of objects using Equation 5.9. As the shape of the SEDs changes with redshift, the Δm are also redshift dependent.

5.5.1 Type Ia Supernovae

For the DES survey, the sub-percent photometry precision goal comes from supernova cosmology, which needs precise photometry so that one can measure the luminosity distances of SNe Ia over a wide redshift range.

Here we give an example of how the synthetic SCE change with redshift. Figure 5.8 shows Δm caused by a PWV change from 3 mm to 10 mm for a Type Ia supernova (SN Ia) as a function of redshift z. We use the SED from SN2011fe (Pereira et al., 2013) as the template for the calculation. The template was taken 0.27 days prior to maximum brightness. The peak-to-valley errors can be as large as 20 mmag for z- and Y- band over redshift $z = 0$ to $z = 1$, shown as the blue solid lines. Because a SN Ia SED is very different from that of a star, the SCE for a star and a SN Ia are very different, even if they share the same $g - i$ color. The red dashed lines in Figure 5.8 show the SCE residuals after naively using the corrections derived from stars with the same $g - i$ color as the SNe Ia, i.e. synthetic SCE calculated in Section 3.1. As the figure shows, the SCE are not properly corrected, and sometimes are even larger.

In Table 5.3, we summarize the synthetic SCE on SNe Ia by the changes of other atmospheric components or by a 2 nm shift. It is similar to Table 5.1 except that the SCE here are calculated as the peak-to-valley SCE over redshift $z = 0$ to $z = 1$.

5.5.2 Galaxies

Precise photometry helps the determination of photometric redshifts of galaxies (Ilbert et al., 2006). We therefore study the synthetic SCE for galaxies. We used

a spectral template of elliptical galaxies from Coleman et al. (1980) for this calcula-
tion. We summarize the peak-to-valley SCE on elliptical galaxies over redshift $z = 0$
to $z = 2$ in Table 5.4. As an example, Figure 5.9 shows Δm caused by a 2 nm shift
of the instrumental throughput towards longer wavelength, as a function of redshift.
The drop of Δr around redshift $z = 0.4$, Δi around redshift $z = 0.8$, Δz around
redshift $z = 1.1$ and ΔY around redshift $z = 1.3$ are due to the 4000 Å break. We
again use the correction derived from stars with the same $g - i$ and the SCE residuals
after correction are shown as red dashed lines in the same figure.

Similar to SNe Ia, the SCE are not properly corrected since the galaxy SED is
different from that of a star. However, it is worth noting that the star-derived cor-
rections using $g - i$ color actually slightly correct the SCE on galaxies. For example,
in $griz$-bands, the red lines (after correction) are much closer to zero compared to
the blue lines (before correction) for redshift $z < 1$. Here, we derive the corrections
based on a fixed color $g - i$. This might be good enough for regular stars, as they
form a well-defined stellar locus on a color-color diagram. We pick $g - i$ throughout
the paper since $g - i$ ranging from -1 to 4 separates the blue stars from red stars[8].
However, $g - i$ might not be the best choice for SNe Ia and galaxies. Choosing a
color close to the band of interest, e.g., $g - r$ for g-band, and $z - Y$ for z-band
and/or Y-band, or choosing a combination of multiple colors, might be better for
these non-stellar objects. We leave further discussion of this to future work.

5.6 Conclusions

In this paper, we have demonstrated that the variation of the atmospheric trans-
mission and the instrumental throughput introduce systematic chromatic errors (SCE)
that depend on the color of the source object. We assess such SCE for the Dark En-

---

[8]For example, $g - r$ is not a good color to pick for red stars since all K and M stars tend to clump
around $g - r \sim 1.5$. Therefore, it is hard to correct the SCE on red stars using $g - r$ color.
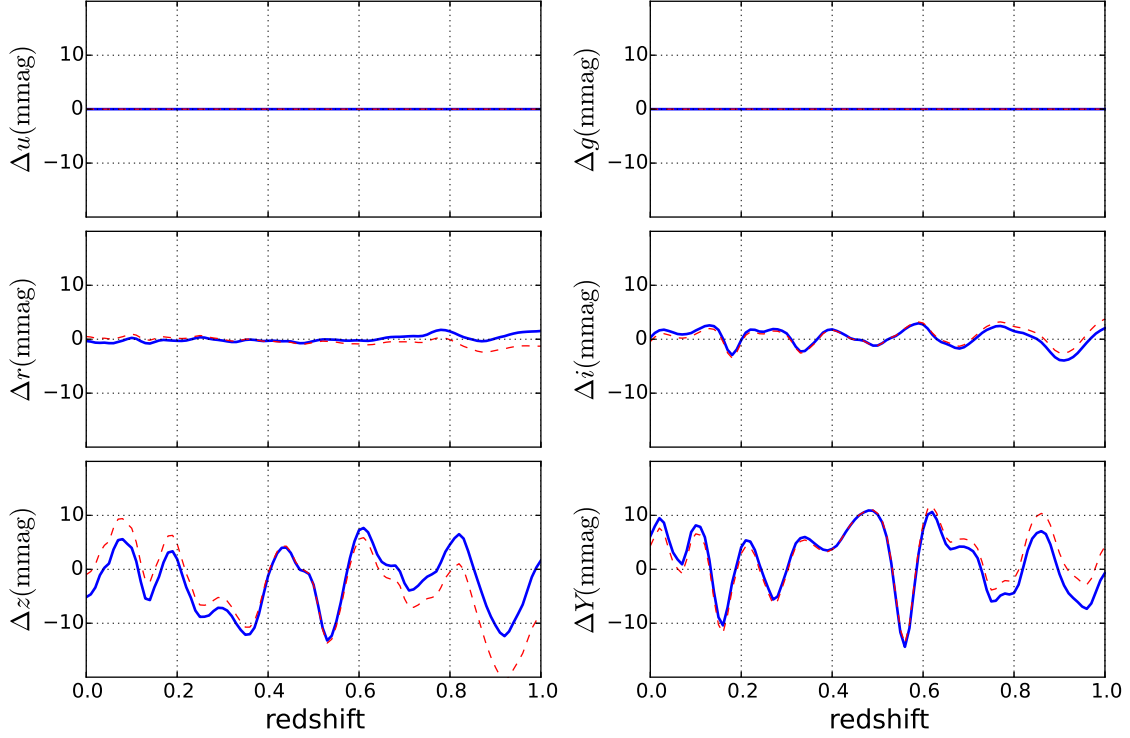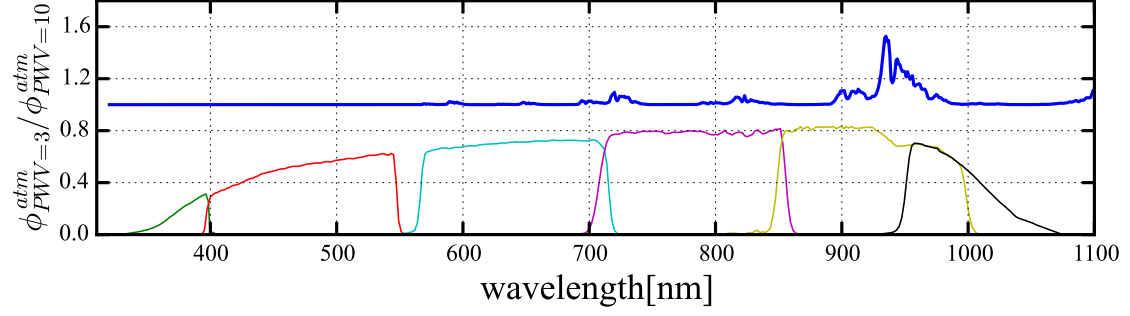
Figure 5.8: Synthetic SCE in $ugrizY$-bands for SNe Ia as a function of redshift when the PWV in the atmosphere changes from 3mm to 10mm, shown as the blue sold lines. The red dashed lines are the residual errors after using the correction derived for stars with the same $g - i$ color as the SNe Ia.

Table 5.3: Peak-to-Valley SCE on SNe Ia over Redshift $z = 0$ to $z = 1$.

Component	Fiducial	Changed	Synthetic SCE (mmag)					
			u	g	r	i	z	Y
Pressure	$P_0 = 779$ hpa	$P_0 = 789$ hpa	0.8	0.9	0.1	0.2	0.1	0.1
Aerosol	AOD= 0.02, $\alpha = 1$	AOD= 0.20, $\alpha = 1$	11	26	7	4	2	1
	AOD= 0.02, $\alpha = 1$	AOD= 0.20, $\alpha = 0.5$	4	11	3	2	1	0.7
PWV	PWV = 3 mm	PWV = 10 mm	0	0	3	7	20	27
Ozone	Ozone = 270 DU	Ozone = 230 DU	0.04	1.7	1	0.1	0	0
Airmass	$X = 1.2$	$X = 1.8$	31	30	7	4	6	7
Instrument	DECal scan	shift 2 nm	186	99	33	22	19	28

101
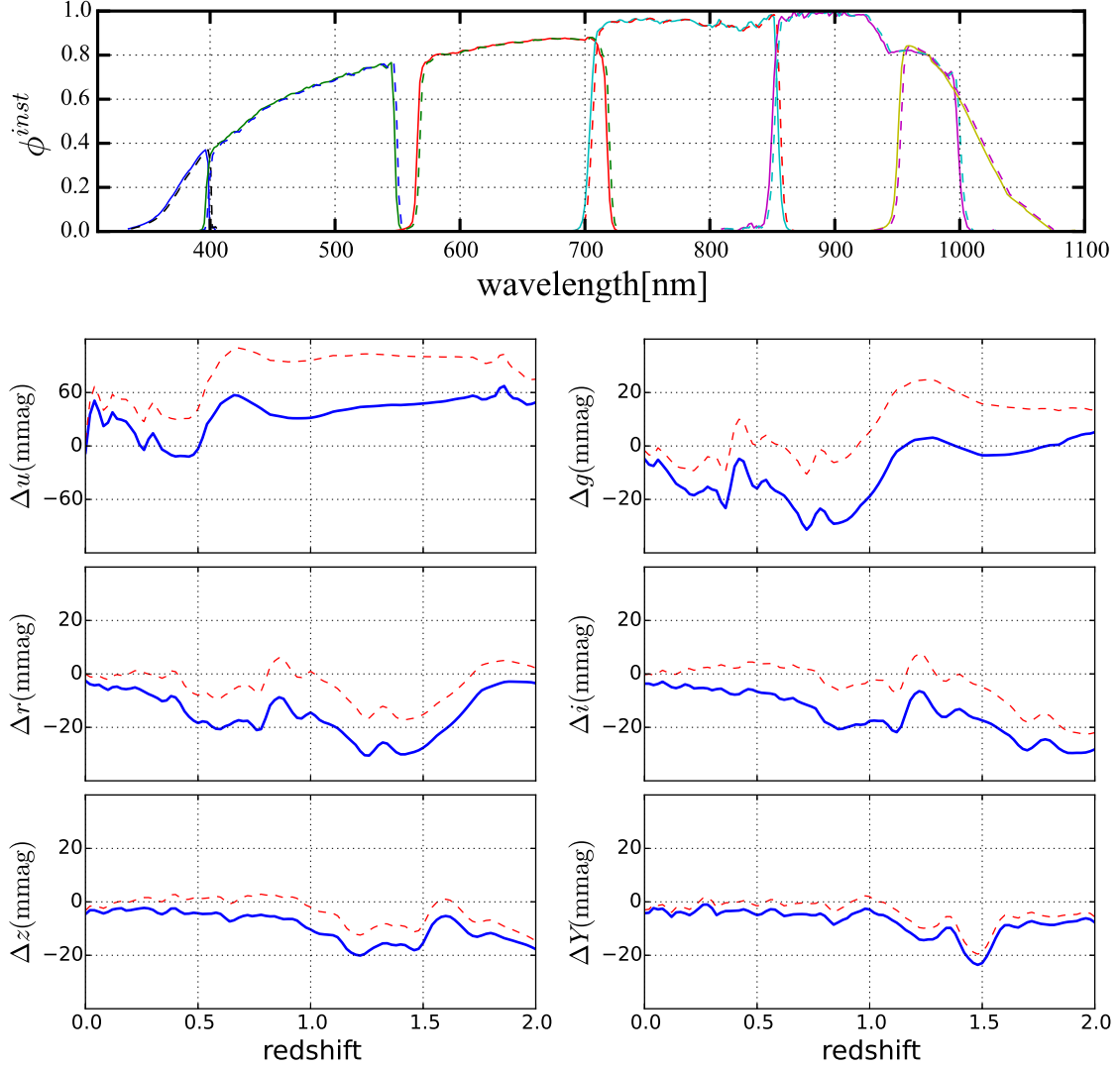
Figure 5.9: Synthetic SCE in *ugrizY*-bands for elliptical galaxies as a function of redshift, when the instrumental throughput is moved by 2 nm toward longer wavelength. The red dashed lines show the residual errors after using the correction derived for stars with the same $g - i$ color as the elliptical galaxies. Note that the scale for $u-$band is different from the other five bands.

102

Table 5.4: Peak-to-Valley SCE on Elliptical Galaxies over Redshift $z = 0$ to $z = 2$.

Component	Fiducial	Changed	Synthetic SCE (mmag)					
			u	g	r	i	z	Y
Pressure	$P_0 = 779$ hpa	$P_0 = 789$ hpa	0.6	0.6	0.07	0.1	0.04	0.03
Aerosol	AOD= 0.02, $\alpha = 1$	AOD= 0.20, $\alpha = 1$	7	18	10	4	3	1
	AOD= 0.02, $\alpha = 1$	AOD= 0.20, $\alpha = 0.5$	3	7	5	2	2	0.7
PWV	PWV = 3 mm	PWV = 10 mm	0	0	4	4	26	20
Ozone	Ozone = 270 DU	Ozone = 230 DU	0.03	1.2	1.6	0.1	0	0
Airmass	$X = 1.2$	$X = 1.8$	26	21	11	4	7	6
Instrument	DECal scan	shift 2 nm	79	36	28	26	17	22

ergy Survey (DES) as an example:

- For stars, the SCE caused by the change of airmass in each exposure and the change of precipitable water vapor and aerosol in the atmosphere can be larger than 1%;

- The SCE caused by the change of the barometric pressure and ozone are smaller than 0.1% (or 1 mmag);

- The SCE caused by the bandpass edge shift over the detector focal plane can be as large as a few percent.

- The SCE can be corrected to 2-3 mmag or better if the shape of the atmospheric transmission and the instrumental throughput are well measured by auxiliary calibration system such as aTmCam and DECal.

- For supernovae and galaxies, these SCE are expected to be larger and also redshift-dependent. Figure 5.8 and 5.9 give examples of how SCE change as a function of redshift for Type Ia supernovae and elliptical galaxies.

- For stars, we could derive a color term to first order and approximately correct the SCE. However, such linear stellar color terms are not sufficient for getting color corrections for extremely red stars, SNe and galaxies.

From this study, we suggest that, for large imaging surveys such as DES and LSST, one should first define a natural system response that represents the average condition of the survey, and also define a stellar SED as the reference SED that represents the average color of the calibration stars in the survey. Then for each stellar object, one could calculate the synthetic SCE using the stellar SED library together with the stellar color, as described in this paper, and use the synthetic SCE as the corrections. For non-stellar objects like SNe Ia or galaxies, the redshifted SED need to be given as an input to derive such corrections.

Even though SCE are systematic errors for each exposure, they will eventually introduce additional scatter on the final coadd photometry and affect the photometric precision of the surveys with multiple visits. This is true because: 1) the atmospheric transmission varies over a wide range of conditions and each exposure is likely to be taken with a different condition; 2) each exposure in the survey has a slight offset for multiple tilings so that the same object does not fall on the same location on the focal plane. Averaging over different conditions and different focal plane positions can reduce the amount of SCE in the final coadd photometry. Exceptions include supernovae and other transients, for which there is only one measurement in a particular epoch.

Last but not least, the SCE calculated here are not limited to photometric calibrations in large surveys. They can also be applied to any ground-based differential photometric measurements, such as exoplanet transients. For example, if the planet host is an M6V star and reference stars are G2V stars, then PWV changes over time affect the photometry in z-band to $\sim 1\%$, which is comparable or even larger than the signal from a super-Earth transiting an M star (Blake & Shaw, 2011). Similarly, variations in either the atmospheric transmission or instrumental throughput can also affect such measurements in other bands.

6. SUMMARY

In this dissertation, we have presented a few work towards understanding the nature of stellar clouds using the data sets from large area sky surveys. While we have not yet succeeded in matching the observation with the simulation predictions, we have made progress in understanding them, particularly on a newly-discovered cloud-like structure, and we can now point the way to future investigators.

In Section 2, we present the analysis of spectroscopic observations of individual stars from the two candidate structures found in the M-giant catalog in Two Micron All-Sky Survey (2MASS).The follow-up observations show that A13 is a real structure and kinematically consistent with the GASS structure Crane et al. (2003) found, so A13 is possibly associated with Monoceros Ring. The Galactic latitude of this structure extends to $b \sim 40°$ and the heliocentric distance extends to 20 kpc. This is further than any of the known extension of the Monoceros Ring. On the other hand, most of the A11 stars turn to be foreground M-dwarfs, instead of distant M-giants. A11 is a false detection, probably due to the systematic photometric errors in 2MASS or dust extinction. The lesson from follow-up on A11 tells us that we must thoroughly understand the systematics of large area sky surveys in order to avoid false detection on searching for substructures in the faint limit of the survey.

In Section 3, We report the discovery of a Galactic halo stellar overdensity in the Southern hemisphere from the first annual internal release catalog of the first year DES data. This overdensity resides in the constellations of Eridanus and Phoenix, centered around $(l, b) \sim (285°, -60°)$ and spanning at least 30° in longitude and 10° in latitude. The full scope of the Eridanus-Phoenix (EriPhe) overdensity may extend farther, but it is limited by the coverage of the first year data. The stellar

population in the overdense region has a similar distribution in color-magnitude space as the nearby globular cluster NGC 1261, indicating that the heliocentric distance of EriPhe is about $d \sim 16$ kpc and the Galactocentric distance is about $d \sim 18$ kpc. We propose two possible scenarios for the creation of the EriPhe overdensity which both involve the tidal stripping and disruption of satellite galaxies. One suggests that EriPhe might be associated with the Phoenix stream and NGC 1261; the other one suggests a possible polar orbit structure formed by EriPhe, VOD, and HerAq stellar overdensities. Whether or not EriPhe is part of the polar orbit structure, or it is the remnant of a dwarf galaxy with two globular cluster companions (i.e. NGC 1261 and the progenitor of the Phoenix Stream), needs to be tested with future observations. Proper motions measured by Gaia may further inform which hypothesis is favored. Moreover, spectroscopic follow-up on the Phoenix stream and EriPhe can provide more information on the kinematics and metallicities of these two structures, and improve our understanding of the nature of the EriPhe overdensity. Further study of cloud-like overdensities like EriPhe can also provide insight to probing the gravitational potential of the Milky Way (Sanderson & Helmi, 2013).

As we learned that systematic photometric errors can cause false detection in finding the halo substructure, such as the A11 candidate, we also studied how to improve the photometric calibration in DES in addition to the scientific discoveries. We have designed and built two auxiliary calibration systems and present a detailed description of the two systems in this dissertation. We then discuss how the auxiliary systems in DES can be used to calibrate the photometry on the systematic chromatic errors – source color-dependent systematic errors that caused by variations in the wavelength dependence of the atmospheric transmission and the instrumental throughput. These systematic errors must be corrected to achieve the most precise

photometric measurements. We conclude that the systematic chromatic errors caused by the change of airmass in each exposure, the change of the precipitable water vapor and aerosol in the atmosphere over time, and the non-uniformity of instrumental throughput over the focal plane, can be up to 0.02 mag in some bandpasses. We compare the calculated systematic chromatic errors with the observed DES data. For the test sample data, we correct these errors using measurements of the atmospheric transmission and instrumental throughput from auxiliary calibration systems. The residual after correction is less than 0.003 mag.

REFERENCES

Abbott, T., et al. 2005, arXiv:astro-ph/0510346

Alam, S., Albareti, F. D., Allende Prieto, C., et al. 2015, ApJS, 219, 12

Armandroff, T. E., & Zinn, R. 1988, AJ, 96, 92

Balbinot, et al. 2015, submitted to ApJ, arXiv:1509.04283

Balbinot, E., Santiago, B. X., da Costa, L., et al. 2013, ApJ, 767, 101

Balbinot, E., Santiago, B. X., Girardi, L., et al. 2015, MNRAS, 449, 1129

Battaglia, G., Irwin, M., Tolstoy, E., et al. 2008, MNRAS, 383, 183

Bechtol, K., Drlica-Wagner, A., Balbinot, E., & Pieres. 2015, ApJ, 807, 50

Bell, E. F., Zucker, D. B., Belokurov, V., et al. 2008, ApJ, 680, 295

Belokurov, V., Zucker, D. B., Evans, N. W., et al. 2006a, ApJ, 647, L111

—. 2006b, ApJ, 642, L137

Belokurov, V., Evans, N. W., Bell, E. F., et al. 2007, ApJ, 657, L89

Berk, A., et al. 1998, Remote Sensing of Environment, 65, 367

Bertin, E. 2011, in Astronomical Society of the Pacific Conference Series, Vol. 442,
    Astronomical Data Analysis Software and Systems XX, ed. I. N. Evans, A. Acco-
    mazzi, D. J. Mink, & A. H. Rots, 435

Bertin, E., & Arnouts, S. 1996, A&AS, 117, 393

Bessell, M. S. 1990, PASP, 102, 1181

Betoule, M., Marriner, J., Regnault, N., et al. 2013, A&A, 552, A124

Blake, C. H., & Shaw, M. M. 2011, PASP, 123, 1302

Bonaca, A., Jurić, M., Ivezić, Ž., et al. 2012, AJ, 143, 105

Bovy, J. 2015, ApJS, 216, 29

Bovy, J., Hogg, D. W., & Rix, H.-W. 2009, ApJ, 704, 1704

Bullock, J. S., & Johnston, K. V. 2005, ApJ, 635, 931

Burke, D. L., Axelrod, T., Blondin, S., et al. 2010, ApJ, 720, 811

Burke, D. L., Saha, A., Claver, J., et al. 2014, AJ, 147, 19

Carballo-Bello, J. A., Sollima, A., Martínez-Delgado, D., et al. 2014, MNRAS, 445, 2971

Carlin, J. L., Yam, W., Casetti-Dinescu, D. I., et al. 2012, ApJ, 753, 145

Carlstrom, J. E., Ade, P. A. R., Aird, K. A., et al. 2011, PASP, 123, 568

Carollo, D., Beers, T. C., Lee, Y. S., et al. 2007, Nature, 450, 1020

Carollo, D., Beers, T. C., Chiba, M., et al. 2010, ApJ, 712, 692

Carrera, R. 2012, A&A, 544, A109

Carrera, R., Pancino, E., Gallart, C., & del Pino, A. 2013, MNRAS, 434, 1681

Cenarro, A.-J. 2003, PASP, 115, 504

Cenarro, A. J., Cardiel, N., Gorgas, J., et al. 2001, MNRAS, 326, 959

Cole, A. A., Smecker-Hane, T. A., Tolstoy, E., Bosler, T. L., & Gallagher, J. S. 2004, MNRAS, 347, 367

Coleman, G. D., Wu, C.-C., & Weedman, D. W. 1980, ApJS, 43, 393

Cooper, A. P., Cole, S., Frenk, C. S., et al. 2010, MNRAS, 406, 744

Crane, J. D., Majewski, S. R., Rocha-Pinto, H. J., et al. 2003, ApJ, 594, L119

Dambis, A. K. 2006, Astronomical and Astrophysical Transactions, 25, 185

Dark Energy Survey Collaboration, Abbott, T., Abdalla, F. B., et al. 2016, MNRAS, 460, 1270

DeLucia, G., & Helmi, A. 2008, MNRAS, 391, 14

Desai, S., Armstrong, R., Mohr, J. J., et al. 2012, ApJ, 757, 83

Diehl, H. T., et al. 2014, Proc. SPIE, 9149, 0

Doi, M., Tanaka, M., Fukugita, M., et al. 2010, AJ, 139, 1628

Dotter, A., Chaboyer, B., Jevremović, D., et al. 2008, ApJS, 178, 89

Drlica-Wagner, A., Bechtol, K., Rykoff, E. S., et al. 2015, ArXiv e-prints, arXiv:1508.03622

Du, W., Luo, A. L., & Zhao, Y. H. 2012, AJ, 143, 44

Duffau, S., Vivas, A. K., Zinn, R., Méndez, R. A., & Ruiz, M. T. 2014, A&A, 566, A118

Duffau, S., Zinn, R., Vivas, A. K., et al. 2006, ApJ, 636, L97

Eggen, O. J., Lynden-Bell, D., & Sandage, A. R. 1962, ApJ, 136, 748

Fernandez-Villacanas, J. L., Rego, M., & Cornide, M. 1990, AJ, 99, 1961

Fitzpatrick, E. L. 1999, PASP, 111, 63

Flaugher, B., Diehl, H. T., Honscheid, K., et al. 2015, AJ, 150, 150

Font, A. S., McCarthy, I. G., Crain, R. A., et al. 2011, MNRAS, 416, 2802

Forbes, D. A., & Bridges, T. 2010, MNRAS, 404, 1203

Fulbright, J. P. 2000, AJ, 120, 1841

Glazebrook, K., Peacock, J. A., Collins, C. A., & Miller, L. 1994, MNRAS, 266, 65

Gruendl, et al. in prep, in prep.

Hansen, J. E., & Travis, L. D. 1974, Space Sci. Rev., 16, 527

Harris, W. E. 1996, AJ, 112, 1487

—. 2010, ArXiv e-prints, arXiv:1012.3224

Hayashi, E., Navarro, J. F., Taylor, J. E., Stadel, J., & Quinn, T. 2003, ApJ, 584, 541

Helmi, A. 2008, A&A Rev., 15, 145

Helmi, A., Cooper, A. P., White, S. D. M., et al. 2011, ApJ, 733, L7

Henden, A. A., & Kaitchuck, R. H. 1990, Astronomical photometry : a text and handbook for the advanced amateur and professional astronomer

Hendricks, B., Koch, A., Walker, M., et al. 2014, A&A, 572, A82

Holberg, J. B., & Bergeron, P. 2006, AJ, 132, 1221

Ibata, R. A., Gilmore, G., & Irwin, M. J. 1994, Nature, 370, 194

Ibata, R. A., Irwin, M. J., Lewis, G. F., Ferguson, A. M. N., & Tanvir, N. 2003, MNRAS, 340, L21

Ilbert, O., Arnouts, S., McCracken, H. J., et al. 2006, A&A, 457, 841

Ivezić, Ž., Beers, T. C., & Jurić, M. 2012, ARA&A, 50, 251

Ivezić, Ž., Goldston, J., Finlator, K., et al. 2000, AJ, 120, 963

Ivezić, Ž., Smith, J. A., Miknaitis, G., et al. 2007, AJ, 134, 973

Johnston, K. V., Bullock, J. S., Sharma, S., et al. 2008, ApJ, 689, 936

Johnston, K. V., Sheffield, A. A., Majewski, S. R., Sharma, S., & Rocha-Pinto, H. J. 2012, ApJ, 760, 95

Jurić, M., Ivezić, Ž., Brooks, A., et al. 2008, ApJ, 673, 864

Kim, D., & Jerjen, H. 2015, ApJ, 808, L39

Kim, D., Jerjen, H., Mackey, D., Da Costa, G. S., & Milone, A. P. 2015, ApJ, 804, L44

Kollmeier, J. A., Gould, A., Shectman, S., et al. 2009, ApJ, 705, L158

Koposov, S., de Jong, J. T. A., Belokurov, V., et al. 2007, ApJ, 669, 337

Koposov, S. E., Belokurov, V., Torrealba, G., & Evans, N. W. 2015, ApJ, 805, 130

Laevens, B. P. M., Martin, N. F., Bernard, E. J., et al. 2015, ApJ, 813, 44

Landolt, A. U. 1992, AJ, 104, 340

Li, T., DePoy, D. L., Marshall, J. L., et al. 2014, in Society of Photo-Optical Instrumentation Engineers (SPIE) Conference Series, Vol. 9147, Society of Photo-Optical Instrumentation Engineers (SPIE) Conference Series, 6

Li, T., DePoy, D. L., Kessler, R., et al. 2012, in Society of Photo-Optical Instrumentation Engineers (SPIE) Conference Series, Vol. 8446, Society of Photo-Optical Instrumentation Engineers (SPIE) Conference Series, 2

Libeskind, N. I., Frenk, C. S., Cole, S., et al. 2005, MNRAS, 363, 146

Lord, S. D. 1992, NASA Tech Memorandum, 103957

LSST Science Collaboration, Abell, P. A., Allison, J., et al. 2009, ArXiv e-prints, arXiv:0912.0201

Luck, R. E., & Heiter, U. 2007, AJ, 133, 2464

MacDonald, E. C., Allen, P., Dalton, G., et al. 2004, MNRAS, 352, 1255

Majewski, S. R., Skrutskie, M. F., Weinberg, M. D., & Ostheimer, J. C. 2003, ApJ, 599, 1082

Majewski, S. R., Kunkel, W. E., Law, D. R., et al. 2004, AJ, 128, 245

Majewski, S. R., Schiavon, R. P., Frinchaboy, P. M., et al. 2015, ArXiv e-prints, arXiv:1509.05420

Manfroid, J. 1995, A&AS, 113, 587

Mann, A. W., Gaidos, E., Lépine, S., & Hilton, E. J. 2012, ApJ, 753, 90

Marín-Franch, A., Aparicio, A., Piotto, G., et al. 2009, ApJ, 694, 1498

Martin, N. F., Ibata, R. A., Bellazzini, M., et al. 2004, MNRAS, 348, 12

Martin, N. F., Ibata, R. A., & Irwin, M. 2007, ApJ, 668, L123

Martin, N. F., Nidever, D. L., Besla, G., et al. 2015, ApJ, 804, L5

Martínez-Delgado, D., Gómez-Flechoso, M. Á., Aparicio, A., & Carrera, R. 2004, ApJ, 601, 242

Mateo, M. L. 1998, ARA&A, 36, 435

Mayer, B., & Kylling, A. 2005, Atmos. Chem. Phys., 5, 1855

McConnachie, A. W. 2012, AJ, 144, 4

McWilliam, A. 1990, ApJS, 74, 1075

Mohr, J. J., Armstrong, R., Bertin, E., et al. 2012, Proc. SPIE, 8451, 84510D

Newberg, H. J., Willett, B. A., Yanny, B., & Xu, Y. 2010, ApJ, 711, 32

Newberg, H. J., Yanny, B., Rockosi, C., et al. 2002, ApJ, 569, 245

Nie, J. D., Smith, M. C., Belokurov, V., et al. 2015, ArXiv e-prints, arXiv:1508.01272

Odenkirchen, M., Grebel, E. K., Rockosi, C. M., et al. 2001, ApJ, 548, L165

Padmanabhan, N., Schlegel, D. J., Finkbeiner, D. P., et al. 2008, ApJ, 674, 1217

Pawlowski, M. S., McGaugh, S. S., & Jerjen, H. 2015, ArXiv e-prints, arXiv:1505.07465

Pawlowski, M. S., Pflamm-Altenburg, J., & Kroupa, P. 2012, MNRAS, 423, 1109

Peñarrubia, J., Martínez-Delgado, D., Rix, H. W., et al. 2005, ApJ, 626, 128

Pereira, R., Thomas, R. C., Aldering, G., et al. 2013, A&A, 554, A27

Perryman, M. A. C., Lindegren, L., Kovalevsky, J., et al. 1997, A&A, 323

Price-Whelan, A. M., Johnston, K. V., Sheffield, A. A., Laporte, C. F. P., & Sesar, B. 2015, MNRAS, 452, 676

Querel, R. R., & Kerber, F. 2014, in Society of Photo-Optical Instrumentation Engineers (SPIE) Conference Series, Vol. 9147, Society of Photo-Optical Instrumentation Engineers (SPIE) Conference Series, 92

Rayleigh, L. 1899, Philosophical Magazine, 47, 375

Regnault, N., Conley, A., Guy, J., et al. 2009, A&A, 506, 999

Rheault, J.-P., DePoy, D. L., Marshall, J. L., et al. 2012, in Society of Photo-Optical Instrumentation Engineers (SPIE) Conference Series, Vol. 8446, Society of Photo-Optical Instrumentation Engineers (SPIE) Conference Series, 84466M

Rocha-Pinto, H. J., Majewski, S. R., Skrutskie, M. F., Crane, J. D., & Patterson, R. J. 2004, ApJ, 615, 732

Rockosi, C., Beers, T. C., Majewski, S., Schiavon, R., & Eisenstein, D. 2009, in Astronomy, Vol. 2010, astro2010: The Astronomy and Astrophysics Decadal Survey

Rockosi, C. M., Odenkirchen, M., Grebel, E. K., et al. 2002, AJ, 124, 349

Rossetto, B. M., Santiago, B. X., Girardi, L., et al. 2011, AJ, 141, 185

Rutledge, G. A., Hesser, J. E., & Stetson, P. B. 1997, PASP, 109, 907

Ryan, S. G., & Lambert, D. L. 1995, AJ, 109, 2068

Sanderson, R. E., & Helmi, A. 2013, MNRAS, 435, 378

Schiavon, R. P., Barbuy, B., Rossi, S. C. F., Milone, & A. 1997, ApJ, 479, 902

Schlafly, E. F., & Finkbeiner, D. P. 2011, ApJ, 737, 103

Schlafly, E. F., Finkbeiner, D. P., Jurić, M., et al. 2012, ApJ, 756, 158

Schlegel, D. J., Finkbeiner, D. P., & Davis, M. 1998, ApJ, 500, 525

Schönrich, R., Binney, J., & Dehnen, W. 2010, MNRAS, 403, 1829

Schuster, G. L., Dubovik, O., & Holben, B. N. 2006, J. Geophys. Res., 111, D07207

Scolnic, D., Casertano, S., Riess, A., et al. 2015, ApJ, 815, 117

Searle, L., & Zinn, R. 1978, ApJ, 225, 357

Sesar, B., Vivas, A. K., Duffau, S., & Ivezić, Ž. 2010, ApJ, 717, 133

Sesar, B., Ivezić, Ž., Lupton, R. H., et al. 2007, AJ, 134, 2236

Sevilla, I., Armstrong, R., Bertin, E., et al. 2011, ArXiv e-prints, arXiv:1109.6741

Sharma, S., Bland-Hawthorn, J., Johnston, K. V., & Binney, J. 2011, ApJ, 730, 3

Sharma, S., & Johnston, K. V. 2009, ApJ, 703, 1061

Sharma, S., Johnston, K. V., Majewski, S. R., et al. 2010, ApJ, 722, 750

Sheffield, A. A., Johnston, K. V., Majewski, S. R., et al. 2014, ApJ, 793, 62

Simion, I. T., Belokurov, V., Irwin, M., & Koposov, S. E. 2014, MNRAS, 440, 161

Simon, J. D., Drlica-Wagner, A., Li, T. S., et al. 2015, ApJ, 808, 95

Skrutskie, M. F., Cutri, R. M., Stiening, R., et al. 2006, AJ, 131, 1163

Slater, C. T., Bell, E. F., Schlafly, E. F., et al. 2014, ApJ, 791, 9

Smith, V. V., & Lambert, D. L. 1986, ApJ, 311, 843

Sollima, A., Valls-Gabaud, D., Martinez-Delgado, D., et al. 2011, ApJ, 730, L6

Steinmetz, M., & Navarro, J. F. 2002, New A, 7, 155

Stetson, P. B. 2000, PASP, 112, 925

—. 2005, PASP, 117, 563

Stubbs, C. W., & Tonry, J. L. 2006, ApJ, 646, 1436

Stubbs, C. W., High, F. W., George, M. R., et al. 2007, PASP, 119, 1163

Ångström, A. 1924, Quarterly Journal of Royal Meteorological Society, 50, 121125

Tucker, D. L., Annis, J. T., Lin, H., et al. 2007, in Astronomical Society of the Pacific Conference Series, Vol. 364, The Future of Photometric, Spectrophotometric and Polarimetric Standardization, ed. C. Sterken, 187

Vivas, A. K., Zinn, R., Andrews, P., et al. 2001, ApJ, 554, L33

Wallace, L., Hinkle, K., & Livingston, W. 2007, An Atlas of the Spectrum of the Solar Photosphere from 13,500 to 33,980 cm^{-1} (2942 to 7405 Å)

Walsh, S. M., Jerjen, H., & Willman, B. 2007, ApJ, 662, L83

Wang, J., Frenk, C. S., & Cooper, A. P. 2013, MNRAS, 429, 1502

Warren, S. R., & Cole, A. A. 2009, MNRAS, 393, 272

Watkins, L. L., Evans, N. W., Belokurov, V., et al. 2009, MNRAS, 398, 1757

White, S. D. M., & Frenk, C. S. 1991, ApJ, 379, 52

Willman, B., Blanton, M. R., West, A. A., et al. 2005a, AJ, 129, 2692

Willman, B., Dalcanton, J. J., Martinez-Delgado, D., et al. 2005b, ApJ, 626, L85

Wittman, D., Ryan, R., & Thorman, P. 2012, MNRAS, 421, 2251

Xu, Y., Newberg, H. J., Carlin, J. L., et al. 2015, ApJ, 801, 105

Yanny, B., Newberg, H. J., Kent, S., et al. 2000, ApJ, 540, 825

Yanny, B., Newberg, H. J., Grebel, E. K., et al. 2003, ApJ, 588, 824

Yanny, B., Rockosi, C., Newberg, H. J., et al. 2009, AJ, 137, 4377

York, D. G., Adelman, J., Anderson, Jr., J. E., et al. 2000, AJ, 120, 1579

Zentner, A. R., Berlind, A. A., Bullock, J. S., Kravtsov, A. V., & Wechsler, R. H. 2005, ApJ, 624, 505

Zinn, R. 1993, in Astronomical Society of the Pacific Conference Series, Vol. 48, The Globular Cluster-Galaxy Connection, ed. G. H. Smith & J. P. Brodie, 302

Zolotov, A., Willman, B., Brooks, A. M., et al. 2009, ApJ, 702, 1058

Zucker, D. B., Belokurov, V., Evans, N. W., et al. 2006, ApJ, 643, L103